UiO : University of Oslo

Martin Nyborg

Dominant Defect Complexes in Cuprous Oxide

Thesis submitted for the degree of Philosophiae Doctor

Department of Physics
Faculty of Mathematics and Natural Sciences

2022

Series of dissertations submitted to the
Faculty of Mathematics and Natural Sciences, University of Oslo
No. 2512

ISSN 1501-7710

Cover: Hanne Baadsgaard Utigard.
Print production: Reprosentralen, University of Oslo.

Proverbs 3:19-27

Abstract

Exploratory work towards alternative abundant materials is essential to realize the large-scale adoption of novel solar cell concepts in the industry. Cu_2O is a possible candidate for both thin-film and tandem solar cells with its abundant, non-toxic constituents and possible realization through a range of production schemes. However, it has not yet fully realized its potential. In this thesis, the electronic properties of Cu_2O are investigated to elucidate the importance of defects in Cu_2O for solar cell application.

Cu_2O has a natural p-type conductivity usually attributed to cation deficiency. In this thesis, Cu_2O thin films and bulk crystals have been investigated to better understand the shortcomings of thin-film Cu_2O solar cell performance. Electronic properties of single crystal (111) Cu_2O wafers have been investigated using a number of complementary techniques. Here, cathodoluminescence, thermal admittance spectroscopy, and temperature-dependent Hall effect analysis revealed four dominant electronic transition levels in the crystal at 0.15, 0.22, 0.4, and $\sim$ 1.3 eV above the valence band edge. Further, from the temperature-dependent mobility data, we have identified that the limiting mechanism of carrier mobility can be described by scattering on neutral and ionized defect centers in the Cu_2O single crystal. The origin and identity of the defect centers and the corresponding electronic centers are discussed.

In order to investigate the effect of Li doping, magnetron sputtered undoped, and Li-doped Cu_2O films were studied through complementary techniques. Li doping significantly alters the electrical properties of Cu_2O and increases hole concentration at room temperature for higher Li concentrations. This can be considered as a counter-intuitive finding since Li is theorized to passivate the copper vacancy acceptors states, commonly believed to be the dominating acceptor in Cu_2O. Moreover, the apparent activation energy for the dominant acceptors decreases from around 0.2 eV for undoped or lightly doped Cu_2O down to as low as 0.05 eV for higher Li concentrations.

Simulations were performed to elucidate the effect of the known acceptor levels in Cu_2O on solar cell performance. The study concludes that concentrations above $10^{15} cm^{-3}$ of the acceptor level at 0.4 eV lead to high levels of Shockley-Read-Hall recombination, impeding cell performance. Thin-film Cu_2O typically has higher concentrations of the deep acceptor, which could explain the low solar cell efficiencies achieved to date.

Acknowledgements

First, I would like to honor my late professor Bengt G. Svensson for his passion and care during my early years at the LENS group. In his memory:

"Crystals are like people: it is the defects in them which tend to make them interesting!"

C. J. Humphreys

This thesis would not have materialized without the continuous support and help from all the wonderful people surrounding me. I would like to thank my main supervisor Eduard Monakhov, for guidance, discussions and encouragement throughout these years. My PhD would not have been possible without your expertise in the field and contributions. I would also like to thank my co-supervisor, Kristin Bergum, for answering an endless stream of questions during my first period as a Ph.D. student and for guidance related to day-to-day lab work. Thank you for contributing with your vast knowledge in the field. I have learned a lot from working with you.

The work in my thesis relies heavily on experimental work, and I would therefore like to show my gratitude towards Viktor Bobal, Christoph Seiffert, and Halvor Dolva for keeping MiNaLab up and running. Without the troubleshooting magic touch from Viktor, I am not sure if any of my films would ever have been deposited.

I am very grateful to all my colleagues at LENS; thanks for the reception, social life, and endless encounters throughout these past years. I would like to thank Kjetil Karlsen, who I had the pleasure to supervise during his master's degree. I enjoyed working with you and wish you the best of luck on your own Ph.D.

Lastly I would like to thank my friend and family. Your support and encouragement have been uplifting. Especially thanks to mom and dad for cheering me on when motivation was low. Finally, I want to thank my proudest attribute, Pernille. This work would not have been possible without your unselfish support. You are my rock, and I love you so much.

List of Papers

Paper I

Nyborg, M., Kolevatov I., Vásquez, C. G., Bergum, K., Monakhov, E.
Dominant Defects and Carrier Transport in Single Crystalline Cuprous Oxide: A New Attribution of Optical Transitions
Journal of applied Physics **130** (2021) 175701 DOI: 10.1063/5.0059406

My contribution: Coordinating and conducting experimental work, analyzing results, discussions, and manuscript writing. Experimental techniques performed by the defendant: Temperature-dependent Hall effect measurements, and Thermal admittance spectroscopy.

Paper II

Nyborg, M., Azarov, A., Bergum, K., Monakhov, E.
Deposition and Characterization of Lithium Doped Direct Current Magnetron Sputtered Cu_2O Films
Thin Solid Films **722** (2021) 138573 DOI: 10.1016/j.tsf.2021.138573.

My contribution: Coordinating and conducting experimental work, analyzing results, discussions, and manuscript writing. Experimental techniques performed by the defendant: DC/RF Magnetron sputtering, X-Ray diffraction, Hall effect measurement,s and UV-VIS transmittance.

Paper III

Nyborg, M., Karlsen, K., Bergum, K., Monakhov, E.
Dominant Acceptors in Li Doped, Magnetron Deposited Cu_2O Films
Materials Research Express **8** (2021) 125903. DOI: 10.1088/2053-1591/ac3e24

My contribution: Coordinating and conducting experimental work, analyzing results, discussions, and manuscript writing. Experimental techniques performed by the defendant: Temperature-dependent Hall effect measurements.

Paper IV

Nyborg, M., Bergum, K., Monakhov, E. *The Effect of Known Deep Acceptors on Performance of Cu_2O Solar Cells*
Manuscript in preparation for submission.

My contribution: Simulations, analyzing results, discussions and manuscript writing.

Contents

Chapter 1

Introduction

In the past century, semiconductors have revolutionized and accelerated technological advancements exponentially. From its first mention in 1911, the technology has evolved from single Si transistors in the 1950s to billions delicately pieced together on integrated circuit chips.[1, 2] Today, semiconductors are again part of a paradigm change, now within the energy sector. The world's electricity generation has over doubled over the last few decades.[3] This is expected to accelerate further as an increasing portion of the world's population gains access to modern commodities, increased consumer consumption, and growing travel habits. In modern society, the world's energy mix is complex and is historically dominated by non-renewables, i.e., coal, natural gas, and petroleum. However, climate change and the shift toward sustainable energy production puts restrictions on CO_2 emissions. Thus alternative renewable energy sources experience immense growth and are required to scale fast.

While most energy resources are indirectly connected to the sun's activity and radiation, the beauty of semiconductor solar cells is the ability to convert solar radiation directly into electricity. It is only in the recent decades that solar cells have been realized commercially on a large scale. Currently, solar energy is the fastest-growing energy resource and is projected to play a crucial role in achieving the shift to renewable energy sources.[4]

Si-based solar cells are a mature technology with high conversion efficiencies and accounts for as much as 95% of the annual solar module production in 2020 (15% multi- and 80% mono-crystalline Si).[6] Silicon is an indirect bandgap material, requiring a thickness of $\sim 100\ \mu m$ to absorb the solar radiation efficiently. Thin-film technologies such as amorphous Si, CIGS, and CdTe cells accounted for about 7% of the market share. These thin-film technologies are mainly based on direct-bandgap materials, which absorb the solar radiation much more efficiently, allowing for films down to $\sim 1\ \mu m$ in thickness. Advantages of thin-film solar cells include the possibility of cheap and flexible substrates, ease of handling, and, more importantly, lower material usage and production costs. One of the significant challenges is the inferior transport properties due to added complexity in thin films, resulting in lower conversion efficiencies. Unfortunately, today's dominating thin-film technologies will have challenges in meeting the increasing demand. Both CIGS and CdTe contain either scarce or toxic constituents, limiting their potential for scalability.

New emerging technologies, however, have already demonstrated the

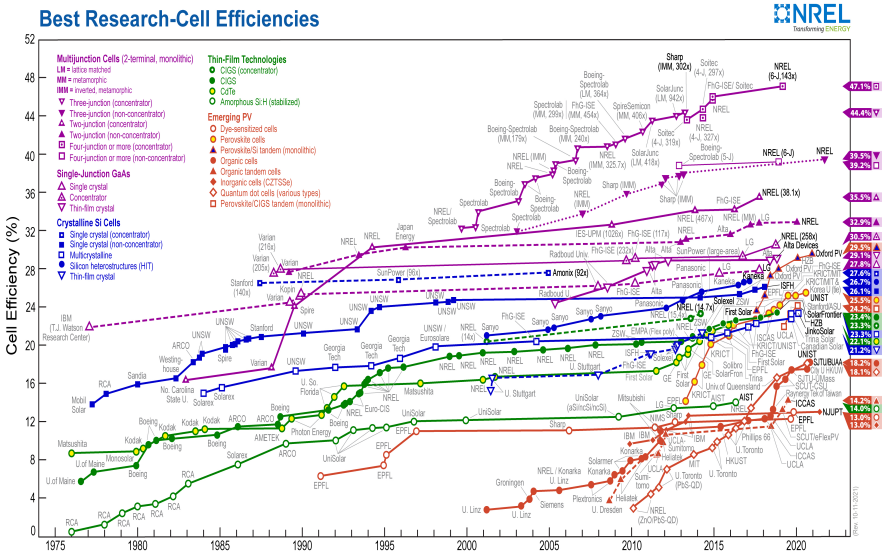

Figure 1.1: NREL's best research-cell efficiency chart under standard test conditions [5]

potential for high efficiency (red symbols in Fig. 1.1). They rely on low material use and non-toxic constituents, which allows for scalable production into the Terra watt scale. [7, 8] Perovskites-based solar cells are perhaps the most spectacular example and have seen explosive research interest since their first mention in 2009, accompanied by solid improvements in research-cell efficiencies, with recent single-junction efficiencies reaching above 25%. [9, 10] Perovskite/Si tandem solar cells have already achieved efficiencies of around 29%. [11] Organic solar cells are another emerging technology with the potential of short payback times compared to conventional technologies. The cells have the potential for mechanical flexible substrates and low production costs, and promising efficiencies of 18% already demonstrated. [9, 12, 13]

Tandem solar cells open the possibility of achieving efficiencies above the single-junction Shockley–Queisser limit ($\sim$ 30 % for Si). In tandem solar cells, two or more cells are stacked on top of each other. As each cell absorbs different parts of the solar spectrum, some fundamental losses due to transmission and thermalization are avoided. By this approach, solar cells with efficiencies exceeding 40 % could be achieved, with an efficiency of 32.9% already achieved for two-junction cells (purple triangles in Fig. 1.1).[5] From Fig. 1.1, one can see that the multijunction cells have successfully achieved stellar performances. However, exotic materials and the required epitaxial growth make them expensive, limiting their use to space applications where the high performance outweighs the fabrication cost. As previously

mentioned, perovskite/Si tandem devices have achieved disruptive results, and currently, efficiencies of 29.5% are reported, sparking hope for possible low-cost emerging PV technologies.[11]

Cuprous oxide (Cu_2O) is an abundant, low-cost and non-toxic semiconductor known for its solar cell potential since the late 1920s. However, it is only in the last decade that bulk Cu_2O ($\sim$ 0.2 mm sheets) efficiencies have increased from 2% to 8%.[14] Additionally, Cu_2O is an intriguing material due to its possible application in tandem solar cells. The bandgap of 2.17 eV makes it a candidate as p-type absorber material in a tandem solar cell structure paired with a conventional Si-based subcell.[15, 16, 17] Progress in thin-film Cu_2O has been elusive, with efficiencies struggling to exceed 1-4%. The challenge is believed to be partially due to the inability to control the defect concentrations in Cu_2O[18]. Therefore, more work on the origin and identity of acceptors in Cu_2O is required.

This thesis researches bulk crystals and thin-film Cu_2O to investigate the shortcomings in thin-film Cu_2O solar cell performances. Synthesis and characterization of sputtered Li doped Cu_2O thin-films have been conducted and compared to undoped films to investigate its theorized potential to passivate dominating acceptors in Cu_2O. Finally, simulations have been carried out to elucidate the effect of unintentional high concentrations of deep acceptors in sputtered Cu_2O cells. The thesis is organized as follows; Chapter 2 introduces Cu_2O, its properties, and relevant literature regarding its application in solar cells. Chapter 3 introduces the experimental methods utilized in this thesis. Chapter 4 summarizes the main results in the appended papers and relevant unpublished results. Finally, in Chapter 5, conclusions and suggestions for future work are presented.

Chapter 2

Cuprous Oxide

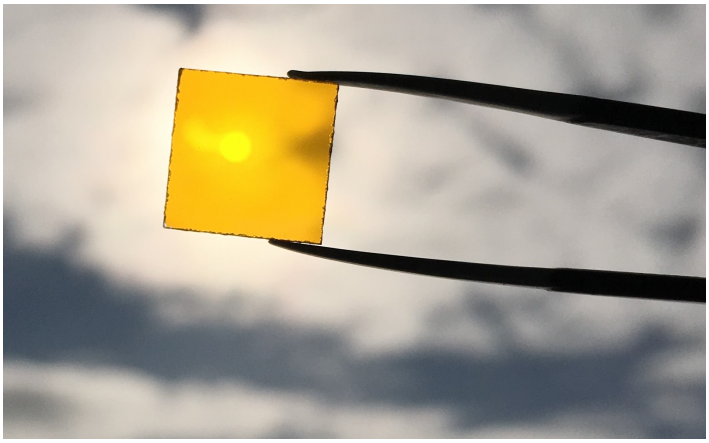

Figure 2.1: Cu_2O thin film grown on fused silica substrate by reactive magnetron sputtering ($t \sim 500nm$)

The semiconducting properties of Cu_2O have a rich history, and it was one of the earliest recognized semiconductor materials in the early 1900s. In 1924, one of the first semiconductor devices was realized on Cu_2O with a copper contact, forming a rectifying junction later recognized as a Schottky contact. [1] This was surely prerequisite for the later work on silicon and germanium transistors, which led to a Nobel prize for Brattain and Bell, laying the foundation for much of the semiconductor device physics we know today. Since then, Cu_2O has been a widely studied material and was also one of the first materials where the photoelectric effect was observed; however, after discovering high-quality germanium and silicon production in the 1940s, the interest in Cu_2O cells became dormant. Due to the rising demand for renewable energy, the interest has again spiked as a possible large-scale solar cell absorber material. In addition, its potential application as a top cell in tandem solar cells is intriguing. The bandgap of Cu_2O at 2.17 eV [19] would be a good match when paired with the already market-dominant silicon-based bottom cell.[20]

Cu_2O has also gained interest in many other areas. Oxide semiconductors are of great interest for flexible and transparent electronic applications. While several high-performing n-type oxides are already utilized in thin-film transistors, the p-type counterpart has been challenging to achieve.

Cu_2O-based thin-film transistors could, however, be a viable option.[21] Cu_2O-based composites have been widely studied in the application as photocatalysts, where it has demonstrated enhanced performances in photocatalytic degradation of pollutants, water splitting, CO_2 reduction, and sterilization. [22, 23] Finally, it is an exciting material in several emerging fields where the application of Cu_2O is still only in its infancy. In the comprehensive review on the development of synthesis, properties, and application of Cu_2O tailored architectures by Sun *et al.* [24], they highlight many possible uses such as antibacterial activity, solar energy conversion, lithium-ion batteries, sodium-ion batteries, supercapacitors, and metal-insulator switching memories.

2.1 Phase Stability and Synthesis

2.1.1 Cu-O phase diagram

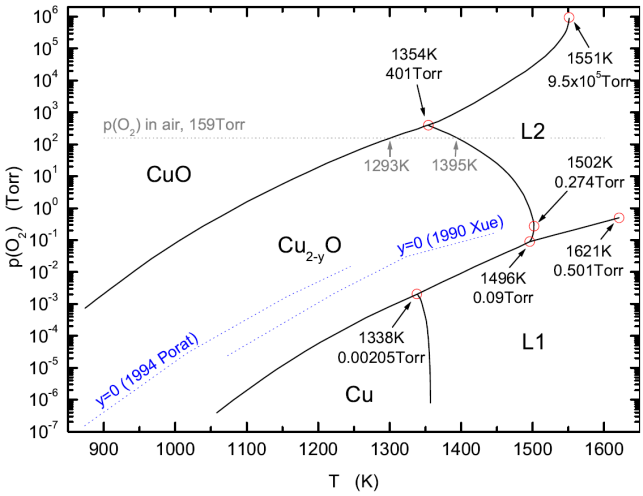

Figure 2.2: Phase diagram of Cu_xO for oxygen partial pressure, $p(O_2)$, vs. temperature, T. Retrieved from Ref [25].

The copper oxide system Cu-O consists of two stable oxides: the black cupric oxide (CuO) and the red cuprous oxide (Cu_2O). The phase diagram of the copper oxide system Cu-O, as reported by Biccari [25], is shown in Fig. 2.2. A high temperature of $\simeq 1000\,^o$ C is required for oxidizing copper sheets into phase pure Cu_2O crystals at atmospheric oxygen levels. [25, 26]

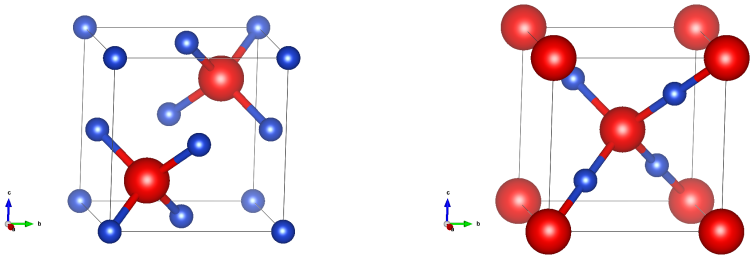

(a) Origin on a copper site. (b) Origin on an oxygen site

Figure 2.3: Unit cell of the cuprite structure for; a) Origin at the copper site. b) origin at the oxygen site. The structures contain two Cu_2O formulas per unit cell. Red spheres represent oxygen atoms, and blue spheres are copper atoms.

2.1.2 Cu_2O crystal structure

Cu_2O crystallizes in a simple cubic Bravias lattice known as the cupric structure (Fig. 2.3). The space group is Pn-3m (224), containing six atoms [27]. Depending on the element at origin, it can be illustrated in two equivalent sublattices translated by a(1/4,1/4,1/4), with copper at the origin in a face-centered copper sublattice with two oxygen ions at a(1/4,1/4,1/4) and a(3/4,3/4,3/4) (Fig. 2.3 a), or with oxygen at the origin where oxygen resides on a body-centered sublattice with Cu ions tetrahedrally coordinated around the center oxygen ion (Fig. 2.3 b). The oxygen atom is tetrahedrally fourfold coordinated with the copper atom, while the copper atom is linearly twofold coordinated with oxygen. The lattice constant a is 4.2696 ± 0.0010 Å, and the Cu-Cu bond length is 3.01 Å, O-O bond length 3.68Å, and Cu-O bond length 1.85 Å [19]. An interesting property of the crystal structure is the dichotomy of the crystal lattice, which can be viewed as two identical interpenetrating networks with the same anti-SiO_2 structure (cristobalite).[28] The two networks have no primary chemical bonds between them and are physically separated and loosely bound from van der Waals forces. Which is possibly bound to the physical properties of Cu_2O such as its negative thermal expansion and low shear modulus. [28]

2.1.3 Growth methods

Most conventional growth methods are possible for Cu_2O synthesis, and bulk crystals have been prepared by, e.g., floating zone growth, melt growth, and thermal oxidation of copper sheets. [29] Minami *et al.* [26] describe the oxidation process, where copper sheets are heated up in an Ar or N_2 atmosphere to 1010^oC before being subjected to two-hour oxidation in air at

the same temperature. Finally, the sample is cooled down in an Ar or N_2 atmosphere before quenching in the air from 500 ^{o}C. Minami *et al.* currently hold the record efficiency in Cu_2O-based solar cells utilizing a similar process in their work from 2016. [14]

Thin-film growth is possible by most common deposition methods with a wide range of conditions and temperatures, e.g., electro-deposition [30], molecular beam epitaxy [31], atomic layer deposition [32], radio frequency (RF) [33], and direct current (DC) reactive magnetron sputtering [34].

The technique practiced in this thesis is magnetron sputter (MS) deposition, which is suitable for low cost and large-scale production. Sputtering provides close control over different vital parameters to achieve the correct phase in the Cu_xO system. Additionally, it allows for a high degree of flexibility for impurity doping through doped targets, gas inclusion, or co-sputtering of the desired element(s). Which copper oxide phase is deposited depends critically on the oxygen partial pressure p_{O_2} during deposition, which is commonly controlled by the O_2 to Ar flow ratio. [35] Further, the flow rate can be tuned to control the growth conditions of the film, i.e., oxygen lean or oxygen-rich conditions, which are closely correlated to the carrier densities present in the films. Li *et al.* [36] reported that a slight increase of oxygen partial pressure (0.2% increase in O_2 to Ar ratio) resulted in order of magnitude increase in carrier density.

Substrate temperature and target power during deposition can be tuned to increase adatom mobility during deposition and elevate crystal quality. Also, target power and argon flow increase the Cu target ion bombardment, influencing the deposition rate and film stoichiometry. Gan *et al.* [33] achieved superior crystal quality for the highest RF deposition power of 190 W in their study on target power during deposition of Cu_xO thin films. Different orientations are known to co-exist in sputtered polycrystalline films, and the preferred orientation is affected by the applied target power during deposition. Consequently, the flexibility during sputter deposition provides both challenges and possibilities, where close control of all parameters is crucial to achieving the desired stoichiometry and film properties.

Post deposition annealing has demonstrated favorable results on sputtered Cu_2O. Bergum *et al.* [37] find that post-deposition rapid thermal annealing for 3 minutes at 900 ^{o}C significantly increases the lateral crystal grain size in DC magnetron sputtered thin films. Concurrently, carrier mobility is increased from $\sim 2\,cm^2/Vs$ to $54 cm^2/Vs$ in the film annealed at 900 ^{o}C.

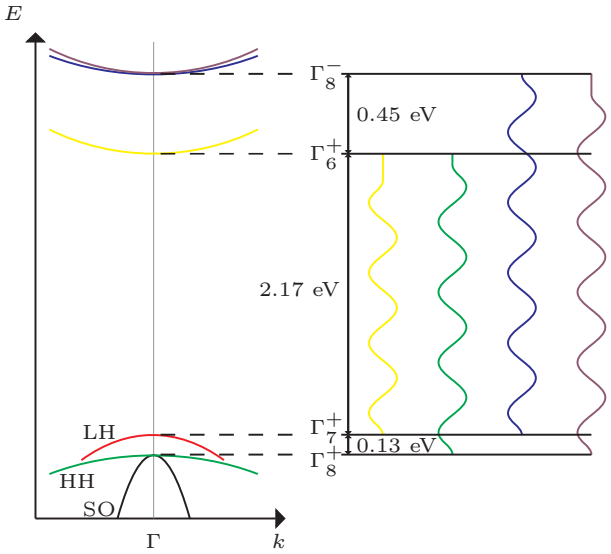

Figure 2.4: Energy band structure of Cu_2O near the Γ-point. The valence band is split by spin-orbit interaction into the Γ_7^+ and Γ_8^+ states with associated light hole (LH) and heavy hole (HH) masses, respectively. The four exciton series resulting from interband transitions are illustrated to the right (yellow, green, blue, and indigo).

2.2 Optoelectronic Properties

2.2.1 Band structure and optical transitions

The band structure of Cu_2O is shown schematically in Fig. 2.4, where the gap between the lowest conduction band (Γ_7^+) and highest valence band (Γ_6^+) is 2.17 eV. [19, 38] The transition between the two lowest transitions ($\Gamma_7^+ \rightarrow \Gamma_6^+$ and $\Gamma_8^+ \rightarrow \Gamma_6^+$) is parity forbidden following the LaPorte rule since the valence band is mainly built up from the $3d^{10}$ states, and the conduction bands have 4s Cu-like characters. The lowest direct allowed transition is thus, $\Gamma_7^+ \rightarrow \Gamma_8^-$ and $\Gamma_8^+ \rightarrow \Gamma_8^-$. The four transitions span the visible spectra and are named after their color, the yellow, green, blue, and indigo exciton series, respectively. [19]

Tauc analysis of the absorption in Cu_2O reports an optical bandgap with values in a wide range of 2.1-2.5 eV. Malerba *et al.*[38] found that the absorption coefficient in Cu_2O includes various contributions from direct, forbidden, and indirect transitions. Therefore, extrapolating the bandgap from a Tauc analysis assuming a single dominating transition will give incorrect values for the bandgap. [38]

The effective masses from the top of the valence band (m^*_{LH} and bottom of the conductance band (m^*_e), together with electron affinity, χ, and work function, Φ, are listed in Tab. 2.1 From the effective masses, the effective density of states in the conduction band (N_C) and valence band (N_V) can be deduced from the relations:

$$N_C(T) = 2\left(\frac{2\pi m^*_e kT}{h^2}\right)^{3/2} = 4.76 \times 10^{15} T^{3/2} cm^{-3}$$

$$N_V(T) = 2\left(\frac{2\pi m^*_{LH} kT}{h^2}\right)^{3/2} = 2.13 \times 10^{15} T^{3/2} cm^{-3}$$

where k is Boltzman constant, h is Planck's constant, and T is the temperature.

Table 2.1: Material parameters of Cu_2O

m_e	0.99
m^*_{LH}	0.58
electron affinity, χ	$\simeq$ 3.1 eV
work function, Φ	$\simeq$ 4.84 eV
permittivity, ϵ	$\simeq$ 7.11

2.2.2 Intrinsic defects

The high bandgap of Cu_2O yields a negligible intrinsic carrier density at room temperature. Nevertheless, the carrier concentration in undoped Cu_2O is routinely reported in the range $10^{12} - 10^{16} cm^{-3}$ at room temperature. [33, 40, 41, 42, 43, 44, 45] The electronic transport properties in Cu_2O are closely related to the growth conditions and impurities present in the crystal. Most oxide semiconductors are insulating and stoichiometric, except for a few *n*-type oxides (anion deficient) such as ZnO and even fewer *p*-type oxides, such as Cu_2O. The *p*-type conductivity of Cu_2O is attributed to deviation from stoichiometry (cation deficiency) and formation of the copper vacancy V_{Cu}, with its associated acceptor states in the bandgap. [1, 46, 47, 48, 49] The *p*-type nature of Cu_2O is explained by Raebriger *et al.* [50] by first-principles calculation of equilibrium non-stoichiometry and defect stability. Generally, when an oxide has a stable higher oxidation state, it will naturally be cation deficient, which is the case with $Cu_2^{(I)}O$ and $Cu^{(II)}O$ in Cu_2O. Further, they report that mainly copper vacancies accommodate the cation deficiency, with low formation energy compared to the oxygen interstitial and a stable concentration of $\sim 10^{20} cm^{-3}$ V_{Cu} can be present in the material. [50] Additionally, another configuration of the vacancy, the so-called split vacancy, V^{split}_{Cu}, is predicted from theoretical studies and

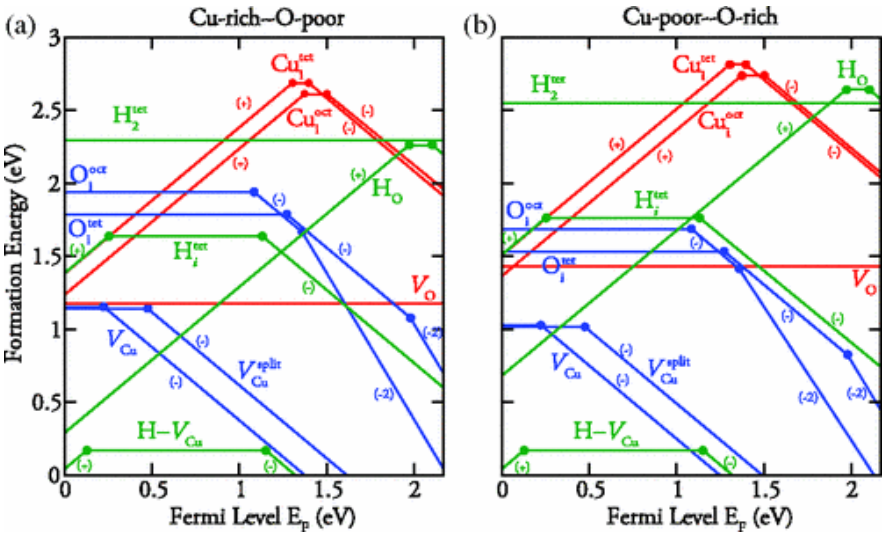

Figure 2.5: Formation energies for intrinsic and H-related defects in Cu_2O reprinted from Scanlon et al. [39]. HSE calculated formation energies for p-type (blue), n-type (red), and hydrogen impurity (green) defects in (a) Cu-rich-O-poor conditions and (b) Cu-poor-O-rich conditions. The solid dots denote the transition levels $\epsilon(q/q')$. Reprinted with permission from © the American Physical Society (2011).

observed experimentally. [41, 42, 48, 49, 50, 51, 52] In Fig. 2.6 the simple and split vacancy structure is shown. The split vacancy is formed when a nearby Cu atom moves towards the vacancy site, creating a stable intermediate state, where it is tetrahedrally coordinated to four O atoms. In Fig. 2.5, formation energies calculated by density functional theory (DFT) is plotted as a function of the Fermi level for intrinsic and hydrogen-related defects. As mentioned previously, another possible source of *p*-type conductivity is the oxygen interstitials O_i^{oct} and O_i^{tet}. However, they are believed to have high formation energy and deep transition levels compared to the copper vacancies. [49, 50]

The dominating acceptor levels reported experimentally have activation energies of ~ 0.25 eV and ~ 0.5 eV. [41, 42] From DFT, Scanlon *et al.* [49] have reported that the formation of V_{Cu} and V_{Cu}^{split} produces acceptor states at Ev + 0.23-0.28 eV and Ev + 0.41 eV, respectively (see Fig. 2.5). The V_{Cu} level is in perfect agreement with the experimental report by Paul *et al.* [42], which finds a shallow acceptor level at Ev + 0.25 eV from deep level transient spectroscopy. The acceptor is sensitive to the oxygen flow rate during growth, solidifying the assignment to V_{Cu}. Additionally, a deeper level is found by Paul *et al.* [42] and predicted by Scanlon *et al.* [49] at Ev + 0.41 eV and

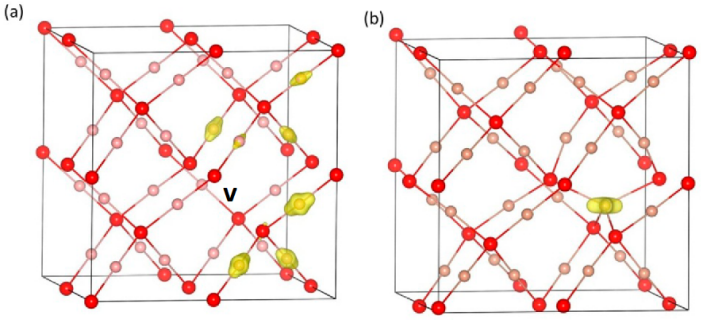

Figure 2.6: Structure of the (a) simple vacancy and (b) split vacancy in Cu_2O. The red and pink spheres represent O and Cu, respectively. The hole is quite delocalized for (a) the simple vacancy, whereas it is strongly localized for (b) the split vacancy.[52] Reprinted with permission from [52]. Copyright (2021) American Chemical Society.

Ev + 0.47 eV, respectively. This is also in agreement with the level reported by Papadimitriou [41], which finds a trap level at Ev + 0.41 from DLTS analysis on undoped single crystal Cu_2O. This level is generally attributed to the V_{Cu}^{split}. [48, 49, 50, 51, 52]

2.2.3 Extrinsic defects and doping

Extrinsic doping of Cu_2O has been widely studied in the literature (see, i.e., Refs. [19, 25] and references therein). Among the investigated elements are N, Li, H, Sr, Cr, Fe, Ag, Si, Na, S, P, and Cl. [25, 55, 56, 57, 58, 59, 60, 61] Yet, definite assignment of different acceptors and donors in Cu_2O is elusive. Biccari concludes his Ph.D. thesis on defects in Cu_2O with the remark; "are the Cu_2O electrical properties really controlled by intrinsic defects or are they controlled by impurities? This dilemma is quite similar to that still affecting the ZnO community". [25, 62] Most doping of Cu_2O is dependent on the quality of the starting material, which impacts the doping characterization. Some of the most relevant intrinsic and extrinsic defect levels for this thesis are summarized in Fig. 2.7, and the impurities are discussed independently below.

Lithium: Lithium is an isovalent cation with a similar ionic size as Cu^+. It is suggested by Isserof et *al.* [52] in a DFT study that Li doping could suppress vacancy trap formation. The calculations suggest that Li doping passivates the V_{Cu}^{split} by forming a $V_{Cu} - Li$ complex which is significantly energetically favorable. The optimal defect complex structure was identified as Li tetrahedrally coordinated to four oxygen atoms, similar to V_{Cu}^{split}. Therefore, Li doping could be a possible route to passivate the high acceptor

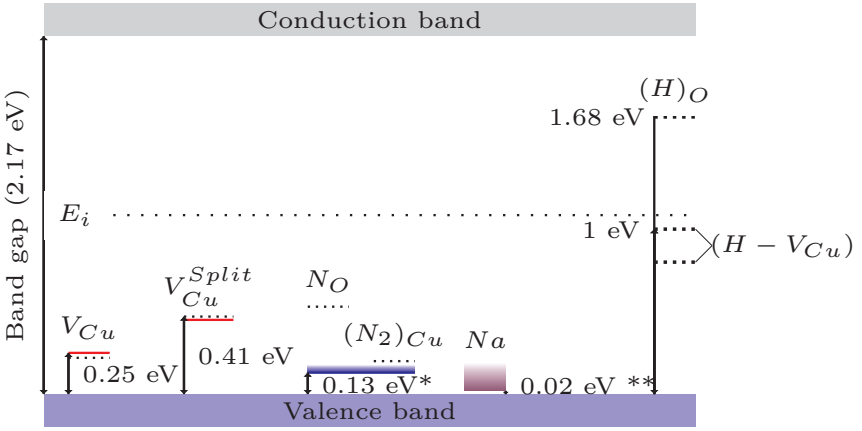

Figure 2.7: Schematic illustration of defects and impurities in Cu_2O with their deduced energy levels within the bandgap from DLTS (solid line) and ionization energies (bands) reported from experimental work. Theoretically predicted transition levels are indicated by dotted lines. [39, 42, 49, 53, 54] *N doped Cu_2O shows a decrease in ionization energy with doping from $\sim$ 0.15 to $\sim$ 0.12. eV[53] **Na doped Cu_2O shows a decrease in ionization energy with doping from $\sim$ 0.19 to $\sim$ 0.02 eV. [55]

density in Cu_2O. However, the few experimental studies on lithium doping report an apparent increase in hole concentration with Li doping. [30, 63] Cho *et al.* [63] demonstrate sputtered p-type Cu_2O films from a 3 *at%*-Li_2O doped Cu_2O ceramic target with hole densities of $8 \times 10^{19} cm^{-3}$. Kim *et al.* [30] investigated electrochemically deposited films where $LiNO_3$ was included with various amounts from 0 to 50 wt% in the electrolyte. They achieved a five times improvement in photocurrent density in a photoelectrochemical cell with Cu_2O prepared with 10wt% $LiNO_3$ compared to the undoped cell. Additionally, in agreement with Cho *et al.* [63], they observed improved grain size in the Li doped samples grown with $<$ 10 wt% $LiNO_3$. Above 10 wt%, they speculate that the reaction of $LiNO_3$ with H_2O could form HNO_3, resulting in etching and limiting grain size.

The report of increased conductivity due to higher acceptor concentrations in Li doped Cu_2O is similar to the reports on Na doping. [55] This is further evidenced in paper II and III, where an emerging shallow acceptor level is reported at $\sim E_v + 0.05eV$ with Li doping. These results are somewhat counter-intuitive since alkali metals are not expected to be an acceptor when substituting for copper, or at interstitial sites in the Cu_2O lattice. This implies other defect configurations in Cu_2O, still unknown, as the source of the shallow acceptor levels associated with Li and Na doping.

Sodium: Elemental doping with Na is an effective approach to achieving

high-quality p-type Cu_2O and is utilized in the best performing solar cell devices to date.[14, 64] Minami *et al.*[55] reports controlled hole concentrations of 10^{13} up to $10^{19} cm^{-3}$ in oxidized copper sheets annealed while covered with a Na compound powder at 400-800 ^oC for 1-30 h in an Ar or N_2 gas atmosphere. For hole concentrations of 10^{13} to $10^{16} cm^{-3}$ the post-treatment mobility of 100 $cm^2/(Vs)$ was retained in the samples. The ionization energy was reported to decrease with increasing hole concentration, from 0.15 eV down to 0.02 eV, until degenerated metallic conductivity was reported for samples with hole concentrations exceeding $10^{19} cm^{-3}$. They propose that the increase in acceptor concentration from Na doping could be explained by charge compensating effects resulting from excess V_{Cu} formation when Na is incorporated at the interstitial site. However, the V_{Cu} is not known to possess such a shallow acceptor level in Cu_2O since the activation energy of V_{Cu} is believed to be $\sim$ 0.25 eV. [42, 49]

Nguyen *et al.* [65] report a smoother surface and larger grain sizes in $\sim 1 \mu m$ Na doped sputtered thin films compared to the undoped films. Low resistivity associated with a hole concentration of 2.1 $\times 10^{18} cm^{-3}$ and mobility of 4.18 $cm^2/(Vs)$ was found from Hall effect measurement. Further, it is speculated that the Na doping is relevant for the passivation of dangling bonds at the grain boundary. [65] However, no theoretical study or experimental verification is found, and the mechanism behind improved crystal quality and chemical identity of acceptor doping with Na is still unknown.

Nitrogen: N doping is another well-established *p*-type dopant in Cu_2O, which is routinely reported with an increase in hole concentration and lowered ionization energy down to $\sim$ 0.12 eV at high doping levels (Fig. 2.7) [53, 66, 67]. An acceptor level at E_V + 0.12-0.18 eV agrees with an estimate based on the effective mass approximation, which gives theoretical activation energy of 0.16 eV[67]. With N doping, the emerging acceptor states have routinely been attributed to nitrogen substituting for oxygen, N_O[53, 66, 67]. Li *et al.* [53] studied the nitrogen-doping-induced defects in Cu_2O, where they reported a unique signature from photoluminescence attributed to interstitial nitrogen at $\sim$ 652 nm (1.90 eV). Further, their study theorizes an evolution of defects with annealing, where a decrease in N_i and V_O, is accompanied by an increase in N_O, suggesting an interaction and formation into N_O with annealing. On the other side, DFT calculations cannot place N_O as a shallow acceptor and rather depicts it as a deep acceptor at $\sim$ E_V + 0.5 eV with high formation energy, labeling it an unlikely source of the emerging acceptor level [54]. Interestingly, the work of Malerba *et al.* [68] observed an optical absorption of N induced defects in Cu_2O at E_V + 0.5 eV. This would harmonize with DFT calculations which predict that the shallow level observed with N doping could instead belong to molecular nitrogen at the copper vacancy, $(N_2)_{Cu}$ (see Fig. 2.8). $(N_2)_{Cu}$ is predicted to have a shallow level at $\sim$ E_V + 0.2 eV and low formation energy[54]. This assignment is further supported by experimental results, which show that

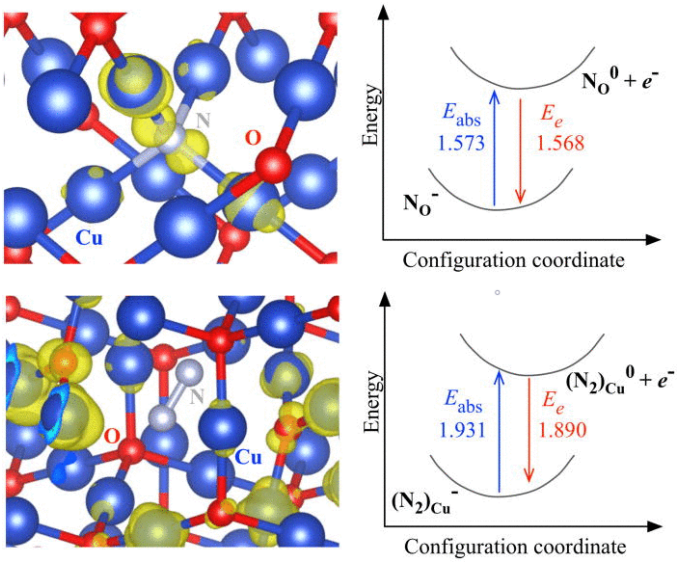

Figure 2.8: (Top left) The local structure of N_O^0 with the charge (hole) density associated with the deep acceptor level shown. (Top right) The schematic illustration of the calculated optical absorption (E_{abs}) and emission (E_e) energies associated with N_O defect for exchanging an electron with the conduction band. The bottom panel shows the local structure, charge density, and optical absorption and emission for $(N2)_{Cu}$. Reprinted from Thienprasert and Limpijumnong [54], with the permission of AIP Publishing.

nitrogen is present in Cu_2O predominantly as N_2 [66, 69, 70]. That said, the chemical configuration and identity of acceptors in nitrogen-doped Cu_2O still require further examinations to be properly discerned.

Hydrogen: Only a few experimental and theoretical works have been conducted on the effect of hydrogen and its role in Cu_2O. Most notably, in a DFT study by Scanlon and Watson, hydrogen is depicted as a "hole killer" in Cu_2O [39]. Several possible atomic configurations for H_i have been calculated in the study, including tetrahedral, octahedral, bond-centered, and anti-bonding configurations. The hypothesis of universal alignment proposed by Walle and Neugebauer [71] proposes that the transition between $H_i(-)$ and $H_i(+)$ is universally aligned to the vacuum level in semiconductors. This level is deduced from DFT calculation at $\sim$ 4.5 eV below the vacuum level [71], together with the electron affinity of Cu_2O (See Tbl. 2.1); this puts the transition, $H_i(+/-)$, at approximately Ev + 0.8 eV following this hypothesis (Fig. 2.7). However, the calculations by Scanlon and Watson [39] depicted H_i as a deep amphoteric defect under both sets of conditions in Cu_2O with the lowest formation energy for the tetrahedral site with a transition level at $\sim$

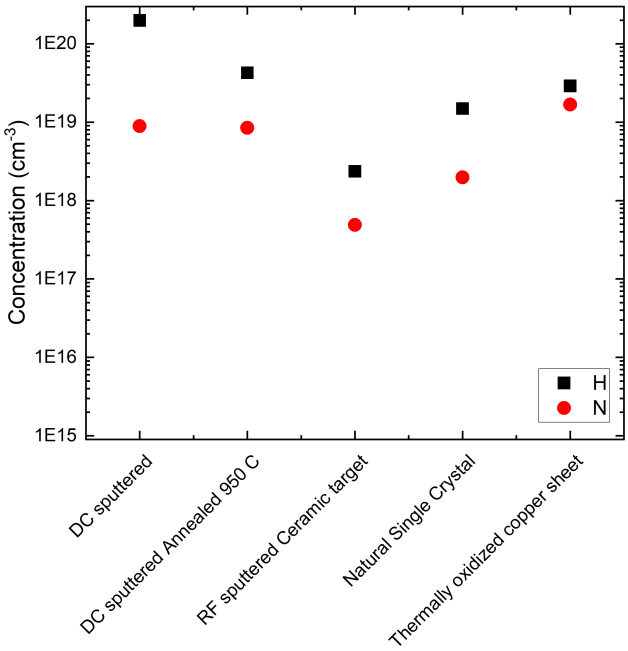

Figure 2.9: Residual impurity concentrations of H and N measured by SIMS in Cu_2O samples from various sources.

Ev + 1eV (Fig. 2.5). It is suggested that it will effectively oppose both *p*-type and *n*-type conductivity in the system. Additionally, they demonstrated the ability of hydrogen to passivate V_{Cu}. The hydrogen-V_{Cu} complex (H-V_{Cu}) has been shown to have the lowest formation energy among all the considered complexes (Fig. 2.5). Finally, H_O^+ is reported as a stable deep donor over most of the bandgap and could oppose *p*-type conductivity in the system.

On the experimental side, Hering *et al.* [59] reported improved carrier transport properties when hydrogen is introduced during Cu_2O deposition by magnetron sputtering. This is attributed to hydrogen passivating donor-like states, resulting in improved mobility in the films. The study also highlights an increase in acceptor ionization energy with higher hydrogen flow during growth, which can be interpreted as the appearance of a hydrogen-related defect with higher activation energy. Tabuchi *et al.* [57] and Kumar *et al.* [58] also report improved mobility in hydrogen-enriched Cu_2O. The increased mobility is accompanied by a decrease in carrier concentration, which suggests either passivation of acceptors by hydrogen or an increase in the acceptor activation energy. These findings are consistent with theoretical

predictions on hydrogen passivation of vacancies performed by Scanlon and Watson. Hering *et al.* [59] report the hydrogen concentration after doping in their study. However, none of the studies report concentrations before and after doping. Hydrogen is believed to be present at high concentrations unintentionally in Cu_2O (Fig. 2.9), making it hard to elucidate the doping effect. The role of H in Cu_2O is ambiguous, and the knowledge of its impact on electrical transport properties is still uncertain.

Historically, the transport properties in Cu_2O are attributed mainly to the intrinsic defects, while the effect of unintentional impurities has not been rigorously considered or investigated experimentally. Fig. 2.9 shows the unintentional residual concentration of hydrogen and nitrogen in different Cu_2O samples. There are considerable concentrations of impurities ranging from $5 \times 10^{18} - 2 \times 10^{20}$ in all samples. The associated acceptor levels are illustrated in 2.7. From theory and experimental results, the role of N and H impurities and the intrinsic copper vacancy configurations (V_{Cu} and V_{Cu}^{Split}) are especially interesting and will require further investigation to precisely identify the the ambiguous deep acceptors in Cu_2O.

2.2.4 n-type Cu_2O

It is proven difficult to achieve n-type conductivity in Cu_2O. Meyer *et al.*[72] approximated through the effective mass theory that the donors have higher binding energies (266 meV) than the acceptors (156 meV) in Cu_2O. Consequently, the high ionization energy and high intrinsic acceptor concentration would require very high donor concentrations to overcome the p-type conductivity at room temperature. However, despite the intrinsic p-type conductivity of Cu_2O, n-type behavior is reported in the literature.[73, 74, 75, 76, 77, 78] Siripala *et al.* [73] demonstrated that electrodeposited Cu_2O show n-type behavior in a liquid/solid junction in a photoelectrochemical cell (PEC). Further, n-type behavior in PECs is realized from the immersion method by boiling Cu plates in $CuSO_4$ or HCl solution. [74, 75] Jayewardena *et al.* [75] found that Cl^- ions in the immersion solution facilitate better cell performance. By flushing oxygen into the solution during the formation of the Cu_2O layer, the cell performance was diminished. Therefore, it was suggested that the n-type behavior was linked to the V_O.

Cu_2O homojunction solar cells have been achieved with sequential electrochemical deposition utilizing different electrolyte solutions during deposition.[76, 77] The n-type nature of the Cu_2O electrodes made by Mcshane *et al.* [76] were confirmed by linear sweep voltammetry with chopped light and Mott-Schottky plots from capacitance measurements. The growth of high-quality Cu_2O homojunction could improve the photovoltaic performance of Cu_2O-based devices. The devices suffer from highly resistive

n-type Cu_2O with conversion efficiency < 1 % and no proper doping technique for low-resistivity n-type Cu_2O.[78, 79]

The source of n-type doping is still unknown and debated in the literature. Suggestions include the oxygen vacancies (V_O)[75, 80] and copper anti-sites (Cu_O) [81]. However, these were later conflicted by a DFT study which concludes that intrinsic defects cannot be the source of the n-type behavior in Cu_2O.[82] They conclude that the intrinsic n-type defects possess deep transition levels excluding them as possible candidates. Also, the most intuitive candidate, namely V_O, is reported no to have a transition in the bandgap at all, ruling out this assignment. It could be speculated that the n-type conductivity stems from unintentional impurity doping by, e.g., Cl or H, which are reported as possible donor dopants in Cu_2O.[39, 75, 82] Based on the results from Nian *et al.*[83], the n-type conduction is linked to the formation of an inversion layer. They propose that a defective surface layer may form in films grown by electrodeposition under copper-deficient conditions. The deficient Cu_2O surface has a large surface-to-volume ratio and is prone to Cu^{2+} absorption, which could be the source of an inversion layer that causes the observed n-type conductivity exclusive for electrodeposited Cu_2O.[83]

2.2.5 Carrier Mobility

Studies of hole mobility limiting mechanisms in Cu_2O demonstrate several dominating scattering mechanisms in the material. Mobility is an important parameter in understanding the electrical properties of the material. It is shown for Cu_2O that the experimental mobility data indicate scattering due to the morphology of the crystal and impurity-related centers. Shimada *et al.* report for single crystals that neutral impurity scattering ($\sim 10^{15}$ cm^{-3}) dominates in the low-temperature regime < 40K. [25, 84] At intermediate temperatures up to ~ 200K, the scattering theory for low and high-frequency modes of the LO phonon and acoustical phonon agrees well with experimental data. [84] Though, at higher temperatures, there is no definite theory to describe the reported sharp decline in mobility observed routinely in Cu_2O at temperatures > 200 K. [84, 85] One possible explanation proposed for the rapid decline in mobility is a meta-stable self-trapped state[84, 86], which would significantly increase the scattering probability at elevated temperatures. In paper I, we report that Cu_2O natural single crystals contain a considerable concentration of deep acceptors and impurities. Additionally, the material is believed to be strongly compensated and thus contains a large concentration of both neutral and ionized impurities. It appears to be a reasonable assumption that the dominating scattering mechanism at high temperatures is that of ionized centers. [45, 87]

2.3 Cu_2O in solar cells

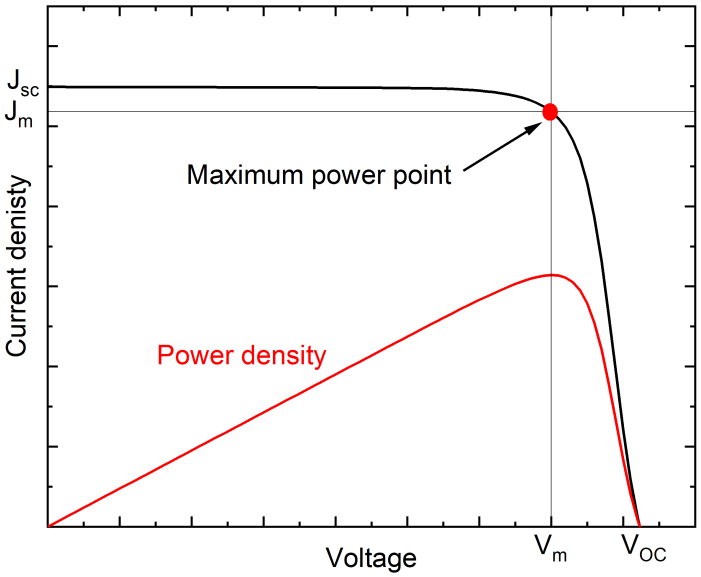

Figure 2.10: Current-voltage (black) and power-voltage (red) characteristics of a pn-junction solar cell. The cell-specific parameters J_{SC}, J_m, V_{OC}, and V_m, are indicated on the axis.

2.3.1 Solar cell operation

Solar cells operate with a one-step conversion of photons to electrical energy. Electrons excited by photons across the bandgap in a semiconductor, generate excited electron-hole pairs. In order to utilize the captured photons' energy, an asymmetry is utilized to separate the charge carriers. This is achieved by a p-n junction, where n-type and p-type semiconductors are joined together. Upon contact, electrons and holes flow over to the opposite side of the junction, leaving behind ionized donor and acceptor host sites which form an electric field across the depleted layer, known as the space charge region (SCR). The resulting potential difference allows the excited electron-hole pairs to drive an external electrical load connected to the cell. Thus, one want to maximize the number of electron-holes generated and minimize the ones lost to recombination in the solar cell. Before illumination, the current-voltage characteristics of an ideal solar cell can be described by the diode equation.

Under forward bias conditions, the majority carriers are injected into their respective side of the junction, and the SCR is reduced. When the SCR reduces, the likelihood of charge carriers crossing the junction increases,

leading to an exponential increase in current with applied forward bias. Under reverse bias, the SCR expands, limiting charge carriers crossing the junction. The current density in the cell under illumination can be described by:

$$J(V) = J_{sc} - J_{dark}(V) \tag{2.1}$$

where J_{SC} is the photo-generated current and $J_{dark}(V)$ for an ideal cell can be given by the diode equation:

$$J(V) = J_{sc} - J_0(e^{qV/nkT} - 1) \tag{2.2}$$

where J_0 is the dark saturation current, n is the diode ideality factor, k is the Boltzman constant, and T is the temperature. The open-circuit voltage is the maximum voltage available from the solar cell, which can be deduced from Eq. 2.2 when the net current is 0, i.e., when the dark current and photo-generated current cancels out:

$$V_{OC} = \frac{nkT}{q} ln(\frac{J_{sc}}{J_0} + 1) \tag{2.3}$$

J_{sc} at 0 V to V_{oc} spans the operating regime of the solar cell. The maximum power output of the cell is somewhere between these extremes at a voltage, V_m, with the corresponding current density J_m, where $P_m = J_m \times V_m$, as illustrated in Fig. 2.10. The cells fill factor is defined as:

$$FF = \frac{J_{mp}V_{mp}}{J_{sc}V_{OC}} \tag{2.4}$$

The cell's efficiency, η, is given by P_m as a fraction of the incident light power density P_s and is related to J_{sc} and V_{OC} through FF (Eq. 2.4):

$$\eta = \frac{P_m}{P_s} = \frac{J_{sc}V_{OC}FF}{P_s} \tag{2.5}$$

All the parameters in Eq.2.5 should preferably be deduced under the standard test conditions (STC) and included when reporting solar cell performances. STC for solar cells is; a cell temperature of 25 ^{o}C and $P_s = 1000\,Wm^{-2}$, with an air mass 1.5 (AM1.5) spectrum.

The photo-generated current, J_{sc} is dependent on the incoming radiation on the cell and can be described with the relation:

$$J_{sc} = q \int b_s(E)QE(E)dE \tag{2.6}$$

Where QE(E) is the probability of an incident photon with energy, $E = hv$, to deliver one electron to the external circuit, q is the elementary charge, b_s(E) is incident photon flux, the number of incident photons in an area in a unit of time with the energy E + dE. From a measurement of the photo-generated current with the illumination of monochromatic radiation with a

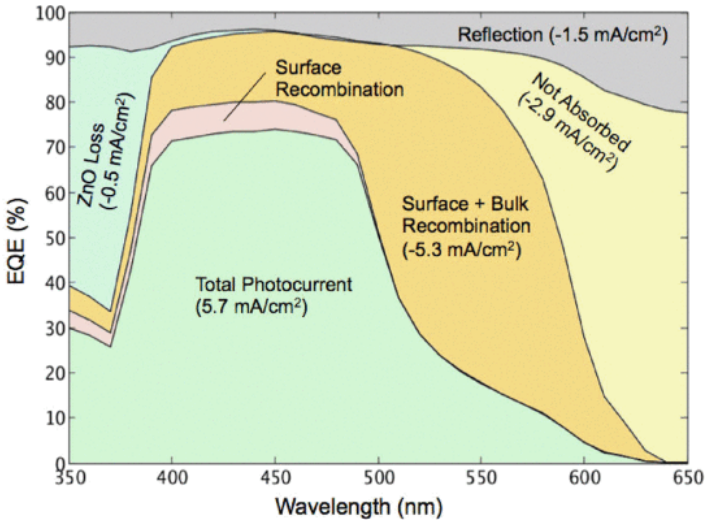

Figure 2.11: EQE of a representative Cu_2O device broken down in fractions by reflection losses, incomplete absorption, and incomplete collection of photogenerated carriers.[18] Reprinted from [18] © 2013 IEEE.

constant power density, an external quantum efficiency (EQE) can be deduced for different wavelengths. The EQE depicts the probability that incoming photons with a given wavelength successfully contribute one electron to the extracted current. The EQE is defined as:

$$EQE(E) = (1 - R(E))\eta_{coll}(E)\alpha(E) \tag{2.7}$$

where R(E) is the reflectance, η_{coll} is the collection efficiency, and $\alpha(E)$ is the absorbance. The EQE losses due to reflections, transmittance, and recombination effects are illustrated in Fig. 2.11 as reported by Brandt *et al.* [18] for a Cu_2O-based solar cell. [88]

Of the different recombination mechanisms, the most common loss mechanisms are described below; i) Band-to-band radiative recombination, ii) Auger recombination, iii) Shockley-Reed-Hall recombination, and iv) interface/surface recombination. (See Fig. 2.12)

i) Band to band radiative recombination occurs when an electron relaxes back to the valence band through radiative emission. It is an unavoidable recombination path that could be viewed as the inverse photon absorption process. It is most important in the limit of an ideal cell, where it is the limiting mechanism for cell efficiency.

ii) Auger recombination is another band-to-band recombination pathway where a carrier recombines across the bandgap. It is a three-particle process mediated through the excitation of a second free carrier, i.e., electron-

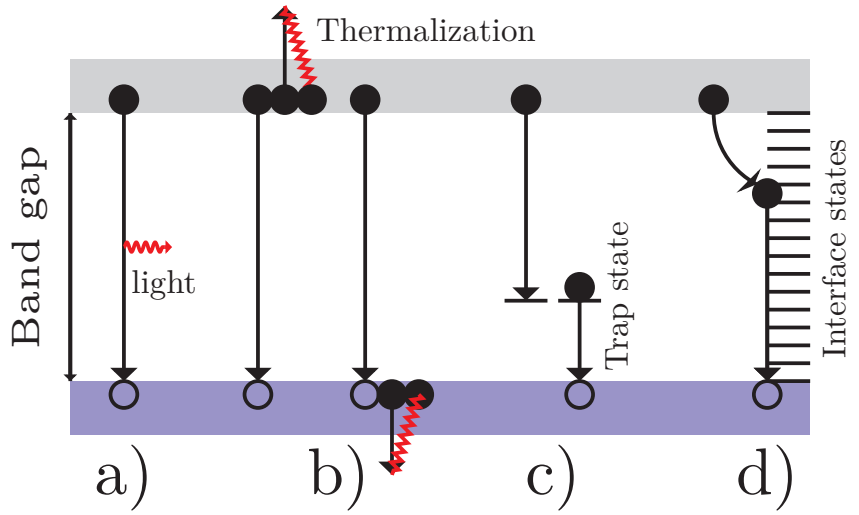

Figure 2.12: Schematic illustration of the four recombination processes discussed a) Radiative recombination b) Auger recombination c) Shockley-Reed-Hall recombination d) interface recombination

electron collision in the conduction band followed by recombination with holes in the valence band. The excited free carrier then thermalizes down to the conduction band-edge, losing its energy as heat to the lattice. Auger recombination depends on carrier density and is usually only a dominating recombination pathway under high injection or in highly doped or low-bandgap semiconductors.

iii) Recombination from defects with trap levels within the forbidden band gap is one of the most common recombination pathways in non-ideal semiconductors. The trap states may originate from, i.e., impurities or other defects such as interstitial, vacancies, dislocations or grain boundaries.[89] The recombination rate is dependent on the free-carrier concentrations and the trap state densities in the material. The recombination process can be described in two steps; first, a free carrier is trapped at the localized trap state before recombining with another carrier of opposite polarity. The nature of the defect distinguishes the traps, i.e., acceptor-like traps are centers that predominantly capture holes, followed by the recombination with free electrons. Likewise, a donor-like trap captures electrons followed by recombination with holes in the valence band. The process is often called Shockley-Reed-Hall (SRH) recombination after the authors who first described the recombination process.[90, 91]

iv) Interface recombination is recombination due to electrically active defect states at the interface or surface of a semiconductor. These are extra

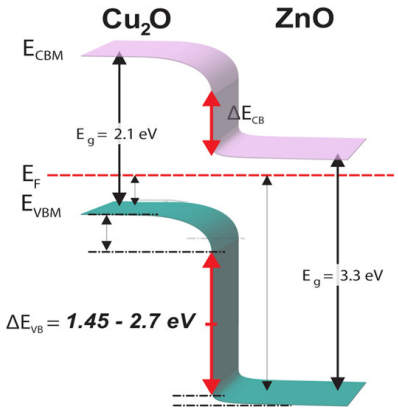

Figure 2.13: ZnO/Cu_2O junction in order to determine the voltage limits of the device. That the ideal built-in voltage and the measured open-circuit voltage are so similar indicates the formation of a near perfect interface.. Reprinted from [93], with permission from ACS Applied Materials & Interfaces

susceptible to high defect densities due to the abrupt termination of the semiconductor crystal. Typically, dangling bonds and impurities introduced from processing are present at higher concentrations at the surface. In Cu_2O, a thin ($\sim 5nm$) strain-induced CuO layer is demonstrated to form at the Cu_2O/ZnO interface, creating additional interface defects. This limits using the ZnO/Cu_2O junction without buffer layers due to high interface recombination at the ZnO/Cu_2O interface.[92]

2.3.2 Efficiencies of Cu_2O Solar cells

The Shockley-Queisser limit for a single-junction solar cell with a bandgap of 2.17 eV restricts the conversion efficiency of Cu_2O absorber-based solar cells to $\sim 20\%$ [94]. This is less than commercially available Si solar cells mass-produced today. Notwithstanding, Cu_2O is an exciting material for solar cell applications due to its high absorption, the abundance of material, non-toxicity, the potential for cheap production schemes, the possibility of flexible substrates, semi-transparent solar cell applications, and suitable band gap for tandem solar cell applications [8, 15, 18]. The scale of current and future PV production puts strict restrictions on candidate constituents. A study by Wadia *et al.* [8] depicts Cu_2O as one of the cheapest PV semiconductors out of 23 candidates to accommodate a worldwide annual electricity production on the terawatt scale. While the bandgap of Cu_2O is too high for high-efficiency single-junction solar cells, it could be well-suited for tandem solar cell applications. Paired with a bottom cell with a bandgap of ~ 1.1 eV yields a Schottky Queisser limit of ~ 40 % [15]. Further, simulation of a

ZnO/Cu_2O top cell with Si-based bottom cell finds that efficiencies up to 31 % are achievable for this configuration. Thus, it could be a commercially feasible route for low-cost, high-efficiency tandem solar cells [17].

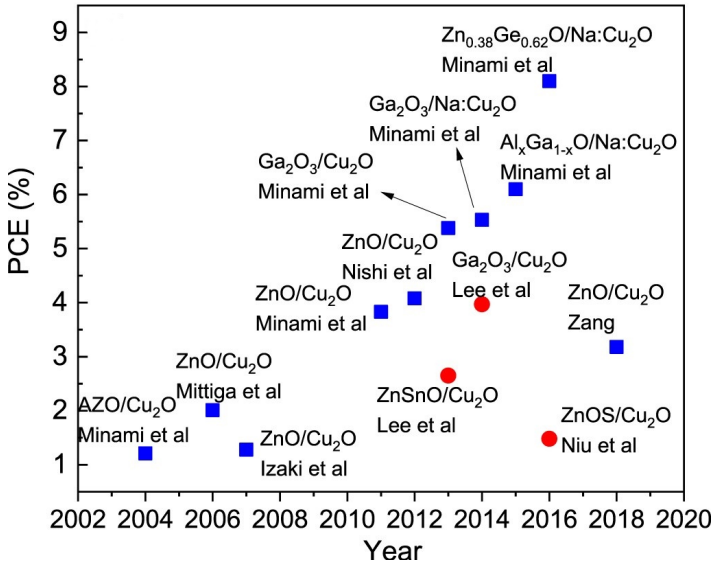

Figure 2.14: Development of Cu_2O based heterojunction solar cells[14, 26, 55, 64, 95, 96, 97, 98, 99, 100, 101, 102]. Blue squares represent cells synthesized on thermally oxidation copper sheets, and red squares represent thin-film devices. Reprinted from [70], with permission from Journal of Physics D: Applied Physics.

The challenges related to n-type Cu_2O outlined in subsection 2.2.4 necessitate hetero-junction cell design with another n-type material since a viable process for n-type Cu_2O is not found. The discontinuity of the valence and conductance band due to differing band gaps, work functions, and electron affinities will influence the carrier transport in the hetero-junction cell. Extra care must be taken concerning band alignment in hetero-junction devices. In the much investigated ZnO/Cu_2O cell, ZnO with a higher bandgap than Cu_2O functions as a window layer with Cu_2O as the active absorber material, where the majority of carrier generation occurs. The hetero-junction between Cu_2O and ZnO is a type II (staggered) hetero-junction, where the valence band of Cu_2O is situated within the bandgap of ZnO. The large band offset between the materials limit achievable cell efficiency from the maximum possible V_{OC} in the device (Fig. 2.13) [103]. Additionally, challenges due to lattice compatibility (strain-induced effects), chemical compatibility, and stability must be carefully considered.

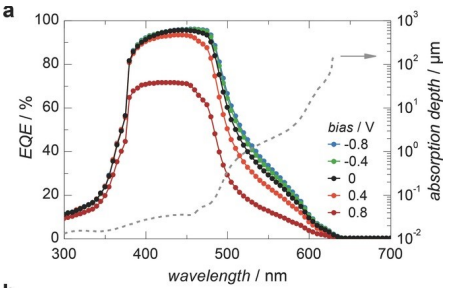

Figure 2.15: The spectra of bias-dependent EQE of Cu_2O device and calculated absorption depth (α^{-1}) [64]. Reprinted from [64] © 2014 Wiley-VCH Verlag GmbH & Co.

The all oxide solar cell comprised of ZnO/Cu_2O is widely studied in the literature. ZnO is another abundant metal oxide, and aluminum-doped ZnO (AZO) is already implemented in the industry as a transparent conductive oxide layer. The progress for ZnO/Cu_2O junctions stalled at $\sim$ 4%; it is shown that the ZnO/Cu_2O interface reduces Cu_2O, forming a defective CuO interface layer impeding cell performance[92, 96]. Additionally, proper band alignment is important for device performance. The low electron affinity of Cu_2O makes many conventional n-type electron selective layers not ideal due to the large conduction band offset between the materials, i.e., ZnO and TiO_2[99, 104]. Consequently, addressing the issue of interface layers and band alignment by replacing ZnO with Ga_2O_3, an $AZO/Ga_2O_3/Cu_2O$ cell showed improved V_{oc} compared to the ZnO equivalent cell [99]. Further pn-interface optimization achieved incremental improvements, and currently, a cell of $MgF_2/AZO/ZnO_{0.38}Ge_{0.62}O/Cu_2O$:Na holds the record efficiency of 8.1 % for Cu_2O hetero-junction cells. Also, here, the main improvement is due to a reduction of the conduction band offset, which leads to a further increase in open circuit-voltage[93, 99] The development of recent Cu_2O hetero-junction solar cell efficiencies is plotted in Fig. 2.14. [70]

Lee *et al.*[64] holds the record efficiency for thin-film Cu_2O solar cells where also Ga_2O_3 is utilized. The best cells have been achieved for both bulk and thin-film in Na doped Cu_2O, which achieves the most favorable electronic properties, such as high mobility, low ionization energy, and controlled doping [55]. Seemingly, much of the improved cell performance up to now have been achieved from pn-junction engineering, prohibiting the formation of interface defect layers, improving band alignment, and reducing interface recombination. Fig 2.15 shows the experimental EQE spectra of the highest efficiency thin-film Cu_2O solar cell[64]. The thin-film cell suffers from poor carrier collection, especially at higher wavelengths, which could be attributed to the relatively low mobility and recombination at the interface and within the Cu_2O layer. Brandt *et al.* [18] suggest that thermal and chemical

treatments will be needed to passivate or remove defects to improve cell performance in Cu_2O devices further.

2.3.3 Simulations of Cu_2O solar cells

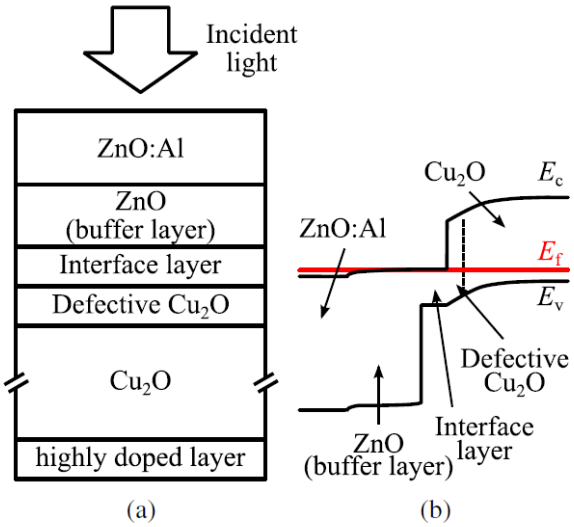

Figure 2.16: (a) Structure and (b) band diagram of the device simulation model. Reprinted from [105].

Technology computer-aided design (TCAD) can be used to model the electrical behavior of semiconductor devices. Several studies on Cu_2O solar cell devices have been conducted in the past.

The effect of the defective layer at the Cu_2O/ZnO interface was studied by Takiguchi and Miyajima with the one-dimensional device simulator wxAMPS to make a realistic model of a Cu_2O device [105]. They used an experimental reference cell (oxidized copper sheet) with an efficiency of 4.13% and tweaked their model to fit the experimental IV and EQE data. The reference cell had the structure ZnO:Al(AZO)/ZnO/Cu_2O. To achieve a good fit, they introduced a defective interface layer and a defective Cu_2O layer at the hetero-junction interface, as shown in Fig. 2.16. This way the model better represented the interface recombination between Cu_2O and ZnO due to strain-induced defects and the formation of CuO at the interface. Further, they showed that efficiencies up to 16% could be reached in an optimized structure with a highly doped back surface Cu_2O layer, a thin Cu_2O absorption layer and a suitable buffer layer. I.e., β-Ga_2O_3 or Ta_2-O_5.

Dumitru *et al.* [106] have investigated the effect of thickness and electron affinity of the buffer layer on the electrical properties of the ZnO/Cu_2O cell. A buffer layer thickness below 0.1 μm and electron affinity between 3.2 eV and 3.7 eV are proposed for optimal cell performance. Also here, β-Ga_2O_3 and Ta_2O_5 are proposed as possible candidates, as well as Zn(O,S) and $Zn_{1-x}Ge_xO$.

Nordseth *et al.* [107] have analyzed the optical properties of a ZnO/Cu_2O top-cell for a silicon-based tandem solar cell structure. They implemented experimental data in the optical simulation model. They report that a $2\mu m$ thick Cu_2O absorber should generate a photo-current of about $10\,mA/cm^2$ under AM1.5G illumination, 80% of an infinite thick Cu_2O layer. Further, an AZO layer thickness of approximately 80 nm gave the lowest reflectance and high transmittance for the ZnO/Cu_2O solar cell.

Chapter 3

Methods

The work included in this thesis is mainly experimental, except for TCAD simulations through the SILVACO software, which is presented in section 4.3. The primary fabrication method employed in this thesis is magnetron sputtering. A wide range of characterization methods was used in the thesis. The focus of this chapter will be put on describing the theory behind the three main characterization methods; X-ray diffraction, Hall effect measurements, and thermal admittance spectroscopy. Other characterization methods utilized in section 4 and appended papers are described briefly to overview the techniques. The covered techniques in this regard are Rutherford backscattering spectrometry (RBS), secondary ion mass spectrometry (SIMS), UV-vis measurements, and cathodoluminescence (CL).

3.1 Magnetron Sputtering

Sputter deposition is a thin-film deposition method widely used in the thin-film industry, where the material is physically ejected from one or more so-called targets. Lumps of the desired materials comprise the targets for deposition. It is a versatile deposition method where several targets or reactive gases can be introduced to achieve compound materials and alloys. The target material (cathode) is bombarded by ionized atoms (typically Ar^+ ions) accelerated in a vacuum during the sputtering process. Upon impact with the target surface, there are several possible outcomes.[109]; At low energy (>10 eV), the ion may bounce off the surface back into the chamber, or it could transfer its energy to phonons (heat) and adsorb to the surface. At high energies (>5keV), the ions are implanted deep into the substrate. Finally, in the intermediate range, the ions will transfer their energy both to heat and from physically rearranging the target material atoms. A collision cascade within the top atomic layers occurs, as illustrated in Fig 3.1, which results in partial ejection of atoms and clusters from the target material. On the substrate (Anode) facing the target, the ejected material will then adsorb, and ultimately a thin film may form. High adatom mobility is desired for quality thin-film growth, and the impinging adatoms achieve typical energies of 10-50 eV, which is over 100 times more than evaporated atoms[109]. High adatom energy increases the probability of finding the energetic minima at the deposited surface, facilitating good film quality and step coverage.

An inert gas is "ignited" when a voltage is applied in the chamber or electrons are injected through a filament to achieve the plasma. When the

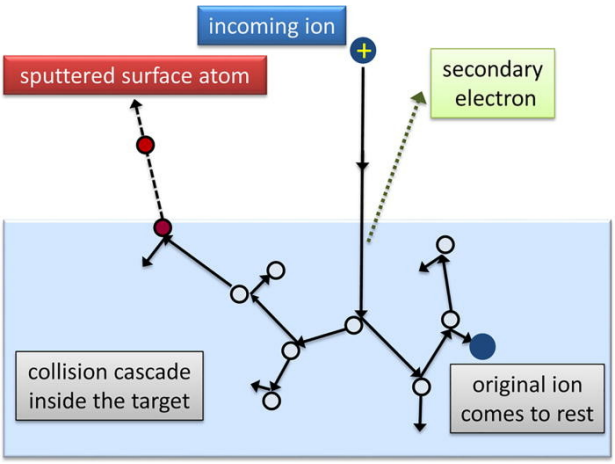

Figure 3.1: Schematic illustration of possible outcomes for an incident ion on the target material. Reprinted from [108], with the permission of AIP Publishing.

plasma is ignited, the ionized atoms are accelerated towards the cathode. Upon bombardment, secondary electrons emitted from the target surface are then accelerated towards the anode, ionizing additional Ar atoms in its path. Secondary electrons play an essential role in maintaining the plasma, and in magnetron sputtering, the ionization from secondary electrons is amplified when a magnetic field is applied. When subjected to the magnetic field, the electrons spiral around the magnetic field lines, which increases their effective path lengths, increasing the likelihood of ionization of neutral species in the chamber. Increased plasma density results in a higher deposition rate and gives greater flexibility, as the plasma can be sustained at lower chamber pressures, which is typically desired for optimal crystal growth. The energy of the ions is controlled mainly by the applied voltage (V), while the number of impinging ions is proportional to the discharge current (I). The discharge power (P), commonly cited for sputter processes, comprises the product of the two, P=IV.

3.1.1 Thin Film Growth

Upon arrival to the substrate, the adatom may adsorb or reflect off the surface. Adsorbed atoms are loosely bound by Van der Waal forces (0.01-0.1 eV) to the surface, allowing them to diffuse along the surface until they are incorporated into the crystal. When the diffusing atoms meet other atoms or nuclei, they cluster together and may grow until it reaches a critical size. The critical size is the largest dissociable atom cluster, so in clusters larger

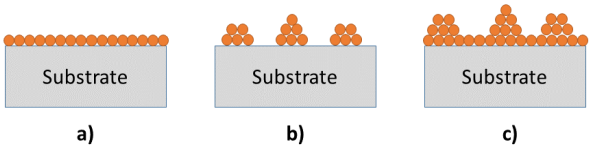

Figure 3.2: Modes of film growth: a) Frank–Vander Merwe layer growth b) Volmer–Weber island growth, and c) Stranski-Krastanov layer plus island growth.

than this, the atoms are stable and immobile, i.e., their center of mass does not diffuse further. By maintaining high surface mobility, the clusters will continue to grow, and if the island merges while still very thin, smooth continuous films may form. [109] Depending on the material's affinity and growth conditions, the clustering process can be described by the three growth types as illustrated in Fig. 3.2; a) Frank Van der Merwe (layered growth), b) Volmer-Weber (island growth), or c) Stranski-Krastaniv (layer plus island growth). The clustering of the atoms at the surface is determined by the adatom mobility (temperature and ion energy) and the chemical reactions at the surface. In Frank Van der Merwe growth adsorbing atoms favor growth directly at the surface, forming well-defined smooth layers. In Volmer-Weber island growth, there is a higher affinity between the adatoms than between the adatom and the substrate surface. Consequently, the nucleation process is favorable by clustering together in an "island" to reduce the surface exposed to the substrate. In the third case, Stranski-Krastaniv growth is a combination of the former types, which occur due to the relaxation of elastic stress.[110] In the initial growth layers, the film follows Frank Van der Merwe layered growth conditions, up to some critical layer thickness. The energy difference overcompensates the extra surface energy exposed to the 3D crystallites, and it becomes energetically favorable for Volmer-Weber island growth to reduce the stress. [110] For sputter deposition, the growth has been divided into a zone model describing the effect of process conditions such as substrate temperature normalized by the deposited materials' melting point, argon pressure (Pa), and incident ion energy (eV). Movchan and Demchishin first proposed the Zone model before a modified approach, as illustrated in Fig. 3.3 was adopted by Thornton, where he divided the growth into four zones. The model is broadly applicable to materials that crystallize; however, the zone borders may vary.[109] In zone 1, the adatom mobility is low due to low temperature and ion energy. This is unfavorable for uniform crystal growth, which results in amorphous, highly porous growth with a low mass density. At higher temperatures in the T zone, the adatom mobility is higher,

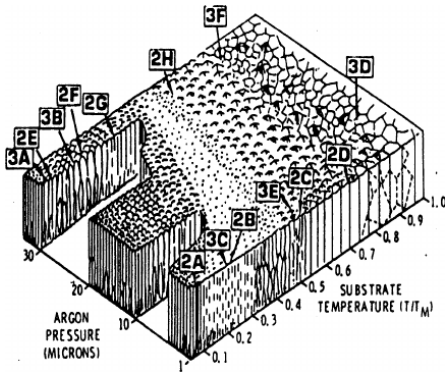

Figure 3.3: Schematic representation of the dependence of coating structure on substrate temperature and argon pressure as presented by Thornton. Reprinted from [111], with permission from AIP Publishing.

leading to denser films with very small grains. In zone 2 at even higher temperatures of about $> 0.5\ T_m$, the adatom mobility is high enough for the atoms to diffuse between grain boundaries. The zone produces narrow-tall columnar grains. Finally, at high temperatures in Zone 3, large 3D grains may form, suggesting bulk diffusion in addition to surface diffusion. This is often the desired zone to avoid crystal defects and achieve optimal device performance.[109]

3.2 X-ray Diffraction

X-ray diffraction (XRD) is a crucial tool for determining the structure of crystalline materials. It has been involved in the characterization of all samples prepared in this thesis to confirm that the desired phase, Cu_2O, is achieved from the growth process. In addition to phase analysis, it has been used to deduce lattice parameters and crystallographic orientations and to indicate crystallite size variation in the films.

Three main interactions occur between incident x-rays on a solid; inelastic scattering through photo-ionization, the related Compton scattering including the re-emission of x-rays at lower energy, and finally, Thompson scattering, an elastic scattering mechanism involving collective oscillation of the electron "cloud" at the frequency of incident x-rays as a hertz dipole, results in re-emission of x-rays at approximately the same frequency as the incoming x-rays. X-rays are photons with high energy, 125 eV - 125 keV or a wavelength of $\lambda \sim 0.01 - 10nm$. This is on the same order of magnitude as the inter-atomic distances in crystals and molecules. Therefore, constructive and destructive interference can be observed for X-rays incident on ordered crystalline structures. The constructive interference has been demonstrated

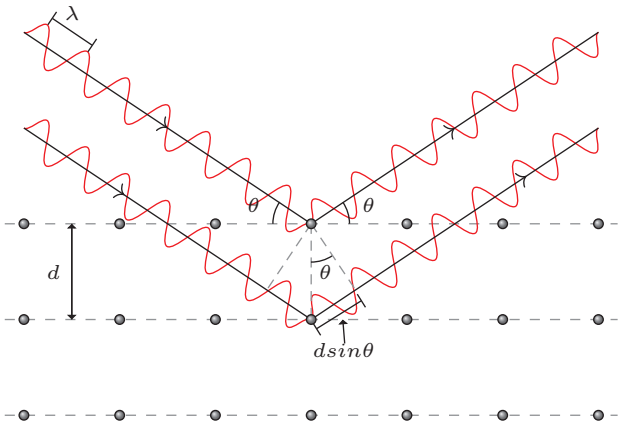

Figure 3.4: Visualization of the Bragg condition, constructive interference when the incident angle θ and plane separation d satisfy the Bragg condition $n\lambda = 2dsin(\theta)$.

to have a maximum intensity when the Bragg condition is satisfied, as illustrated in Fig. 3.4 and described by the relation:

$$d_{h,k,l} sin\theta_B = n\lambda \tag{3.1}$$

where $d_{h,k,l}$ is the inter-planar spacing in the crystal, θ_B angle of incidence, n an integer, and λ the wavelength of incident x-rays (0.1543 nm for Cu_α source). Bragg's law applies to all crystal structures and can be used to determine the inter-planar spacing and lattice constant for known unit cells. In the case of Cu_2O with a cubic unit cell, the lattice constant can be deduced through the relation:

$$d_{h,k,l} = \frac{a}{h^2 + k^2 + l^2} \tag{3.2}$$

where $d_{h,k,l}$ is the inter-planar spacing found in Eq. 3.1, a is the lattice constant, and 'h, k, and l are the miller indices of the investigated reflection.

In a Bragg-Brentano scan, the reflected intensities are measured as a function of the angle between the incoming and diffracted beam. This is achieved by moving the detector around the circumference of the sample stage. The resulting diffractogram can be used as a material "fingerprint". This way, the diffractogram can be utilized to determine phases present in the material when compared to a reference, i.e., the International Centre for Diffraction Data database.

The crystallite size can be estimated by the Scherrer's formula from the line widths of the x-ray Bragg peaks and is given by the relation:

$$D = \frac{K\lambda}{\beta Cos\theta} \tag{3.3}$$

where D is the crystallite size, K the Scherrer constant (0.9 for spherical particles), $\lambda = 0.1543\,nm$ the X-ray wavelength, and θ the FWHM from a gaussian fit on the investigated peak in radians. The Scherrer formula is widely adopted to deduce crystallite sizes in polycrystalline materials. However, the crystallite size deduced from the Scherrer equation should be used cautiously in this regard. Since the equation is originally deduced for spherical particles, effects such as the non-spherical shape of the crystallites, stress/strain, non-uniform crystallite sizes, and other peak broadening effects will impact the analysis.

For the XRD measurements in this thesis, a Bruker AXS D8 Discovery XRD system was employed in the Bragg-Brentano geometry, and a $CuK_{\alpha 1}$ radiation source was selected by a GE(002) asymmetric monochromator on the primary beam side.

3.3 Hall Effect Measurements

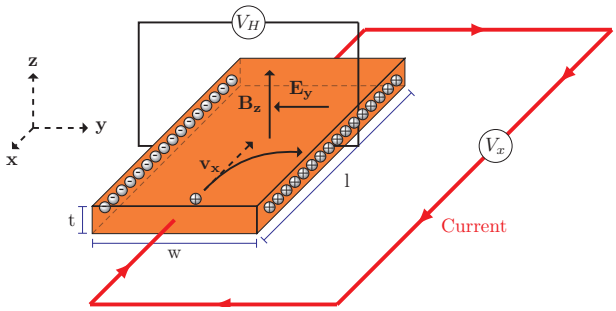

Figure 3.5

Hall effect measurements determine carrier density and Hall carrier mobility when performed in unison with a resistivity measurement in semiconductor materials. The Hall effect arises when moving charge carriers interact with a magnetic field due to the Lorentz force. In an experimental setup, the interaction of the magnetic field is aligned perpendicular to the moving charge and is then observed due to charge carrier accumulation. Therefore, an opposing electric field E_y is generated as illustrated in Fig. 3.5. When equilibrium is reached, the field can be described through:

$$E_y = v_x B_z \tag{3.4}$$

Where v_x is the carrier drift velocity and B_z is the applied magnetic field. The drift velocity can be expressed as $v_x = \frac{[J_x]}{qp}$, where J_x is the current density, q the charge, and p hole carrier concentration in the case of p-type material. Combined, the field can be given as:

$$E_y = R_H J_x B_z \tag{3.5}$$

where the Hall coefficient is defined as $R_H \equiv \frac{1}{qp}$. When conducting a measurement with the known magnitude and direction of both the current (I_x), the magnetic field, and the Hall voltage ($V_H = E_y w$, where w is the width of the sample), one can now determine the carrier density and deduce its polarity from the sign of V_H from:

$$p = \frac{1}{qR_H} = \frac{I_x B_z}{qV_H t} \tag{3.6}$$

where t is the thickness of the conducting layer. By pairing the measurement with a resistivity measurement, typically a Van der Pauw measurement which can use the same contact geometry as the Hall measurement, the hole mobility, μ_p, is found through the relation:

$$\mu_p = \frac{1}{\rho qp} = \frac{R_H}{p} \tag{3.7}$$

3.3.1 Temperature-Dependent Hall Effect Measurements

The temperature-dependent Hall effect can be used to examine electrical transport properties such as carrier mobility limiting mechanisms, and from the carrier density, the acceptor (or donor) activation energies can be deduced. Additionally, in compensated semiconductors, an estimation of the compensating donor densities can be made. Cu_2O is a predominant p-type semiconductor that is assumed to be heavily compensated. For a non-degenerate compensated semiconductor with N_a acceptors, the charge neutrality equations can be given as:

$$p + p_A = N_a - N_d \tag{3.8}$$

where p is the hole concentration, N_d is the concentration of net compensating donors, and p_A is the concentration of non-ionized acceptors. The temperature dependency of p and p_A is given by:[112]

$$p_A = N_A \frac{1}{1 + \beta exp\{\frac{E_f - E_A}{k_B T}\}} \tag{3.9}$$

and

$$p = N_V(T)exp\{-\frac{E_f - E_V}{k_B T}\} \tag{3.10}$$

which then can be combined together with Eq. 3.8 and be expressed as:

$$\frac{p(p+N_d)}{N_a - N_d - p} = \beta N_V exp(-\frac{E_V + E_a}{k_B T}) \tag{3.11}$$

where β is the degeneracy of the acceptor level. Eq. 3.11 can be solved analytically by the quadratic equation or numerically to fit Na, Nd, and E_a to the experimental data. In three limiting cases, the equation can be simplified;

In samples at high temperatures where $k_B T >> (E_a - E_V)$, the carrier concentrations equals the ionized acceptor concentration ($p > N_a > N_d$) yielding the solution $p = (N_a - N_d)$.

At lower temperatures under incomplete ionization where $N_d < p < N_a$, the carrier density can be simplified as:

$$p \simeq g_a(N_v N_a)^{1/2} exp(\frac{E_a}{2k_b T}) \tag{3.12}$$

Finally, lowering the temperature further leads to a compensated material where $p < N_d < N_a$, the hole carrier density can, in this case, be expressed by the relation [112]:

$$p \sim \frac{\beta N_V (N_a - N_d)}{N_d} exp(-\frac{E_a - E_V}{k_B T}) \tag{3.13}$$

In the case of two acceptors, N_{a1} and N_{a2}, and a net compensating donor concentration N_d the charge neutrality equation can be solved for p through the relation: [113, 114]

$$p + N_d = \frac{N_{a1}}{1 + \frac{p}{g_{ai} N_v e^{-E_{a1}/k_b T}}} + \frac{N_{a2}}{1 + \frac{p}{g_{ai} N_v e^{-E_{a2}/k_b T}}} \tag{3.14}$$

Eq. 3.14 can further be rewritten in the form of the cubic equation $ap^3 + bp^2 + cp + d$. The TDH parameters can then be deduced from a least-square fitting of the positive solution of Viéte's trigonometric expression;

$$p(T) = 2\sqrt{-\frac{s}{3}} cos\left(\frac{arccos\left(\frac{3q}{2s}\sqrt{\frac{-3}{s}}\right)}{3} - k\frac{2\pi}{3}\right) - \frac{b}{3a} \tag{3.15}$$

Here, $s = \frac{c}{a} - \frac{b^2}{3a^2}$ and $r = \frac{2b^3}{27a^3} + \frac{d}{a} - \frac{bc}{3a^2}$.

The temperature-dependent mobility data is an important tool to describe the electric properties of a material. The different scattering mechanisms

used to estimate the mobility data in this thesis are estimated through the relations:

Longitudinal optical (LO) high-frequency phonon scattering as deduced by Shimada et *al.* [84]:

$$\mu_{LO_1} = 268(e^{220/T} - 1)\, cm^2/Vs \tag{3.16}$$

Longitudinal optical (LO) low-frequency phonon scattering as deduced by Shimada et *al.* [84]:

$$\mu_{LO_2} = 102(e^{951/T} - 1)\, cm^2/Vs \tag{3.17}$$

Ionized impurity scattering:

$$\mu_i \propto \frac{\alpha T^{3/2}}{e^{-E_a/kT}} \tag{3.18}$$

where α is a proportionality coefficient, and E_a is the activation energy. Both the Conwell-Weisskopf and Brooks-Herring approximations[87] state that μ_i is inversely proportional to the concentration of ionized impurities and roughly proportional to $T^{3/2}$. The concentration of ionized impurities, N_i, is assumed to strongly increases with temperature as an activation-type dependence: $N_i \propto exp(-E_a/kT)$.

Finally, the total mobility in the system can be summed and fitted following Matthiessens's rule:

$$\frac{1}{\mu} = \frac{1}{\mu_n} + \frac{1}{\mu_i} + \frac{1}{\mu_{LO_1}} + \frac{1}{\mu_{LO_2}} \tag{3.19}$$

The room temperature and low temperature (20-300K) Hall effect data presented in this thesis were collected in a Lakeshore 7604 setup utilizing soldered indium contacts on four corners of the sample. A second Lakeshore 7604 setup fitted with a furnace (300-700K) and sample holder fitted with probe needles was utilized for high-temperature measurements.

3.4 Thermal Admittance Spectroscopy

Thermal admittance spectroscopy (TAS) is a characterization technique for majority carrier traps. The capacitive trap state contribution is probed in semiconductors by a small AC bias. Unlike TDH measurement, which probes the net majority carrier density, TAS probes the capture/emission process of

discrete majority traps in the bandgap. The capacitive response as a function of frequency, temperature, and voltage can determine trap parameters such as capture-cross section, trap density, and trap energy level relative to the band edges.

The admittance describes the current flowing in response to the small probing voltage. Admittance can be written as the sum of the contribution from in-phase conductance G(ω) and out-of-phase susceptance S(ω):

$$Y(\omega) = G(\omega) + iS(\omega) \tag{3.20}$$

where i is the imaginary number, and the capacitance is given from $C = \frac{S(\omega)}{\omega}$.

At different temperatures, the trap capture/emission process resonates with the probing frequency, resulting in trap signatures observable as local maximums on the conductance curves or steps in the capacitance curve. By extracting the temperature of maximums or inflection points of these signatures and plotting $ln(\pi f/T_{max}^2)$ vs. $1/T$, energy position relative to the band edges and capture-cross section of the traps can be deduced from the relation [112]:

$$\frac{2\pi f}{T_{max}^2} = e^{-\frac{\Delta E_t}{k_b T_{max}}} + 2\pi\sigma_j\nu_{th}N_V \tag{3.21}$$

T_{max} is the temperature of maximum conductance/inflection points, ΔE_t the trap energy level relative to conduction/valance band, k_b Boltzmann constant, and f the probing frequency. Here we assume $N_V \propto T^{3/2}$ and $\nu_{th} \propto T^{1/2}$, which gives the T dependency in Eq. 3.21.

The Cu_2O films investigated in this thesis are deposited on moderately doped Si substrates. Due to the high acceptor concentration in the films, the depletion region zone is expected to extend predominantly into the Si substrate at room temperature. Therefore, the trap concentration in Cu_2O cannot be determined from TAS measurements. See Fig. 3.6 for schematic band diagrams and illustrated depletion width, *W*. At lower temperatures, the acceptors in Cu_2O freeze out. Consequently, the capacitance falls to the geometric capacitance. Calculating the apparent trap concentration assuming $N_t \propto \frac{dC}{dT}$ and $C = -\frac{\epsilon_r A}{W}$ corroborates with this assumption, resulting in $N_t \simeq 3 \pm 2 \times 10^{15}$ in all samples. This is in good agreement with the Si phosphorous doping concentration of $1 \times 10^{15} cm^{-3}$. Here we used $W = \sqrt{\frac{2\epsilon_r V_0}{qN_t}}$, where A is contact area, ϵ_r permittivity, q elemental charge, and V_0 built-in bias deduced from room temperature CV measurements [115].

The observable range of trap energies is governed by the demarcation energy and the Fermi level position. Only the trap levels crossing the Fermi level in the transition region contributes to the capture/emission process and measured capacitance. Demarcation energy defines the depth a trap can be

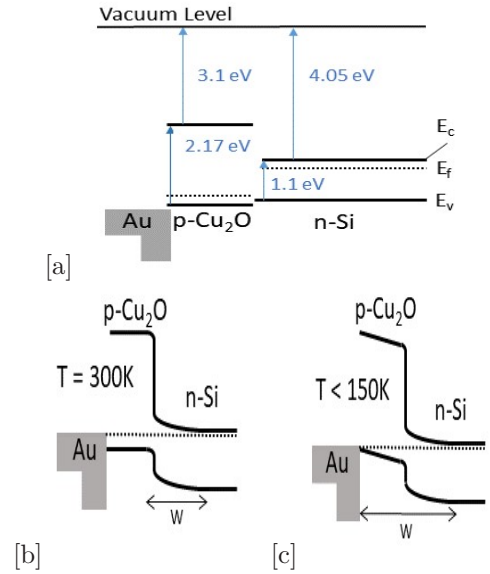

Figure 3.6: a) Schematic band diagrams of Cu_2O and Si before contact b) Cu_2O/Si junction at room temperature c) Cu_2O/Si junction at low temperature where we assume carrier freeze out in the Cu_2O film. The depletion width is indicated by W.

probed at given an ac modulation frequency f and temperature T. It can be derived from Eq. 3.21 as:

$$E_\omega = kT\, ln(\frac{\nu_{th}\sigma_j N_V}{\omega}) \tag{3.22}$$

Where v_th is the thermal velocity, ω is the AC modulation frequency, and E_ω is the deepest energy relative to the valence band in the case of an acceptor. In our investigations, a frequency range of 1kHz-1MHz and a temperature range of 50-300K were employed. From Eq. 3.22 one can deduce acceptor traps up to 0.25-0.41eV above the valence band for traps with capture cross-sections in the range $10^{-15} - 10^{-17} cm^{-2}$.

The thermal admittance spectroscopy measurements performed in this thesis were achieved with an Agilent 4280A LCR meter, while the temperature was swept from 50K - 300K.

3.5 Uv-vis Measurements

Uv-Vis measurements were employed to determine the transmittance of the deposited samples. During operation, the incident light I_0 is compared to the

transmitted intensity I_t after the addition of a sample to the beam path. The transmittance is then given as; $T = \frac{I_t}{I_0}$. Gratings are used to "step" through the light-beam wavelengths to achieve a transmittance spectrum from UV into the visible part of the spectrum.

Tauc plot analysis can be used to investigate the optical bandgap of semiconductors. The Tauc analysis deduces the bandgap from the intersection of the sharp increase in absorption for incident light with energy above the bandgap of the material. Generally, the absorption coefficient α can be determined from the transmittance using the relation:

$$T = \frac{(1-R)^2 e^{\alpha d}}{1 - R^2 e^{-2\alpha d}} \tag{3.23}$$

where R is the reflectance and d is the sample thickness. In the following calculations regarding α, the reflectance is omitted, assuming little effect on the slope near the absorption onset. Since the aim was to investigate the trend over absolute values, this was deemed acceptable. As previously mentioned in Section 2.2 the absolute value of the optical bandgap in Cu_2O is poorly estimated by the assumption of a single dominating transition.[38]

The Tauc relation is given as:

$$(\alpha h\nu)^{(1/n)} = A(h\nu - E_g) \tag{3.24}$$

where h is Planck's constant, v is the photon frequency, A is a proportional constant, and r is a constant, which depends on the type of transition. For direct allowed transitions n=1/2, whereas for indirect allowed transitions, n=2. The apparent bandgap can then be deduced from the intercept of the energy axis.

In this thesis a Shimadzu Solid Spe-3700 DUV spectrophotometer was used in the spectral range 290 - 2500 nm with a 1 nm step size.

3.6 Secondary Ion Mass Spectrometry

Secondary ion mass spectrometry (SIMS) analyses the atomic masses of ions emitted when sputtering a material surface. It can detect the presence and distribution of elements in materials down to sub-parts per billion and has a dynamic range of $\sim$ five orders of magnitude. The three most common measurement methods are; mass spectrum, depth profiling, and imaging.

A primary beam of high-energy ions, consisting of O_2^+ or Cs^+ at 5-15 keV, is used to sputter the target material during operation. Atoms, clusters, and ions are then dislodged from the sputtered target. The fraction of the ejected material which is ionized is accelerated towards a mass spectrometer made up of an electrostatic and magnetic analyzer, which separates the secondary ion beam by their mass to charge ratio. The filtered beam is then guided to a detector that measures the ion current. A plot of mass to charge ratio

vs. intensity is achieved by sweeping the mass spectrometer's magnetic field strength. The resulting mass spectrum can be used to deduce the elements present in the sample. A depth profile is achieved by sputtering in the same place. When assuming constant sputtering yields, the sputtering time can be converted to depth by measuring the crater depth after the measurement. The intensity of the recorded ion current can be converted to concentration by measuring a reference sample of the same material (matrix/lattice) with a known concentration of the element of interest. This is commonly achieved by ion implantation in a reference sample.

The SIMS measurement was performed in a Cameca IMS7f microanalyzer with O_2^+ ions at 10keV and Cs^+ ions at 15keV.

3.7 Cathodoluminescence

Cathodoluminescence probes radiative relaxation pathways in a material by bombarding the material with electrons (cathode ray) and analyzing the emitted photons. It can reveal valuable information about band structure, crystal quality, defect structures, and impurities. Similar to other luminescence methods, CL spectra are collected with a spectrophotometer to achieve photon energy vs. intensity spectra. CL is often included in a scanning electron microscope, which already has the cathode ray. This way, both structural and optical properties can be studied in the same system. The high energy of impinging electrons allows multiple excitation paths and a broad spectra investigation from near-infrared up to UV radiation. The radiative relaxation process emits a photon, which has characteristic energy related to the relaxation pathway. In an imperfect crystal, there is an increased probability of non-radiative recombination of the excited electron-hole pair through phonon-assisted recombination.

High resolution of near band emission (NBE) is generally linked to high crystalline quality. NBE emissions are sharp emission lines due to a combination of free-electron relaxation between the bands across the bandgap and emissions related to the relaxation of excitons. Additionally, luminescence from deeper defects within the bandgap allows for defect characterization from CL measurements.

The CL measurement was performed in a JEOL JSM-IT300 SEM with a Delmic SPARC CL system. The spectra were recorded with acceleration voltages of 3, 5, 10, and 20 keV and a probing current of 100 pA at 80 K.

Chapter 4

Summary of Results

The focus of this thesis has been to investigate Cu_2O and especially its electrical properties. The work includes a study on natural bulk Cu_2O crystals investigated with complementary techniques to study dominating electronic centers and carrier transport in Cu_2O. Further, a study of Li doping is conducted to investigate its influence on sputtered Cu_2O properties. Finally, simulations are performed to elucidate the effect of high acceptor concentrations in Cu_2O-based solar cells.

4.1 Dominant defect complexes in single-crystal Cu_2O

In paper I, we study the dominant electrically active centers and carrier mobility in commercially available natural single crystal Cu_2O wafers from SurfaceNET. The wafers had 111-orientation, a size of 1x1 cm^2 with a thickness of 500 μm, and resistivity of 20 $k\Omega cm$ at room temperature. The single crystals were investigated by XRD, SIMS, CL measurements (Fig. 4.1), TDH (Fig. 4.2), and TAS (Fig. 4.5). SIMS measurements of hydrogen and nitrogen concentrations were conducted with reference samples to quantify the concentrations in the Cu_2O wafers studied. The measurements revealed high impurity concentrations in the wafer: $3 \times 10^{19} cm^{-3}$ and $7 \times 10^{17} cm^{-3}$ for hydrogen and nitrogen, respectively.

4.1.1 Optical transitions

The CL measurements reveal five near band emission (NBE) signatures (Fig. 4.1), which is in good agreement with previous reports on high-quality Cu_2O films from photo-luminescence measurements. [37] The lines are attributed to the orthoexcitonic emission coupled with various of phonon-emission and absorption combinations listed in Table 4.1. We note that for peak 1 the

Table 4.1: NBE transitions in CL at 80K and their tentative assignments.

Peak	Energy position (eV)	Assignment
1	1.891	$X_O - \Gamma_{25}^{+} - \Gamma_{15}^{-2} \rightarrow \Gamma_7^{+}$ or $(N_2)_{Cu}$
2	1.950	$X_O + \Gamma_{15}^{-2} \rightarrow \Gamma_7^{+}$
3	1.974	$X_O + \Gamma_{25}^{+} \rightarrow \Gamma_7^{+}$
4	2.018	$X_O - \Gamma_{12}^{-} \rightarrow \Gamma_7^{+}$
5	2.043	$X_O + \Gamma_{12}^{-} \rightarrow \Gamma_7^{+}$

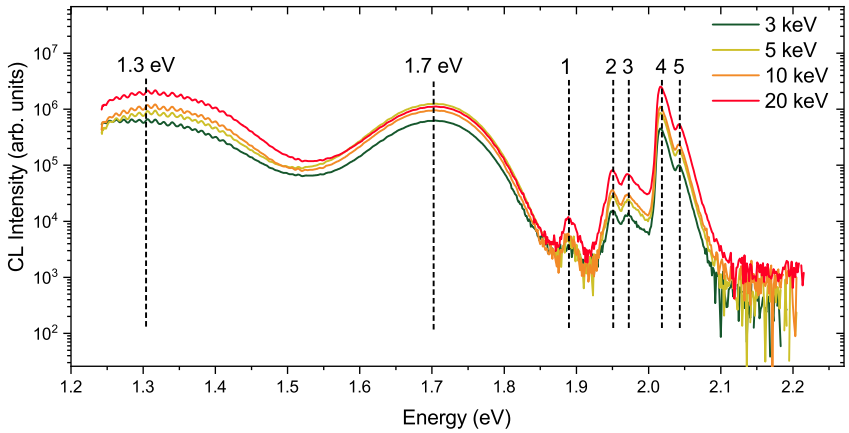

Figure 4.1: CL at 80 K in the photon energy range 1.2-2.2 eV recorded for different electron-beam energies: 3, 5, 10 and 20 eV. Five NBE lines and two mid-gap deep emission lines are indicated on the plot. Reprinted from paper I

emission could also be a good match with reports on nitrogen-related centers. [53, 54].

Two broad and strong luminescence bands are observed around 1.3 and 1.7 eV in Fig. 4.1. These are well documented in the literature and routinely assigned to V_{Cu} and V_O^{2+}, respectively.[19] However, these assignments contradict DFT calculations and reports of the V_{Cu} and V_{Cu}^{split}, which are believed to be responsible for acceptor levels at $\sim$ 0.2 eV and 0.47 eV above the valence band.[42, 49, 50] Firstly, V_O^{2+} is predicted to be electrically neutral without electronic levels in the bandgap. Secondly, the assignment of V_{Cu} to the band at 1.3 eV (i.e., $\sim$ 0.8 eV above the valence band) would contradict theoretical and experimental results, which tend to assign it to the level at $\sim$ 0.2 eV above the valence band. Accordingly, the deep emission level at 1.7 eV is tentatively assigned to the V_{Cu}^{split}, which is predicted at 0.47 eV above the valence band (E_G - 1.7 eV). [41, 42, 49] The line at 1.3 eV is in contrast to the identification in literature as V_{Cu}, speculated to be related to the acceptor state of a hydrogen-V_{Cu} complex. Hydrogen is found to be abundant in the studied samples, as shown by SIMS (Fig. 2.9). The photon energy of 1.3 eV is close to the energy for the acceptor level of H-V_{Cu}, which was predicted by Scanlon and Watson [39] at $\sim E_V$+1.2 eV.

4.1.2 Temperature-dependent Hall effect measurement

The TDH data of a naturally formed single-crystal Cu_2O are shown in Fig. 4.2. Fitting of the TDH data with a single level to the whole temperature

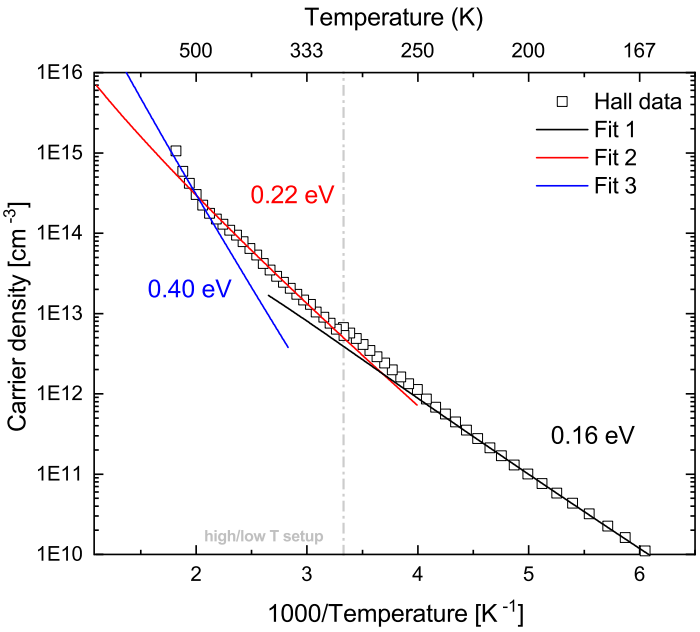

Figure 4.2: TDH results of single-crystal Cu_2O with hole concentration plotted versus the inverse temperature. Reprinted from paper I

range gives activation energy of 0.19 eV. However, we tend to assume two distinct levels, of 0.16 eV to 0.22 eV. The acceptor at 0.22 eV above the valence band (E_V) can be assigned to V_{Cu} with the acceptor level at E_V + 0.25 eV.[42, 49]. According to previous reports, which put the nitrogen level at Ev + 0.12-0.18 eV, the acceptor with the activation energy of 0.16 eV was attributed to nitrogen.[53, 66, 67] A sharp increase in carrier concentration is observed at the higher temperature limit of the measurements. This increase corresponds to an activation energy of $\sim$ 0.4 eV. Two possible explanations can be put forward: (1) there is another deeper acceptor with a level at $\sim$ E_V+0.4 eV, and (2) there is an increase in the concentration of shallow acceptors, which is governed by the formation energy $\sim$ 0.4 eV.[48] Here, the former interpretation is favored. Firstly, a similar acceptor has been observed previously by Paul et al. and Papadimitriou.[41, 42] Secondly, the acceptor level at $\sim$ E_V+0.4 eV is consistent with the results of CL measurements, where the 1.7 eV emission can be attributed to a level at E_C-1.7 eV, i.e., at E_V+0.47 eV. In paper I, we assign this level to V_{Cu}^{split} based on previous reports and theoretical predictions from DFT [41, 42, 49].

The temperature-dependent Hall mobility has a strong dependence on

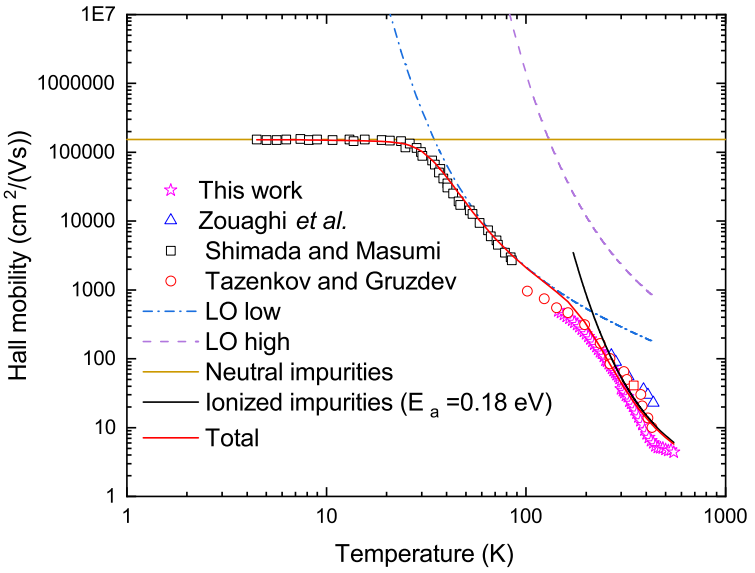

Figure 4.3: Hole mobility in Cu_2O. The data is fitted to the scattering of LO phonon's high and low-frequency modes, neutral impurities (as reported by Shimada and Masumi [84]), and an added contribution from scattering by ionized centers at elevated temperatures. The data digitized from the work of Biccari [25]. [84, 116, 117]

temperature and is shown in Fig. 4.3 Previous studies of hole transport in Cu_2O summarized by Biccari [25] indicate that there was a lack of consistent picture for hole mobility as a function of temperature: In the low-temperature limit, an acceptable agreement could be made from the combination of phonon LO scattering, acoustical phonon scattering, and neutral impurities. However, in the higher temperature range, another dominating mobility limiting mechanism had to be assumed. To account for the observed rapid decline in mobility, the formation of a metastable self-trapped state has been suggested.[84] A similar rapid decline in mobility is reported by Matsuzaki et al. for temperatures above 200 K. In Eq. 3.18, the mobility as a result of ionized centers is described. It is adopted from the Conwell-Weisskopf and Brooks-Herring approximations, which show that carrier mobility has an inverse relation to the concentration of ionized centers and is roughly proportional to $T^{3/2}$ due to the increased thermal velocity of carriers with temperature. The data in Fig. 4.3 show good agreement with this assumption;

utilizing ionization energy of 0.18 eV gives a reasonable and consistent picture between the datasets. The plateau observed in the data of Tazenkov and Gruzdev [117] and in this work could be described by additional ionizing centers or higher neutral impurity concentration compared to the data of Shimada.[84] This is demonstrated in Fig. 4.4, where a full fit is performed for our dataset.

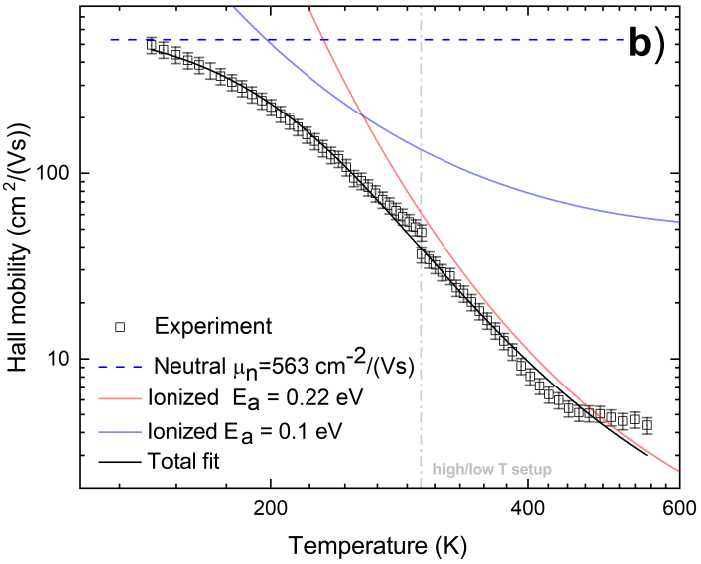

Figure 4.4: Carrier mobility plotted versus temperature. The fitted curves indicate scattering on ionized centers with 0.1 and 0.22 eV activation energies and neutral impurities.

Like the model with several ionizing acceptors from the TDH carrier density data, one could assume several distinct ionization processes influence the scattering mechanisms. A fit of two ionizing centers with the addition of neutral impurities was attempted, and the resulting fit is presented in Fig. 4.4. Two centers with ionization energies in good agreement with the carrier density data of 0.1 eV and 0.22 eV gave the best fit together with neutral impurity mobility of $\mu_n = 563 cm^2/(Vs)$. In this way, the scattering on neutral and ionized impurity centers in the investigated Cu_2O sample could explain the declining mobility observed at elevated temperatures.

4.1.3 Thermal admittance spectroscopy

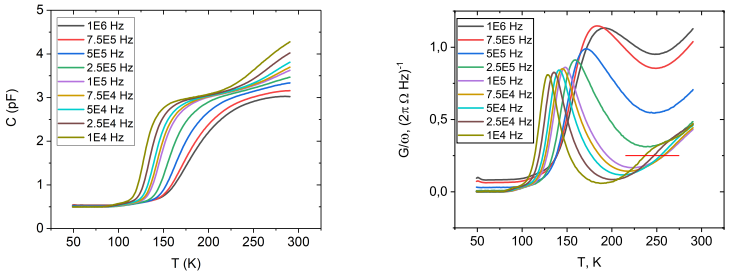

(a) (b)

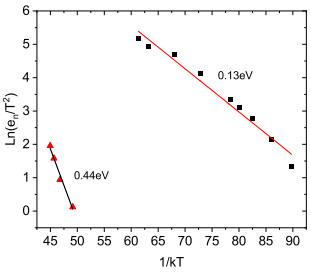

(c)

Figure 4.5: a) TAS Capacitance data plotted versus temperature for 9 different frequencies. b) TAS conductance data plotted versus temperature for 9 different frequencies. c) Arrhenius plot of $\ln(\omega_0/T^2)$ vs. $1/T$ deduced from the G/ω maxima in Fig. 4.5b. The signature of an additional trap level is emerging in the high-level region. A lower estimate of this trap energy level is deduced from the indicated range in plot b).

In Fig. 4.5, the results of TAS measurements on the crystal with capacitance (Fig. 4.5a) and conductance (Fig. 4.5b) as functions of temperature for different frequencies are shown. In Fig. 4.5c, the Arrhenius plot for the emission rates is shown. From the analysis, two dominant electronic levels are evidenced by the two step-like changes in the capacitance measurements or peaks in the conductance measurements. An Arrhenius analysis of the freeze-out labeled E1 results in a level of 0.13 eV. In the high-temperature regime (> 250K), the presence of a deeper level is indicated. A level E2 can be estimated to be ~ 0.4 eV in the indicated area in Fig. 4.5. E1 does not demonstrate a clear Arrhenius dependence. This could be explained by (1) temperature dependence of the capture cross-section or (2) the presence of two overlapping electronic levels similar to the observed results

from TDH measurements. The second assumption results in two levels at 0.09 eV and 0.18 eV, corroborating with the two observed ionization energies retrieved from the TDH measurements. In conclusion, three electronic levels at around E_V+0.09-0.16, E_V+0.18-0.22, and $\sim E_V$+0.4 are suggested in the crystal from TDH and TAS analysis. The levels are suggested as the acceptor states of nitrogen-related centers, copper vacancy (V_{Cu}), and the split-vacancy configuration $V_{Cu,split}$, respectively.

4.2 Magnetron sputter deposited, Li-doped Cu_2O films

4.2.1 Deposition of Li-doped Cu_2O films

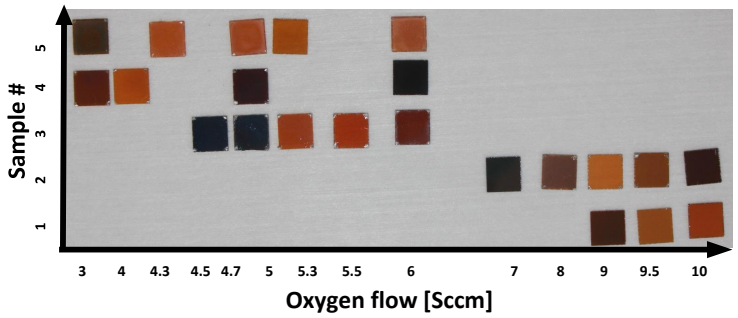

Figure 4.6: Photograph of the samples laid out in matrix, with increasing O_2 flow rate on the x-axis and increasing Li doping on the y-axis.

High-quality Cu_2O is required for the realization of Cu_2O absorber solar cells. Sputtering and electro-deposition are favorable for thin-film deposition due to their maturity within solar cell applications and ease of scalability. The samples presented in this section is used in paper II and III, the films are deposited by DC and RF reactive magnetron sputtering. Common for sputtered Cu_2O films is the challenge of controlling the electrical properties. It is previously reported that the main acceptors in Cu_2O are the copper vacancies, V_{Cu} and V_{Cu}^{split}. By tuning the O_2 flow rate during deposition Cu_xO films with varying phases and stoichiometry can be achieved. However, the sputtered films spontaneously exhibit hole concentrations of $\sim 10^{15} cm^{-3}$ at room temperature [33, 37, 118]. In an attempt to passivate the acceptors present in sputtered Cu_2O, a study on the effect of lithium doping is conducted. Lithium is proposed from a density functional study to suppress copper vacancy formation in Cu_2O, which is believed to be the source of its p-type nature.[52]

In the study, a similar process optimization was carried out for the five different deposition conditions to achieve various Li content in the films (see

Table 4.2: Deposition parameters during the growth of the Cu_2O:Li films.

Sample	#1	#2	#3	#4	#5
Cu target	DC 100W	-	DC 100W	DC 100W	-
$Cu : Li$ target [99.99/0.01 wt%]	-	DC 100W	-	-	-
$Cu : Li$ target [99/1 wt%]	-	-	RF 10W	RF 50W	DC 100W
Argon flow [Sccm]	40.5	41	44.7	45.5	44.5
Oxygen flow [Sccm]	9.5	9.0	5.3	4.5	5.5
Temperature [^oC]	400	400	400	400	400
Rotation [RPM]	12	12	12	12	12
Base pressure [$1x10^{-4}Pa$]	2.7	2.7	2.7	2.7	2.7
Deposition time [min]	15	15	15	15	15
Thickness [nm]	290	380	390	470	430

Table 4.2). A series of samples were deposited, tuning the O_2 for optimal film quality. The trend in XRD, Hall effect and transmittance data was consistent in all the five deposition series, illustrated in Fig. 4.7 with the hall data of sample series #3, #4, and #5. The image in Fig. 4.6 shows how the variation of opacity and phase are clearly visible for samples deposited at different O_2 flow rates. At increasing O_2 flow rates, an initial increase in transmittance and mobility is observed in all the series. The mobility in the films is closely related to their structural properties, and it is found that the mobility in Cu_2O is limited by grain boundary scattering.[119] Additionally, the samples are investigated for phase purity by XRD. By increasing O_2 flow rates further, the inclusion of CuO is first observed through reduced transmittance in the wavelengths below Cu_2O's bandgap, accompanied by a drop in mobility in the films. Finally, at high O_2 flow rates, the CuO phase is also observable in XRD.

The selected films were chosen based on high transmittance, mobility, and phase purity, deduced by UV-Vis, RT Hall measurements, and XRD, respectively. The films where chosen for further characterization to elucidate the effect of varying Li content on structural, optical and electrical properties. I.e., in Fig. 4.7 the samples deposited with an O_2 flow rate of 5.5, 4.5, and 5.5 sccm was selected for series #3, #4, and #5, respectively. Refer to Table 4.2 for a full list of deposition parameters for the selected sample series.

4.2.2 Characterization of $Cu_2O : Li$ films

The results presented in Fig. 4.8 are published in paper II. SIMS measurements plotted in Fig. 4.8a show the Li concentration vs. depth

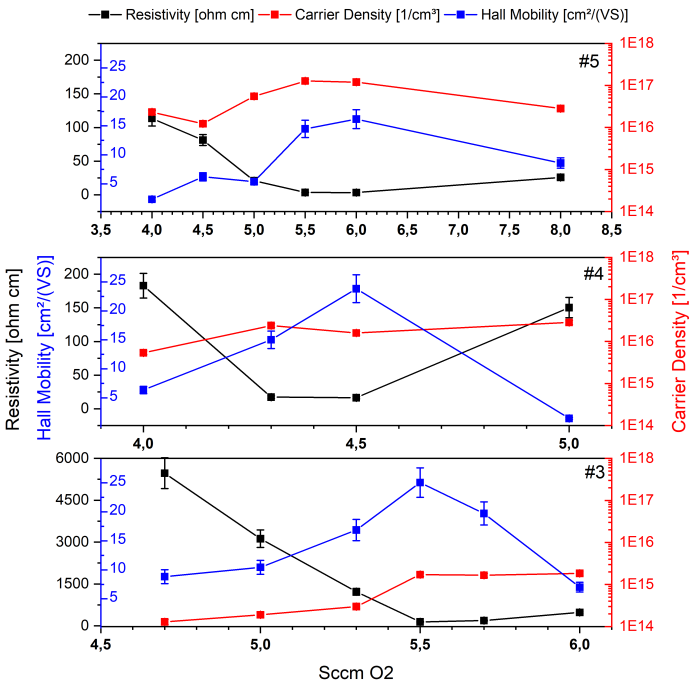

Figure 4.7: Hole density, hole mobility and resistivity of Cu2O:Li samples (#3, #4 and #5) versus oxygen flow during deposition.

for the deposited samples. The un-doped sample (labeled # 1) has Li concentration below the systems detection limit of $< 10^{15} cm^{-3}$). The doped samples, labeled #2-5 after increasing Li content, has Li concentrations of $2 \times 10^{18} cm^{-3}$, $7 \times 10^{18} cm^{-3}$, $2 \times 10^{20} cm^{-3}$, and $5 \times 10^{20} cm^{-3}$, respectively. XRD spectra in Fig. 4.8b show that single-phase Cu_2O is achieved in all the films with growth predominantly in the [111] direction. Transmission measurements show high transmittance without significant deviations from the un-doped film. The same is observed in a Tauc analysis to investigate the trend in the optical bandgap, and all films show similar E_g of $\simeq 2.55 \pm 0.02$ eV.

4.2.3 Electrical properties $Cu_2O : Li$ films

Carrier density, mobility, and resistivity are plotted vs. Li concentrations in Fig. 4.9. While structural and optical properties were seemingly unchanged within the selected films, doping had a large effect on the electrical properties. The films show an increase in carrier concentration from $\simeq 10^{15} cm^{-3}$ to over $10^{17} cm^{-3}$ at the highest doping level.

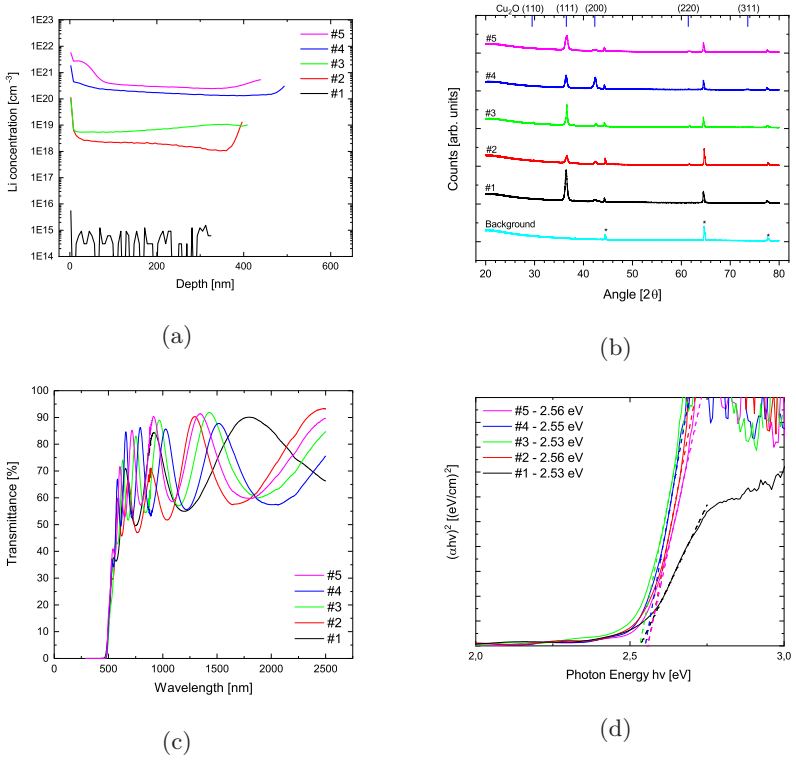

Figure 4.8: Characterization of the Cu_2O (#1) and Cu_2O:Li films **a)** SIMS depth profiles of the films with Li concentrations vs. depth. **b)** $\theta - 2\theta$ XRD pattern of the doped films. Peaks with asterisk marks stem from the background. **c)** Transmittance spectra of the films **d)** Tauc plot of the films deduced from the transmittance spectra in Fig. 4.8c. The optical band gap is extracted by extrapolating to the abscissa. The figures are reprinted from paper II

TDH and TAS measurements were performed, and the analysis can be seen in full in paper III. From temperature-dependent Hall effect measurements (Fig. 4.10), we can see that the hole concentration strongly depends on temperature in all samples. One can observe that p(T), especially samples #1, #4, and #5 in Fig. 4.10, deviates from the simple exponential dependence in Eq. 3.13. In the experimental results, the slope of p(T) increases with increasing T. We interpret this as indicating several acceptor levels in the film, where deeper acceptors become activated at higher temperatures. Nevertheless, in the analysis, we have estimated the activation energy of the most shallow acceptor by fitting Eq. (1) in the lower temperature range (<

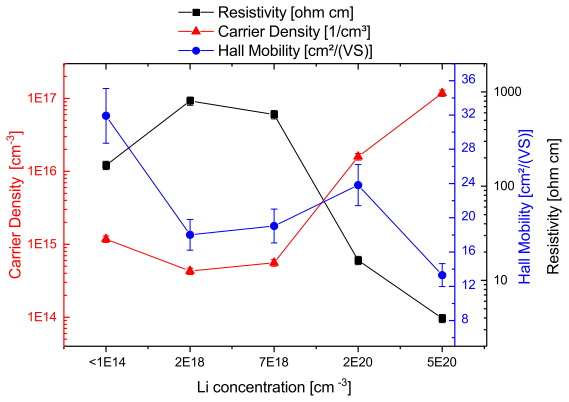

Figure 4.9: Carrier density, mobility, and resistivity from Hall effect measurements plotted versus lithium concentration.

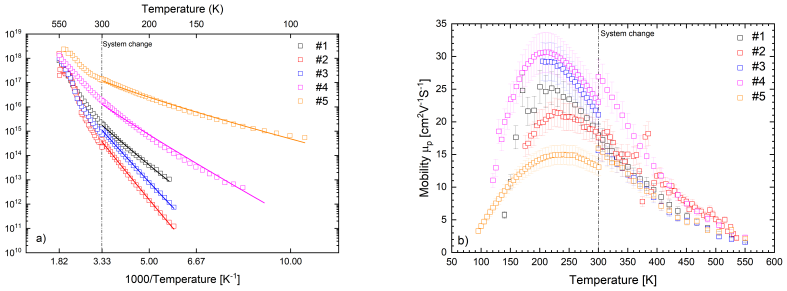

(a) (b)

Figure 4.10: a) TDH results from the Li doped samples with hole concentration plotted versus inverse temperature. b) Carrier mobility plotted versus temperature in the Li doped Cu_2O samples.

300 K) to elucidate the ionization energy of the emerging acceptor. The estimated activation energy is $\sim$ 0.16 eV, 0.25 eV, 0.22 eV, 0.12 eV and 0.05 eV in sample #1-5 respectively. The temperature-dependent mobility data in Fig. 4.10b show a typical bell-shaped temperature dependency. This is generally attributed to the contribution of ionized impurity scattering at low temperatures and intrinsic scattering at elevated temperatures (i.e., phonon scattering). The mobility is relatively low compared to that reported for single crystal samples (80-100 $Cm^2V^{-1}s^{-1}$). This could be attributed to an increased neutral impurity scattering and grain boundary scattering in the polycrystalline thin films.

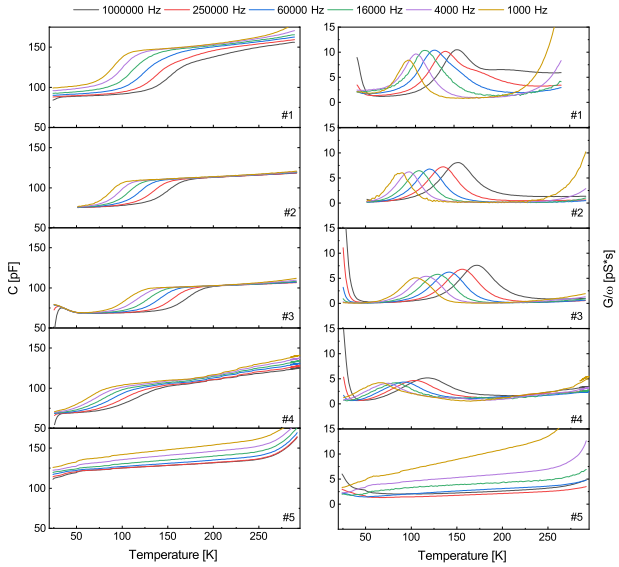

Figure 4.11: a) Conductance/ω plotted versus temperature for the frequencies probed. b) Capacitance plotted versus temperature for the frequencies probed.

TAS measurements are presented in Fig. 4.11. The activation energy of the acceptors can be deduced by performing capacitance and conductance measurements at different probing frequencies. The temperature of the step-like capacitance drop or the conductance maximum varies with frequency[112]. From the TAS plots (Fig. 4.11), a single dominating carrier freeze-out is observed in samples #1 - #4. By performing a standard Arrhenius analysis (see paper III), the deduced energy levels are 0.11 eV, 0.11 eV, 0.14 eV and 0.08 eV for sample #1, #2, #3 and #4, respectively. In sample #5, no clear freeze-out is visible within the investigated temperature range in TAS. The activation energy for the shallow acceptor deduced from TDH measurements was found to be 0.05 eV. This would indicate that the freez- out temperature is outside the probed range.

To substantiate the TAS results, simulations in Silvaco TCAD were performed on the Cu_2O/Si structure (Fig. 4.12). The device structure and parameters were chosen to corroborate with the experimental data of sample # 3 to represent the intermediate case. A diode structure with a 100 μm thick Si substrate was defined together with a 500 nm thick Cu_2O layer. Further, it was defined with an n-type doping concentration of $10^{15} cm^{-3}$ in the Si layer and an acceptor concentration of $1 \times 10^{18} cm^{-3}$ with an activation energy of 0.14 eV in the Cu_2O layer. The simulation code, diode structure, and utilized models are described in Appendix A.

Since the concentration of acceptors in Cu_2O ($10^{18} cm^{-3}$) is much higher

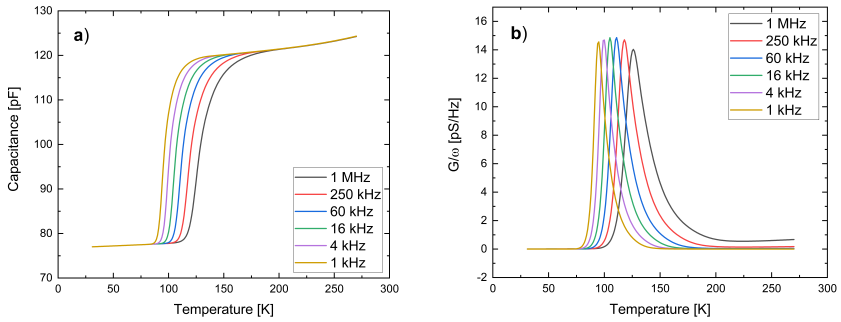

(a) (b)

Figure 4.12: Capacitance (a) and conductance over angular frequency (b) simulated as functions of temperature for the 6 probing frequencies used in the experiment (1 kHz–1MHz).

then the donor concentration in Si ($10^{15}cm^{-3}$), the depletion region is predominantly extended into the Si. This is in agreement with the theory of depletion region in p-n junctions. Thus, the resulting capacitance of the structure is determined mainly by the depletion region in Si, which is around $\sim$ 120 pF for the diode size utilized. When the temperature decreases, a decrease in the capacitance is observed due to the freeze-out of acceptors in Cu_2O. When the Cu_2O films are fully frozen out, it becomes a fully depleted dielectric while the Si still has an ionized donor concentration of $\sim 10^{15}cm^{-3}$ in the investigated temperature range. The capacitance of the structure is then determined mainly by the capacitance of the depleted film, which is about $\sim 80pF$ for the film thickness and diode size utilized. Therefore, the simulation supports that the capacitance step from the experimental data (Fig. 4.11) can be attributed to the freeze-out of the dominant acceptors in the Cu_2O film.

One can see that the activation energies deduced by TAS are systematically lower compared to those deduced by TDH. The reason can be twofold: (1) One can observe that p(T) deviates from perfect exponential dependence in Fig. 4.10, which introduces uncertainty in the activation energy deduced from the TDH measurements. (2) The Poole-Frenkel effect, which lowers the activation energy in external electric fields, can play an important role in the TAS measurements.[120] In the following, an analysis of fitting two acceptors to the TDH data is attempted to achieve a coherent analysis between the TAS and TDH data. In Fig. 4.13a and Fig. 4.13b, the data of sample #4 is fitted to two acceptors (eq. 3.14) without and with a compensating donor, respectively. The resulting activation energy for the shallow acceptor, E_a1, is 0.19 eV and 0.09 eV for the fit without and with compensation, respectively. By considering the TAS measurements, a consistent model could be put

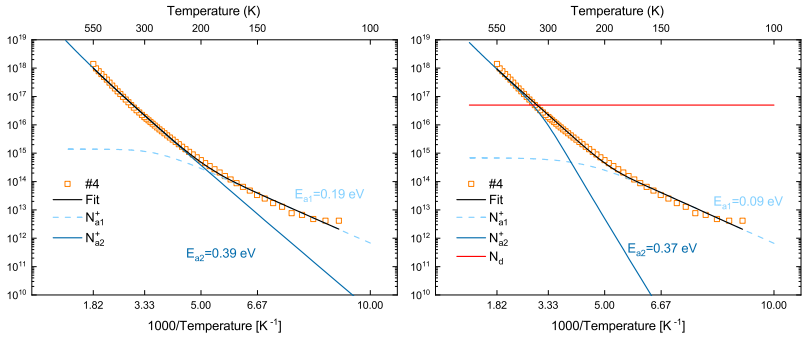

(a) (b)

Figure 4.13: a) TDH results of sample #4 fitted with two acceptors. The fitted curves are plotted together with the temperature-dependent evolution of N_{a1}^{+} and N_{a2}^{+}. b) TDH results of sample #4 fitted with two acceptors and a net compensating donor N_d.

forward where a compensating donor is present in addition to at least two contributing acceptors ($\sim E_V + 0.4$ eV and $\sim E_V + 0.09$ eV), where the shallow level corroborates well with the level at 0.08 eV deduced from TAS.

The behavior with Li doping concentration observed in these samples is similar to that of reports on Na doping, where the acceptor energy deduced from TDH measurements decreases with doping. [55] These results could be said to contradict the predictions by Isseroff et *al.*, where Li was predicted to passivate copper vacancies in Cu_2O [52]. However, the behavior of sample # 2 and # 3 could indicate that passivation of defects in the samples occur to some extent, while other unknown defect configurations dominate at higher concentrations, resulting in the formation of shallow acceptor states in highly Li doped Cu_2O. Finally, the deduced acceptor ionization energies in doped Cu_2O should be done thoroughly due to the presence of additional acceptors and compensating donors, which would warrant more elaborate models to fully explain the temperature-dependent carrier data compared to only a single compensated acceptor.

4.3 The effect of known deep acceptors on the performance of Cu_2O solar cells

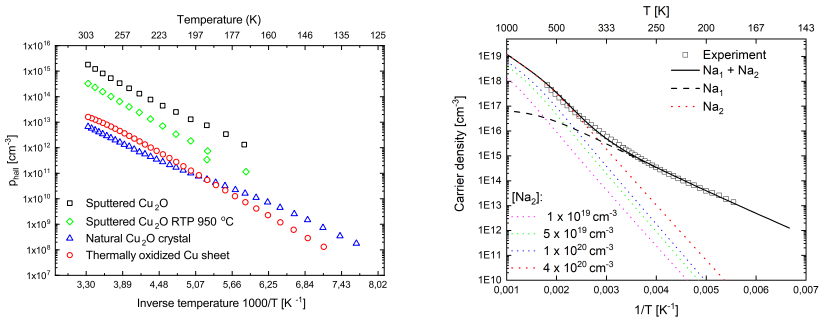

(a) (b)

Figure 4.14: a) Hole concentration plotted versus the inverse temperature for different bulk and sputtered thin-film Cu_2O samples up to 300 K. b) Temperature dependency of carrier concentration in a 500 nm thick sputtered Cu_2O film up to 550K. The data were fitted to two acceptor levels at 0.16 and 0.46 eV above the valence band. The acceptor concentrations deduced from the fit were $1.4 \times 10^{17} cm^{-3}$ and $4 \times 10^{20} cm^{-3}$, respectively, with a compensating donor concentration Nd = $1.3 \times 10^{17} cm^{-3}$

In paper IV, the effect of deep acceptors in the Cu_2O layer of an AZO/Ga_2O_3/Cu_2O/Cu_2O-p^+ cell is studied. The TDH data of different bulk and sputtered thin-film Cu_2O samples are shown in Figure 4.14a. The activation energy in the vicinity of $\sim 0.2eV$ can be deduced for all the samples. This is generally linked to the copper vacancy in Cu_2O with a transition level at $\sim 0.25eV$ above the valence band. In addition to these levels, a deeper level at $\sim 0.4eV$ is routinely reported in Cu_2O, assigned the copper split vacancy. The plots in Figure 4.14 are used to demonstrate the high acceptor concentrations in sputtered thin-film Cu_2O compared to bulk and oxidized copper sheets. Additionally, note the high concentration of the "deep" acceptor in Fig. 4.14b. It is found to be present in concentrations above $10^{20} cm^{-3}$ in the investigated sample. In Paper IV and the following section, the effect of these acceptor levels is investigated to elucidate the effect on bulk recombination in the Cu_2O layer of the solar cells. As Simmons *et al.* put it [121]; "...any trap between the quasi Fermi levels for the trapped electrons and holes is a recombination center", which will lead to poor carrier collection in the cells.

The investigated cell structure was adopted from the current best performing thin-film Cu_2O cell achieved by Lee et al. [64]. This structure

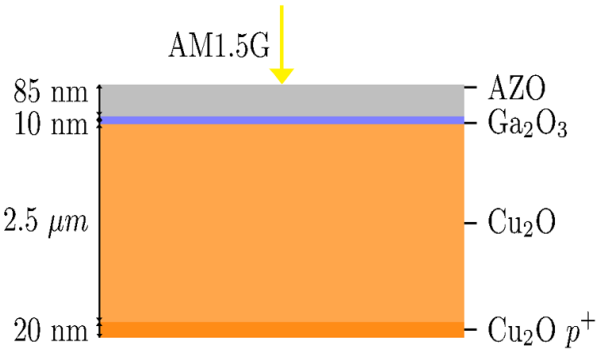

Figure 4.15: Schematic representation of the simulated AZO/Ga_2O_3/Cu_2O/Cu_2O-p^+ heterojunction solar cell.

is also in good agreement with the optimal layer thicknesses found for a Cu_2O-based silicon tandem cell as calculated by Nordseth et al. [107] In their optical model, they predict that a Cu_2O absorber thickness of $\sim 2\mu m$ would yield high absorption and transmittance for the top layer. Additionally, an AZO layer thickness of approximately 80 nm was demonstrated to give the lowest reflectance and highest transmittance for the ZnO/Cu2O subcell. The chosen layer thicknesses and material properties used in the calculations are included in Table 4.3; a schematic model of the cell structure is shown in Fig. 4.15. Further, it was assumed an ideal case with only fundamental loss mechanisms through Shockley-Read-Hall recombination, Auger recombination, and radiative recombination. Details on the included models and the source code used in the simulations are included in Appendix B.

Table 4.3: Simulation parameters for the AZO/Ga_2O_3/Cu_2O solar cell.[19, 41, 42, 49, 72, 105, 122, 123, 124]

Parameters	AZO	Ga_2O_3	Cu_2O	Cu_2O p^+
Thickness (μm)	0.085	0.01	2.4	0.1
Dielectric constant	9	10	7.6	7.6
Bandgap (eV)	3.35	4.8	2.17	2.17
Electron affinity (eV)	4.4	4	3.2	3.2
Effective density of states of conduction band minimum (cm^{-3})	2.2×10^{18}	3.72×10^{18}	2.43×10^{19}	2.43×10^{19}
Effective denstity of states of valence band maximum (cm^{-3})	1.8×10^{19}	3.72×10^{18}	1.34×10^{19}	1.34×10^{19}
Electron mobility [$cm^2/(Vs)$]	10	118	200	200
Hole mobility [$cm^2/(Vs)$]	5	50	100	100
Donor concentration (cm^{-3})	1×10^{20}	1×10^{18}	0	0
Acceptor concentration (cm^{-3})	0	0	1×10^{16}	1×10^{19}
Traps				
Trap distribution			uniform	
Trap density			Variable ($0 - 10^{20}$)	
Trap level (eV)			0.4	
Capture cross section of electrons (cm^2)			1×10^{-15}	
Capture cross section of holes (cm^2)			1×10^{-15}	

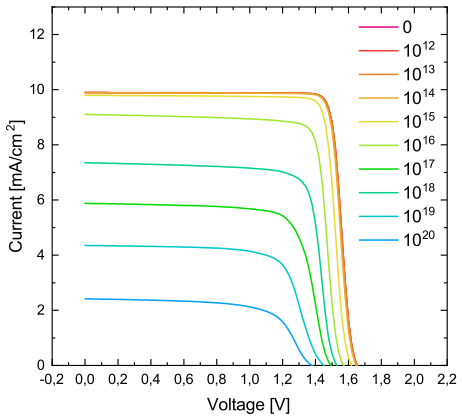

Figure 4.16: IV curves of the simulated AZO/Ga_2O_3/Cu_2O cells with increasing deep acceptor concentrations.

The simulated IV curves in Fig. 4.16 show that the increased deep acceptor densities lead to an evident deficiency in cell performance. In the ideal case, with a low concentration, a cell efficiency of 15 % is achieved, with an open-circuit voltage of V_{OC} = 1.67 V, current density J_{SC} = 11 mA, and fill factor FF = 80%. This is in good agreement with Takiguchi and Miyajima [105], which found that efficiencies up to $\sim$ 16 % were achievable from simulations of an optimized Cu_2O thin-film structure. In Fig. 4.16, one can clearly see the effect of increased deep acceptor concentrations. SRH recombination becomes significant at concentrations above $10^{15} cm^{-3}$, resulting in a dropping current density accompanied by a correlated smaller drop in V_{OC} and FF with increasing acceptor concentrations. In the cell with a similar concentration of the deep acceptor as in our sputtered samples (10^{20} cm^{-3}) the cell efficiency is below 3%, with a low current density of 2-3 mA. Sputtered thin-film devices have yet to surpass efficiencies of 1-2 %. These simulations show clearly that the high defect concentration in sputtered Cu_2O contributes factor to the limited efficiencies achieved in these devices. To achieve better performing Cu_2O thin-film solar cells, proper identification and passivization of the deep acceptor states in Cu_2O to below $10^{15} cm^{-3}$ would be required to limit losses from SRH recombination.

The EQE data from Lee et *al.* [64], which demonstrated excellent interface quality through atomic layer deposition of Ga_2O_3 buffer layer in an AZO/Ga_2O_3/Cu_2O cell, is included in Fig. 4.17. The cell demonstrated the highest V_{OC} reported in any Cu_2O-based solar cell of 1.2 V, just above that achieved in bulk devices (1.1 eV)[14]. The EQE curve shows similar characteristics for the high wavelengths as the simulation results, which

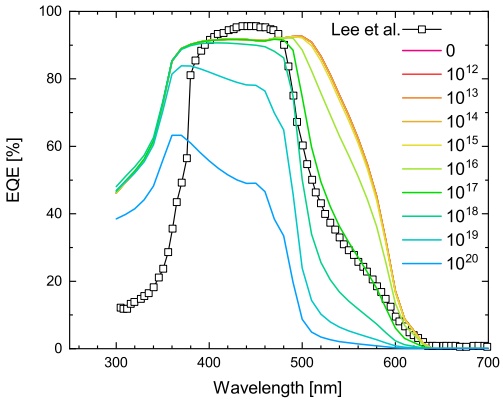

Figure 4.17: EQE of the simulated devices with increasing deep acceptor concentrations. The data labeled Lee et al. is experimental EQE data digitized from Lee et *al.* [64]

could imply recombination within the Cu_2O layer due to SRH recombination. Further, the experimental data are analogous to the simulated data with a deep acceptor concentration of $\sim 10^{17} cm^{-3}$, which is in line with the result of other post-deposition treated thin films[37, 42]. From these simulations, one could suggest that higher efficiencies are possible if one could limit the concentration of deep acceptors ($< 10^{15} cm^{-3}$) in bulk and thin-film Cu_2O.

Chapter 5

Conclusions and Future Work

Properties of both bulk and thin films have been investigated to assess its viability for use in solar cells.

Dominating acceptors and electrical transport properties were investigated in a naturally formed single crystal Cu_2O sample. The study deduced four different electronic levels around 0.16 eV, 0.22 eV, 0.4 eV above the valence band, and a cathodoluminescence deep emission line at 1.3 eV. The levels at 0.16 eV and 0.22 eV were assigned to a nitrogen-related center and to the widely reported copper vacancy, V_{Cu}. Furthermore, based on theoretical predictions and recent literature, we question the generally accepted assignment of the deep emission levels seen in cathodoluminescence at 1.7 eV and 1.3 eV to the oxygen vacancy and copper vacancy, respectively. We discuss that the emission band at $\sim$ 1.7 eV could be attributed to the the copper split vacancy,V_{Cu}^{split}, widely reported as an acceptor in Cu_2O located at $\sim$ 0.4 eV above the valence band. Finally, the widely reported photoluminescence peak at $\sim$ 1.3 eV is speculated to be a hydrogen-V_{Cu} related center due to the high level of residual H content and theoretical calculation of hydrogen-related defects. Additionally, we demonstrate that the limiting mechanism of carrier mobility can be attributed to scattering on neutral and ionized defect centers.

Li doping of Cu_2O was studied in sputtered thin films. Cu_2O:Li films with Li concentrations of $2 \times 10^{18} - 10^{20} cm^{-3}$ are shown to retain pure phase, relatively high mobility, and transparency in the investigated samples. The isovalent Li dopant was proposed to reduce acceptor concentration by passivating V_{Cu}. However, an increased carrier density with increased Li doping concentrations is reported. The highest doped sample exhibits a high carrier concentration at room temperature ($1.2 \times 10^{17} cm^{-3}$ at 300 K). Further, the highly doped films exhibited a reduction in ionization energy from $\sim$ 0.16 eV to $\sim$ 0.08 and 0.05 eV above the valence band for samples with Li concentrations of $2 \times 10^{20} cm^{-3}$ and $5 \times 10^{20} cm^{-3}$, respectively. The doping characteristics are deemed similar to the reports on Na doping in Cu_2O.

Through SILVACO simulation, it is revealed that Shockley-Reed-Hall recombination could be majorly contributing to limiting the efficiency in thin-film Cu_2O devices due to the high presence of deep-level acceptors. The results could also explain the large gap in device performance between bulk and thin-film devices. Bulk crystals are reported from DLTS studies with as low concentrations as $\sim 1 \times 10^{11} cm^{-3}$ of the deep acceptor compared

to $\sim 1 \times 10^{16-20} cm^{-3}$ in thin films. It is demonstrated for sputtered films, which are found to have high concentrations of deep acceptors, $> 10^{20} cm^{-3}$, that high recombination and poor carrier collection impede cell performance, resulting in efficiencies below 3%.

The conversion efficiency of Cu_2O-based solar cells has not improved since the advances made by Minami *et al.* in 2016, and thin-film technologies have yet to surpass $\sim 4\%$ efficiency. Many of the incremental improvements have been due to interface and junction engineering. While further progress can be made in this regard, a better understanding and control of defects in Cu_2O is important. Studies on unintentional impurities in Cu_2O could help identify the different acceptor states in Cu_2O. Especially systematic studies elucidating hydrogen and nitrogen's role could help identify the ambiguous defect behavior observed. It would be advisable to utilize high-quality single crystals to reduce the noise of other defects present in thin films at presumably high concentrations, making the effect of H in Cu_2O challenging to discern.

Thin-film Cu_2O would benefit from lowering the deep acceptor concentrations and would be required in order to achieve performances matching that of bulk Cu_2O devices. The author sincerely hopes the considerations and observations presented in this thesis can stimulate further discussions on the path toward realizing sustainable, high-performing Cu_2O solar cells.

Bibliography

[1] W. H. Brattain. "The Copper Oxide Rectifier". In: *Rev. Mod. Phys.* vol. 23 (3 1951), pp. 203–212. DOI: 10.1103/RevModPhys.23.203.

[2] J. Tudor. "A brief history of semiconductors". In: *Physics Education* vol. 40, no. 5 (2005), pp. 430–439. DOI: 10.1088/0031-9120/40/5/002.

[3] H. Ritchie and M. Roser. "Energy". In: *Our World in Data* (2020).

[4] *World Energy Outlook 2020*. Tech. rep. Paris: IEA, 2020.

[5] NREL. *Best Research-Cell Efficiency Chart*. https://www.nrel.gov/pv/cell-efficiency.html. 2021.

[6] Fraunhofer ISE. *Photovltaics Report 2020*. http://bit.ly/S8YtWS. July 2021.

[7] S. Essig et al. "Raising the one-sun conversion efficiency of III–V/Si solar cells to 32.8% for two junctions and 35.9% for three junctions". In: *Nature Energy* vol. 2, no. 9 (2017), p. 17144. DOI: 10.1038/nenergy.2017.144.

[8] C. Wadia, A. P. Alivisatos, and D. M. Kammen. "Materials Availability Expands the Opportunity for Large-Scale Photovoltaics Deployment". In: *Environmental Science & Technology* vol. 43, no. 6 (2009), pp. 2072–2077. DOI: 10.1021/es8019534.

[9] M. Green et al. "Solar cell efficiency tables (version 57)". In: *Progress in Photovoltaics: Research and Applications* vol. 29, no. 1 (2021), pp. 3–15. DOI: https://doi.org/10.1002/pip.3371.

[10] J. Jeong et al. "Pseudo-halide anion engineering for α-FAPbI3 perovskite solar cells". In: *Nature* vol. 592, no. 7854 (2021), pp. 381–385. DOI: 10.1038/s41586-021-03406-5.

[11] C. Kamaraki et al. "Perovskite/silicon tandem photovoltaics: Technological disruption without business disruption". In: *Applied Physics Letters* vol. 119, no. 7 (2021), p. 070501. DOI: 10.1063/5.0054086.

[12] F. C. Krebs, ed. John Wiley & Sons, Ltd, 2012, pp. i–xvi. DOI: https://doi.org/10.1002/9781119942436.fmatter.

[13] Q. Liu et al. "18% Efficiency organic solar cells". In: *Science Bulletin* vol. 65, no. 4 (2020), pp. 272–275. DOI: https://doi.org/10.1016/j.scib.2020.01.001.

[14] T. Minami, Y. Nishi, and T. Miyata. "Efficiency enhancement using a Zn_{1-x} Ge_x-O thin film as an n-type window layer in Cu_2O-based heterojunction solar cells". In: *Applied Physics Express* vol. 9, no. 5 (2016), p. 052301. DOI: 10.7567/APEX.9.052301.

[15] A. De Vos. "Detailed balance limit of the efficiency of tandem solar cells". In: *Journal of Physics D: Applied Physics* vol. 13, no. 5 (1980), p. 839. DOI: 10.1088/0022-3727/13/5/018.

[16] T. P. White, N. N. Lal, and K. R. Catchpole. "Tandem Solar Cells Based on High-Efficiency c-Si Bottom Cells: Top Cell Requirements for >30% Efficiency". In: *IEEE Journal of Photovoltaics* vol. 4, no. 1 (2014), pp. 208–214. DOI: 10.1109/JPHOTOV.2013.2283342.

[17] M. R. Mitroi, V. Ninulescu, and L. Fara. "Tandem Solar Cells Based on Cu_2O and c-Si Subcells in Parallel Configuration: Numerical Simulation". In: *International Journal of Photoenergy* vol. 2017 (2017), p. 6. DOI: 10.1155/2017/7284367.

[18] R. E. Brandt et al. "Identifying and comparing efficiency-loss mechanisms in earth-abundant thin-film solar cells". In: *2013 IEEE 39th Photovoltaic Specialists Conference (PVSC)*. 2013, pp. 0846–0848. DOI: 10.1109/PVSC.2013.6744277.

[19] B. K. Meyer et al. "The Physics of Copper Oxide Cu_2O". In: *Semiconductors and Semimetals*. Ed. by B. G. Svensson, S. J. Pearton, and C. Jagadish. Vol. 88. Academic Press, 2013, pp. 201–226. DOI: 10.1016/B978-0-12-396489-2.00006-0.

[20] T. Leijtens et al. "Opportunities and challenges for tandem solar cells using metal halide perovskite semiconductors". In: *Nature Energy* vol. 3, no. 10 (2018), pp. 828–838. DOI: 10.1038/s41560-018-0190-4.

[21] H. A. Al-Jawhari. "A review of recent advances in transparent p-type Cu_2O-based thin film transistors". In: *Materials Science in Semiconductor Processing* vol. 40 (2015), pp. 241–252. DOI: https://doi.org/10.1016/j.mssp.2015.06.063.

[22] Y.-H. Zhang et al. "Recent advances in Cu_2O-based composites for photocatalysis: a review". In: *Dalton Transactions* vol. 50, no. 12 (2021), pp. 4091–4111. DOI: 10.1039/D0DT04434B.

[23] R. Wick and S. D. Tilley. "Photovoltaic and Photoelectrochemical Solar Energy Conversion with Cu_2O". In: *The Journal of Physical Chemistry C* vol. 119, no. 47 (2015), pp. 26243–26257. DOI: 10.1021/acs.jpcc.5b08397.

[24] S. Sun et al. “Cuprous oxide (Cu_2O) crystals with tailored architectures: A comprehensive review on synthesis, fundamental properties, functional modifications and applications”. In: *Progress in Materials Science* vol. 96 (2018), pp. 111–173. DOI: https://doi.org/10.1016/j.pmatsci.2018.03.006.

[25] Francesco Biccari. “Defects and doping in Cu_2O”. PhD thesis. University of Rome, 2009.

[26] T. Minami et al. “High-Efficiency Oxide Solar Cells with ZnO/Cu_2O Heterojunction Fabricated on Thermally Oxidized Cu_2O Sheets”. In: *Applied Physics Express* vol. 4, no. 6 (2011), p. 062301. DOI: 10.1143/apex.4.062301.

[27] P. Villars and K. Cenzual, eds. *Cu2O Crystal Structure: Datasheet from “PAULING FILE Multinaries Edition – 2012” in SpringerMaterials.* accessed 2021-05-11.

[28] P. A. Korzhavyi and B. Johansson. *Literature review on the properties of cuprous oxide Cu_2O and the process of copper oxidation.* Tech. rep. October. Stockholm: Royal Institute of Technology, 2011, pp. 8–22.

[29] T. Ito et al. “Single-crystal growth and characterization of Cu_2O and CuO”. In: *J. Mater. Sci.* vol. 33 (1998), p. 3555. DOI: 10.1023/A:1004690809547.

[30] T. G. Kim, H. Ryu, and W.-J. Lee. “Effects of lithium (Li) on lithium-cuprous-oxide (Li-Cu_2O) composite films grown by using electrochemical deposition for a PEC photoelectrode”. eng. In: *Journal of the Korean Physical Society* vol. 68, no. 2 (2016), pp. 268–273. DOI: 10.3938/jkps.68.268.

[31] D. S. Darvish and H. A. Atwater. “Epitaxial growth of Cu_2O and ZnO/Cu_2O thin films on MgO by plasma-assisted molecular beam epitaxy”. eng. In: *Journal of crystal growth* vol. 319, no. 1 (2011), pp. 39–43. DOI: 10.1016/j.jcrysgro.2011.01.071.

[32] J. R. Avila et al. “Atomic layer deposition of Cu(i) oxide films using Cu(ii) bis(dimethylamino-2-propoxide) and water”. In: *Dalton Trans.* vol. 46 (2017), pp. 5790–5795. DOI: 10.1039/C6DT02572B.

[33] J. Gan et al. “Influence of target power on properties of Cu_xO thin films prepared by reactive radio frequency magnetron sputtering”. In: *Thin Solid Films* vol. 594 (2015), pp. 250–255. DOI: 10.1016/j.tsf.2015.05.029.

[34] A. Jafari et al. “Ion Implantation of Copper Oxide Thin Films; Statistical and Experimental Results”. In: *Surfaces and Interfaces* vol. 18 (2020), p. 100463. DOI: 10.1016/j.surfin.2020.100463.

[35] J. F. Pierson, A. Thobor-Keck, and A. Billard. "Cuprite, paramelaconite and tenorite films deposited by reactive magnetron sputtering". In: *Applied Surface Science* vol. 210, no. 3-4 (2003), pp. 359–367. DOI: 10.1016/S0169-4332(03)00108-9.

[36] B.S. Li, K. Akimoto, and A. Shen. "Growth of Cu_2O thin films with high hole mobility by introducing a low-temperature buffer layer". In: *Journal of Crystal Growth* vol. 311, no. 4 (2009), pp. 1102–1105. DOI: 10.1016/j.jcrysgro.2008.11.038.

[37] K. Bergum et al. "Improving carrier transport in Cu_2O thin films by rapid thermal annealing". In: *Journal of Physics: Condensed Matter* vol. 30, no. 7 (2018), p. 75702. DOI: 10.1088/1361-648x/aaa5f4.

[38] C. Malerba et al. "Absorption coefficient of bulk and thin film Cu_2O". In: *Solar Energy Materials and Solar Cells* vol. 95, no. 10 (2011), pp. 2848–2854. DOI: 10.1016/j.solmat.2011.05.047.

[39] D. O. Scanlon and G. W. Watson. "Uncovering the Complex Behavior of Hydrogen in Cu_2O". In: *Phys. Rev. Lett.* vol. 106 (2011), p. 186403. DOI: 10.1103/PhysRevLett.106.186403.

[40] G. P. Pollack and D. Trivich. "Photoelectric properties of cuprous oxide". In: *Journal of Applied Physics* vol. 46, no. 1 (1975), pp. 163–172. DOI: 10.1063/1.321312.

[41] L. Papadimitriou. "DLTS evaluation of nonexponential transients of defect levels in cuprous oxide (Cu_2O)". In: *Solid-State Electronics* vol. 36, no. 3 (1993), pp. 431–434. DOI: 10.1016/0038-1101(93)90098-B.

[42] G. K. Paul et al. "Defects in Cu_2O studied by deep level transient spectroscopy". In: *Applied Physics Letters* vol. 88, no. 14 (2006). DOI: 10.1063/1.2175492.

[43] M. Nyborg et al. "Deposition and characterization of lithium doped direct current magnetron sputtered Cu_2O films". In: *Thin Solid Films* vol. 722 (2021), p. 138573. DOI: 10.1016/j.tsf.2021.138573.

[44] M. Nyborg et al. "Dominant acceptors in Li doped, magnetron deposited Cu_2O films". In: *Materials Research Express* vol. 8, no. 12 (2021), p. 125903.

[45] M. Nyborg et al. "Dominant defects and carrier transport in single crystalline cuprous oxide: A new attribution of optical transitions". In: *Journal of Applied Physics* vol. 130, no. 17 (2021), p. 175701. DOI: 10.1063/5.0059406.

[46] J. Xue and R. Dieckmann. "The non-stoichiometry and the point defect structure of cuprous oxide ($Cu_{2-\delta}O$)". In: *Journal of Physics and Chemistry of Solids* vol. 51, no. 11 (1990), pp. 1263–1275. DOI: 10.1016/0022-3697(90)90003-X.

[47] O. Porat and I. Riess. "Defect chemistry of $Cu_{2-y}O$ at elevated temperatures. Part II: Electrical conductivity, thermoelectric power and charged point defects". In: *Solid State Ionics* vol. 81, no. 1 (1995), pp. 29–41. DOI: 10.1016/0167-2738(95)00169-7.

[48] M. Nolan and S. D. Elliott. "The p-type conduction mechanism in Cu_2O: a first principles study". In: *Physical Chemistry Chemical Physics* vol. 8, no. 45 (2006), pp. 5350–5358. DOI: 10.1039/B611969G.

[49] D. O. Scanlon et al. "Acceptor levels in p-type Cu_2O: Rationalizing theory and Experiment". In: *Physical Review Letters* vol. 103, no. 9 (2009), pp. 1–4. DOI: 10.1103/PhysRevLett.103.096405.

[50] H. Raebiger, S. Lany, and A. Zunger. "Origins of the p-type nature and cation deficiency in Cu_2O and related materials". In: *Physical Review B* vol. 76, no. 4 (2007), p. 45209. DOI: 10.1103/PhysRevB.76.045209.

[51] A. F. Wright and J. S. Nelson. "Theory of the copper vacancy in cuprous oxide". In: *Journal of Applied Physics* vol. 92, no. 10 (2002), pp. 5849–5851. DOI: 10.1063/1.1516620.

[52] L. Y. Isseroff and E. A. Carter. "Electronic structure of pure and doped cuprous oxide with copper vacancies: Suppression of trap states". In: *Chemistry of Materials* vol. 25, no. 3 (2013), pp. 253–265. DOI: 10.1021/cm3040278.

[53] J. Li et al. "Probing Defects in Nitrogen-Doped Cu_2O". In: *Scientific Reports* vol. 4 (2014). DOI: 10.1038/srep07240.

[54] J. Thienprasert and S. Limpijumnong. "Identification of nitrogen acceptor in Cu_2O: First-principles study". In: *Applied Physics Letters* vol. 107, no. 22 (2015), p. 221905. DOI: 10.1063/1.4936760.

[55] T. Minami, Y. Nishi, and T. Miyata. "Impact of incorporating sodium into polycrystalline p-type Cu_2O for heterojunction solar cell applications". In: *Applied Physics Letters* vol. 105, no. 21 (2014), p. 212104. DOI: 10.1063/1.4902879.

[56] S. Brochen et al. "Effect of Strontium Incorporation on the p-Type Conductivity of Cu_2O Thin Films Deposited by Metal–Organic Chemical Vapor Deposition". In: *The Journal of Physical Chemistry C* vol. 120, no. 31 (2016), pp. 17261–17267. DOI: 10.1021/acs.jpcc.6b05479.

[57] N. Tabuchi and H. Matsumura. "Control of Carrier Concentration in Thin Cuprous Oxide Cu_2O Films by Atomic Hydrogen". In: *Japanese Journal of Applied Physics* vol. 41, no. Part 1, No. 8 (2002), pp. 5060–5063. DOI: 10.1143/jjap.41.5060.

[58] R. Kumar et al. “Impact of post annealing and hydrogen implantation on functional properties of Cu_2O thin films for photovoltaic applications”. In: *Journal of Alloys and Compounds* vol. 825 (2020), p. 153982. DOI: https://doi.org/10.1016/j.jallcom.2020.153982.

[59] K. P. Hering et al. “Hydrogen induced mobility enhancement in RF sputtered Cu2O thin films”. In: *Journal of Applied Physics* vol. 120, no. 18 (2016), p. 185705. DOI: 10.1063/1.4966605.

[60] S. Pelegrini et al. “Electrochemical Cl Doping of Cu_2O: Structural and Morphological Properties”. In: *ECS Journal of Solid State Science and Technology* vol. 4, no. 7 (2015), pp. 181–185. DOI: 10.1149/2.0041507jss.

[61] S. Pelegrini et al. “Electrodeposited Cu_2O doped with Cl: Electrical and optical properties”. In: *Journal of Applied Physics* vol. 123, no. 16 (2018), p. 161567. DOI: 10.1063/1.5004782.

[62] M. D. McCluskey and S. J. Jokela. “Defects in ZnO”. In: *Journal of Applied Physics* vol. 106, no. 7 (2009), p. 071101. DOI: 10.1063/1.3216464.

[63] K. S. Cho et al. “Li-doped Cu_2O/ZnO heterojunction for flexible and semi-transparent piezoelectric nanogenerators”. In: *Ceramics International* vol. 43, no. 2 (2017), pp. 2279–2287. DOI: 10.1016/j.ceramint.2016.10.208.

[64] Y. S. Lee et al. “Atomic Layer Deposited Gallium Oxide Buffer Layer Enables 1.2 V Open-Circuit Voltage in Cuprous Oxide Solar Cells”. In: *Advanced Materials* vol. 26, no. 27 (2014), pp. 4704–4710. DOI: 10.1002/adma.201401054.

[65] H. K. Nguyen et al. “The characteristics of IGZO/ZnO/Cu_2O:Na thin film solar cells fabricated by DC magnetron sputtering method”. In: *Journal of Photochemistry and Photobiology A: Chemistry* vol. 349 (2017), pp. 100–107. DOI: https://doi.org/10.1016/j.jphotochem.2017.09.016.

[66] J. Benz et al. “The influence of nitrogen doping on the electrical and vibrational properties of Cu_2O”. In: *physica status solidi (b)* vol. 254, no. 4 (2017), p. 1600421. DOI: 10.1002/pssb.201600421.

[67] S. Ishizuka et al. “Nitrogen Doping into Cu_2O Thin Films Deposited by Reactive Radio-Frequency Magnetron Sputtering”. In: *Japanese Journal of Applied Physics* vol. 40, no. Part 1, No. 4B (2001), pp. 2765–2768. DOI: 10.1143/jjap.40.2765.

[68] C. Malerba et al. “Nitrogen doped Cu_2O: A possible material for intermediate band solar cells?” In: *Solar Energy Materials and Solar Cells* vol. 105 (2012), pp. 192–195. DOI: 10.1016/j.solmat.2012.06.017.

[69] Y. Wang et al. “Nitrogen chemical state in N-doped Cu_2O thin films”. In: *Applied Physics Letters* vol. 110, no. 13 (2017), p. 131902. DOI: 10.1063/1.4979140.

[70] Y. Wang and J. F. Pierson. “Binary copper oxides as photovoltaic absorbers: recent progress in materials and applications”. In: *Journal of Physics D: Applied Physics* vol. 54, no. 26 (2021), p. 263002. DOI: 10.1088/1361-6463/abf165.

[71] C. G. Van de Walle and J. Neugebauer. “Universal alignment of hydrogen levels in semiconductors, insulators and solutions”. In: *Nature* vol. 423, no. 6940 (2003), pp. 626–628. DOI: 10.1038/nature01665.

[72] B. K. Meyer et al. “Binary copper oxide semiconductors: From materials towards devices”. In: *Physica Status Solidi B* vol. 249, no. 8 (2012), pp. 1487–1509. DOI: 10.1002/pssb.201248128.

[73] W. Siripala et al. “Study of annealing effects of cuprous oxide grown by electrodeposition technique”. In: *Solar Energy Materials and Solar Cells* vol. 44, no. 3 (1996), pp. 251–260. DOI: https://doi.org/10.1016/0927-0248(96)00043-8.

[74] C. A. N. Fernando and S. K. Wetthasinghe. “Investigation of photoelectrochemical characteristics of n-type Cu_2O films”. In: *Solar Energy Materials and Solar Cells* vol. 63, no. 3 (2000), pp. 299–308. DOI: 10.1016/S0927-0248(00)00036-2.

[75] C. Jayewardena et al. “Fabrication of n-Cu_2O electrodes with higher energy conversion efficiency in a photoelectrochemical cell”. In: *Solar Energy Materials and Solar Cells* vol. 56, no. 1 (1998), pp. 29–33. DOI: 10.1016/S0927-0248(98)00104-4.

[76] C. M. McShane and K.-S Choi. “Photocurrent Enhancement of n-Type Cu_2O Electrodes Achieved by Controlling Dendritic Branching Growth”. In: *Journal of the American Chemical Society* vol. 131, no. 7 (2009), pp. 2561–2569. DOI: 10.1021/ja806370s.

[77] K. Han and M. Tao. “Electrochemically deposited p–n homojunction cuprous oxide solar cells”. In: *Solar Energy Materials and Solar Cells* vol. 93, no. 1 (2009), pp. 153–157. DOI: https://doi.org/10.1016/j.solmat.2008.09.023.

[78] H. M. Wei et al. “Photovoltaic Efficiency Enhancement of Cu_2O Solar Cells Achieved by Controlling Homojunction Orientation and Surface Microstructure”. In: *The Journal of Physical Chemistry C* vol. 116, no. 19 (2012), pp. 10510–10515. DOI: 10.1021/jp301904s.

[79] C. M. McShane, W. P. Siripala, and K.-S. Choi. “Effect of Junction Morphology on the Performance of Polycrystalline Cu_2O Homojunction Solar Cells”. In: *The Journal of Physical Chemistry Letters* vol. 1, no. 18 (2010), pp. 2666–2670. DOI: 10.1021/jz100991e.

[80] R. Garuthara and W. Siripala. “Photoluminescence characterization of polycrystalline n-type Cu_2O films”. In: *Journal of Luminescence* vol. 121, no. 1 (2006), pp. 173–178. DOI: 10.1016/j.jlumin.2005.11.010.

[81] W. Wang et al. “pH-dependence of conduction type in cuprous oxide synthesized from solution”. In: *Journal of Applied Physics* vol. 107, no. 12 (2010), p. 123717. DOI: 10.1063/1.3452383.

[82] D. O. Scanlon and G. W. Watson. “Undoped n-Type Cu_2O: Fact or Fiction?” In: *The Journal of Physical Chemistry Letters* vol. 1, no. 17 (2010), pp. 2582–2585. DOI: 10.1021/jz100962n.

[83] J. N. Nian et al. “Elucidating the Conductivity-Type Transition Mechanism of p-Type Cu_2O Films from Electrodeposition”. In: *Journal of The Electrochemical Society* vol. 156, no. 7 (2009), H567. DOI: 10.1149/1.3125800.

[84] H. Shimada and T. Masumi. “Hall Mobility of Positive Holes in Cu_2O”. In: *Journal of the Physical Society of Japan* vol. 58, no. 5 (1989), pp. 1717–1724. DOI: 10.1143/JPSJ.58.1717.

[85] K. Matsuzaki et al. “Epitaxial growth of high mobility Cu_2O thin films and application to p-channel thin film transistor”. In: *Applied Physics Letters* vol. 93, no. 20 (2008), p. 202107. DOI: 10.1063/1.3026539.

[86] Y. Toyozawa and A. Sumi. “Metastable Self-Trapping and Anomalous Temperature Dependence of Hole Mobility BT - Proceedings of the Twelfth International Conference on the Physics of Semiconductors”. In: ed. by Manfred H Pilkuhn. Wiesbaden: Vieweg+Teubner Verlag, 1974, pp. 179–183.

[87] D. Chattopadhyay and H. J. Queisser. “Electron scattering by ionized impurities in semiconductors”. In: *Rev. Mod. Phys.* vol. 53 (1981), pp. 745–768. DOI: 10.1103/RevModPhys.53.745.

[88] Y. S. Lee et al. “Ultrathin amorphous zinc-tin-oxide buffer layer for enhancing heterojunction interface quality in metal-oxide solar cells”. In: *Energy Environ. Sci.* vol. 6 (2013), pp. 2112–2118. DOI: 10.1039/C3EE24461J.

[89] S. S. Li. “Excess Carrier Phenomenon in Semiconductors BT - Semiconductor Physical Electronics”. In: ed. by Sheng S Li. New York, NY: Springer, 2006, pp. 134–170. DOI: 10.1007/0-387-37766-2_6.

[90] W. Shockley and W. T. Read. “Statistics of the Recombinations of Holes and Electrons”. In: *Phys. Rev.* vol. 87 (1952), pp. 835–842. DOI: 10.1103/PhysRev.87.835.

[91] R. N. Hall. “Electron-Hole Recombination in Germanium”. In: *Phys. Rev.* vol. 87 (1952), pp. 387–387. DOI: 10.1103/PhysRev.87.387.

[92] J. Gan et al. “Structural properties of Cu_2O epitaxial films grown on c-axis single crystal ZnO by magnetron sputtering”. In: *Applied Physics Letters* vol. 108, no. 15 (2016), p. 152110. DOI: 10.1063/1.4945985.

[93] S. Siol et al. “Band Alignment Engineering at Cu_2O/ZnO Heterointerfaces”. In: *ACS Applied Materials & Interfaces* vol. 8, no. 33 (2016), pp. 21824–21831. DOI: 10.1021/acsami.6b07325.

[94] W. Shockley and H. J. Queisser. “Detailed Balance Limit of Efficiency of p-n Junction Solar Cells”. In: *Journal of Applied Physics* vol. 32, no. 3 (1961), pp. 510–519. DOI: 10.1063/1.1736034.

[95] T. Minami, Y. Nishi, and T. Miyata. “Heterojunction solar cell with 6% efficiency based on an n-type aluminum–gallium–oxide thin film and p-type sodium-doped Cu_2O sheet”. In: *Applied Physics Express* vol. 8, no. 2 (2015), p. 022301. DOI: 10.7567/apex.8.022301.

[96] Y. Ievskaya et al. “Fabrication of ZnO/Cu_2O heterojunctions in atmospheric conditions: Improved interface quality and solar cell performance”. In: *Solar Energy Materials and Solar Cells* vol. 135 (2015). EMRS 2014 Spring Meeting – Advanced materials and characterization techniques for solar cells II, pp. 43–48. DOI: 10.1016/j.solmat.2014.09.018.

[97] W. Niu et al. “Photoresponse enhancement of Cu_2O solar cell with sulfur-doped ZnO buffer layer to mediate the interfacial band alignment”. In: *Solar Energy Materials and Solar Cells* vol. 144 (2016), pp. 717–723. DOI: 10.1016/j.solmat.2015.10.013.

[98] Y. Nishi, T. Miyata, and T. Minami. “Effect of inserting a thin buffer layer on the efficiency in n-ZnO/p-Cu_2O heterojunction solar cells”. In: *Journal of Vacuum Science & Technology A* vol. 30, no. 4 (2012), p. 04D103. DOI: 10.1116/1.3698596.

[99] T. Minami, Y. Nishi, and T. Miyata. “High-Efficiency Cu_2O-Based Heterojunction Solar Cells Fabricated Using a Ga_2O_3 Thin Film as n-Type Layer”. In: *Applied Physics Express* vol. 6, no. 4 (2013), p. 044101. DOI: 10.7567/apex.6.044101.

[100] Y. S. Lee et al. “Ultrathin amorphous zinc-tin-oxide buffer layer for enhancing heterojunction interface quality in metal-oxide solar cells”. In: *Energy & Environmental Science* vol. 6 (2013), pp. 2112–2118. DOI: 10.1039/C3EE24461J.

[101] Z. Zang. “Efficiency enhancement of ZnO/Cu_2O solar cells with well oriented and micrometer grain sized Cu_2O films”. In: *Applied Physics Letters* vol. 112, no. 4 (2018), p. 042106. DOI: 10.1063/1.5017002.

[102] T. Minami et al. “High-Efficiency Oxide Heterojunction Solar Cells Using Cu_2O Sheets”. In: *Japanese Journal of Applied Physics* vol. 43, no. 7A (2004), pp. 917–919. DOI: 10.1143/jjap.43.l917.

[103] S. S. Wilson et al. “Interface stoichiometry control to improve device voltage and modify band alignment in ZnO/Cu_2O heterojunction solar cells”. In: *Energy & Environmental Science* vol. 7, no. 11 (2014), pp. 3606–3610. DOI: 10.1039/C4EE01956C.

[104] R. E. Brandt et al. “Band offsets of n-type electron-selective contacts on cuprous oxide (Cu_2O) for photovoltaics”. In: *Applied Physics Letters* vol. 105, no. 26 (2014). DOI: 10.1063/1.4905180.

[105] Y. Takiguchi and S. Miyajima. “Device simulation of cuprous oxide heterojunction solar cells”. In: *Japanese Journal of Applied Physics* vol. 54, no. 11 (2015), p. 112303. DOI: 10.7567/JJAP.54.112303.

[106] C. Dumitru et al. “Electrical modeling of the buffer layer for A Cu_2O/ZnO solar cell using atlas”. In: *University Politehnica of Bucharest The Scientific Bulletin Series B* vol. 79 (2017), pp. 3–8.

[107] Ø. Nordseth et al. “Optical Analysis of a ZnO/Cu_2O Subcell in a Silicon-Based Tandem Heterojunction Solar Cell”. In: *Green and Sustainable Chemistry* vol. 07, no. 01 (2017), pp. 57–69. DOI: 10.4236/gsc.2017.71005.

[108] A. Anders. “Tutorial: Reactive high power impulse magnetron sputtering (R-HiPIMS)”. In: *Journal of Applied Physics* vol. 121, no. 17 (2017), p. 171101. DOI: 10.1063/1.4978350.

[109] S. A. Campbell. *Fabrication Engineering at the Micro- and Nanoscale*. Oxford series in electrical and computer engineering. Oxford University Press, 2013.

[110] J. E. Prieto and I. Markov. “Stranski–Krastanov mechanism of growth and the effect of misfit sign on quantum dots nucleation”. In: *Surface Science* vol. 664 (2017), pp. 172–184. DOI: https://doi.org/10.1016/j.susc.2017.05.018.

[111] J. A. Thornton. “Influence of apparatus geometry and deposition conditions on the structure and topography of thick sputtered coatings”. In: *Journal of Vacuum Science and Technology* vol. 11, no. 4 (1974), pp. 666–670. DOI: 10.1116/1.1312732.

[112] P. Blood. *The electrical characterization of semiconductors : majority carriers and electron states*. eng. Vol. 14. Techniques of physics. London: Academic Press, 1992.

[113] S. Brochen, G. Feuillet, and J. Pernot. “Equivalence of donor and acceptor fits of temperature dependent Hall carrier density and Hall mobility data: Case of ZnO”. In: *Journal of Applied Physics* vol. 115, no. 16 (2014), p. 163706. DOI: 10.1063/1.4871397.

[114] D. C. Look. *Electrical Characterization of GaAs materials and devices*. New York, NY: Wiley, 1989.

[115] K. Karlsen. "Characterization of Li doped, magnetron sputtered Cu_2O thin films". MA thesis. University of Oslo, 2019.

[116] M. Zouaghi et al. "Hall mobility and hole density in photoactivated Cu_2O single crystals". In: *Solid State Communications* vol. 8, no. 22 (1970), pp. 1823–1825. DOI: https://doi.org/10.1016/0038-1098(70)90325-X.

[117] B. A. Tazenkov and F. A. Gruzdev. "Positive and negative photomemory in cuprous oxide". In: *Soviet Physics - Solid State* vol. 16 (1974), p. 460.

[118] Y. S. Lee et al. "Hall mobility of cuprous oxide thin films deposited by reactive direct-current magnetron sputtering". In: *Applied Physics Letters* vol. 98, no. 19 (2011), p. 192115. DOI: 10.1063/1.3589810.

[119] S. H. Jeong and E. S. Aydil. "Structural and electrical properties of Cu_2O thin films deposited on ZnO by metal organic chemical vapor deposition". In: *Journal of Vacuum Science & Technology A* vol. 28, no. 6 (2010), pp. 1338–1343. DOI: 10.1116/1.3491036.

[120] J. Frenkel. "On Pre-Breakdown Phenomena in Insulators and Electronic Semi-Conductors". In: *Phys. Rev.* vol. 54 (1938), pp. 647–648. DOI: 10.1103/PhysRev.54.647.

[121] J. G. Simmons and G. W. Taylor. "Nonequilibrium Steady-State Statistics and Associated Effects for Insulators and Semiconductors Containing an Arbitrary Distribution of Traps". In: *Phys. Rev. B* vol. 4 (2 1971), pp. 502–511. DOI: 10.1103/PhysRevB.4.502.

[122] H. N. Riise. "Materials and junctions for a novel oxide solar cell". PhD thesis. University of Oslo, 2018, pp. 137–140.

[123] Majid Toghyani Rizi, M.H. Shahrokh Abadi, and M. Ghaneii. "Two dimensional modeling of Cu_2O heterojunction solar cells based on β-Ga_2O_3 buffer". In: *Optik* vol. 155 (2018), pp. 121–132. DOI: 10.1016/j.ijleo.2017.11.028.

[124] M. A. Lloyd et al. "Intrinsic defect engineering of cuprous oxide to enhance electrical transport properties for photovoltaic applications". In: *2014 IEEE 40th Photovoltaic Specialists Conference (PVSC) Volume 2*. 2014, pp. 1–3. DOI: 10.1109/PVSC-Vol2.2014.7588254.

Papers

Paper I

Dominant Defects and Carrier Transport in Single Crystalline Cuprous Oxide: A New Attribution of Optical Transitions

Martin Nyborg, Kristin Bergum, Ilia Kolevatov, Geraldo C. Vásquez, Eduard Monakhov

This paper is published in Journal of applied Physics **130** (2021)

Journal of Applied Physics

Dominant defects and carrier transport in single crystalline cuprous oxide: A new attribution of optical transitions

Cite as: J. Appl. Phys. **130**, 175701 (2021); https://doi.org/10.1063/5.0059406
Submitted: 09 June 2021 • Accepted: 07 October 2021 • Published Online: 01 November 2021

M. Nyborg, Ilia Kolevatov, G. C. Vásquez, et al.

Journal of Applied Physics ARTICLE scitation.org/journal/jap

Dominant defects and carrier transport in single crystalline cuprous oxide: A new attribution of optical transitions

Cite as: J. Appl. Phys. **130**, 175701 (2021); doi: 10.1063/5.0059406
Submitted: 9 June 2021 · Accepted: 7 October 2021 ·
Published Online: 1 November 2021

M. Nyborg,[1,a)] Ilia Kolevatov,[1,2] G. C. Vásquez,[1] K. Bergum,[1] and E. Monakhov[1,a)]

AFFILIATIONS

[1]Department of Physics/Centre for Materials Science and Nanotechnology, University of Oslo, P.O. Box 1048 Blindern, Oslo N-0316, Norway
[2]Justervesenet, P.O. Box 170, Kjeller N-2007, Norway

[a)]**Authors to whom correspondence should be addressed:** martin.nyborg@fys.uio.no and eduard.monakhov@fys.uio.no

ABSTRACT

Electronic properties of single crystal (111) Cu_2O wafers have been investigated using a number of complementary techniques. Secondary ion mass spectrometry has shown significant presence of hydrogen and nitrogen. Cathodoluminescence measurements reveal strong near-band emission indicating the good electronic quality of the wafers. Two deep emission lines are observed at 1.3 and 1.7 eV. Temperature-dependent Hall effect measurements reveal electronic levels at around $E_V + 0.16$ eV, $E_V + 0.22$ eV, and $\sim E_V + 0.4$ eV, where E_V is the valence band edge. The discussion on the identity of the electronic centers calls for a revision of the traditional assignments of the 1.3-eV and 1.7-eV lines in order to take into account independent theoretical predictions. The temperature dependence of carrier mobility shows that the mechanism limiting the mobility can be described by scattering on neutral and ionized defect centers.

I. INTRODUCTION

Cuprous oxide (Cu_2O) is a direct bandgap semiconductor with a bandgap of ~2.17 eV.[1–3] It has been intensively studied for its promising properties for photovoltaic applications due to the abundance and non-toxicity, strong light absorption, and the possibility of thin-film processing. However, efficiencies for most thin-film devices have yet to surpass ~2%.[2] On the other hand, solar cells based on oxidized copper sheets have achieved efficiencies as high as 8%.[4] The challenge to achieve higher efficiencies is believed to be due to the inability to fully control defect concentrations in Cu_2O, where the excess acceptor concentrations are normally attributed to non-stoichiometry caused by cation deficiency through copper vacancies (V_{Cu}).[3]

Theoretical predictions on the properties of V_{Cu} by the density functional theory (DFT) are somewhat contradicting. According to Raebiger *et al.*,[5] V_{Cu} can have another configuration, the so-called split vacancy ($V_{Cu,split}$), that has higher formation energy for both neutral and negative charge states. $V_{Cu,split}$ is thus expected to be less energetically favorable. Both the configurations are predicted to have the acceptor transition (0/−) at around $E_V + 0.28$ eV, where E_V is the valence band edge. Later, Scanlon *et al.*[6] have estimated that neutral $V_{Cu}(0)$ and $V_{Cu,split}(0)$ have similar formation energies, which is in contrast to the calculations by Raebiger *et al.*[5] According to Scanlon *et al.*,[6] the acceptor transitions (0/−) for V_{Cu} and $V_{Cu,split}$ occur at $E_V + 0.23$ eV and $E_V + 0.47$ eV, respectively. One can see that both Raebiger *et al.*[5] and Scanlon *et al.*[6] agree on the preferred configuration for the negative charge state, while disagreeing somewhat on the relation between the formation energies for the neutral charge state.

Experimental studies on electronic properties of nominally intrinsic Cu_2O have routinely reported dominant acceptor levels around 0.2 eV and around 0.4–0.5 eV above E_V (see recent Refs. 7–10 and references therein). Over the decades, there have been a number of different identifications of these levels. Since the results were obtained for nominally intrinsic Cu_2O, the identifications were normally attributed to intrinsic defects, mostly to vacancy related defects. For instance, Paul *et al.*[7] have attributed the electronic level at $E_V + 0.45$ eV to a Cu-monovacancy and the level at $E_V + 0.25$ eV to a Cu-divacancy. After the DFT studies by Raebiger *et al.*[5] and

Scanlon *et al.*,[6] the assignments tend to involve V_{Cu} and $V_{Cu,split}$. One can notice, however, that the effect of unintentional impurities has not been seriously considered and investigated.

Nitrogen is one of the most established acceptor dopants in Cu_2O. Nitrogen substituting oxygen (N_O) is routinely assigned to a shallow acceptor level at 0.12–0.18 eV above E_V.[11–13] This range is in agreement with the estimate based on the effective mass approximation, which gives a theoretical activation energy of 0.16 eV.[11] However, recent DFT calculations could not place N_O as a shallow acceptor. It was reported to have a deeper level at $\sim E_V + 0.5$ eV, making it a less likely candidate as a dominant shallow acceptor in Cu_2O (see recent Ref. 14 and references therein). Instead, nitrogen is proposed to mainly replace Cu in its molecular form, as $(N_2)_{Cu}$,[14] which is supported by experimental results showing that nitrogen is present in Cu_2O predominantly as N_2.[15] Finally, it is calculated that $(N_2)_{Cu}$ has a shallower acceptor level at ~0.2 eV.[16] It is interesting to note that Malerba *et al.*[17] have shown direct evidence of optical absorption around 0.5–0.7 eV associated with nitrogen induced electronic levels. This observation is consistent with the DFT results on the acceptor level of N_O at $\sim E_V + 0.5$ eV.[14]

Although hydrogen is known to be an abundant impurity in oxides, our understanding of its properties in Cu_2O is limited. According to Van de Walle and Neugebauer[18] isolated interstitial hydrogen (H_i) is a negative-U center in various semiconductors. It has been calculated that the positive charge state, $H_i(+)$, tends to take the bond-centered (BC) configuration, while the negative charge state, $H_i(-)$, tends to take the tetrahedral (tet) configuration. The negative-U behavior is thus attributed to the electronic and structural transition between $H_{i,BC}(+)$ and $H_{i,tet}(-)$. The calculations suggest that for the majority of semiconductors, the electronic level for the transition between $H_{i,BC}(+)$ and $H_{i,tet}(-)$ is universally aligned with respect to the vacuum level. The DFT calculations put this level at around 4.5 eV below the vacuum level.[18] Adopting this hypothesis and taking the electron affinity of Cu_2O as 3.1 eV,[2,3] one can estimate that the expected level in Cu_2O is at ~1.4 eV below the conduction band (E_C) or at ~0.8 eV above E_V.

First, DFT calculations on some hydrogen-related complexes have been reported by Scanlon and Watson.[19] Several possible atomic configurations for H_i have been calculated, including tetrahedral, octahedral, bond-centered, and anti-bonding configurations. Unfortunately, the transition between $H_{i,BC}(+)$ and $H_{i,tet}(-)$ has not been explicitly considered, and the hypothesis on the universal alignment has not been explicitly checked for Cu_2O. The calculations by Scanlon and Watson[19] have also demonstrated the ability of hydrogen to passivate V_{Cu}. The hydrogen-V_{Cu} complex (H-V_{Cu}) has been shown to have the lowest formation energy among the considered complexes. It is predicted to have the donor level (+/0) at around $E_V + 0.1$ eV and the acceptor level (0/−) at around $E_V + 1.2$ eV.

The experimental reports on the role of hydrogen in Cu_2O are quite scarce. Hering *et al.*[20] have reported on improved carrier transport properties when hydrogen is introduced during Cu_2O deposition by magnetron sputtering. This is attributed to hydrogen passivating donor-like states, resulting in improved mobility in the films. The study also highlights an increase in acceptor ionization energy with higher hydrogen flow during growth, which can be interpreted as the appearance of a hydrogen-related defect with higher activation energy. Tabuchi and Matsumura[21] and Kumar *et al.*[22] also report on improved mobility in hydrogen enriched Cu_2O. The increased mobility is accompanied by a decrease in carrier concentration, which suggests either passivation of acceptors by hydrogen or an increase in the acceptor activation energy. These findings are consistent with theoretical predictions on hydrogen passivation of vacancies by Scanlon and Watson.[19]

The literature shows that the majority of studies are performed on magnetron-sputtered films or thermally oxidized copper sheets. In this work, we report on the dominant electronic states in single crystalline Cu_2O. We employ a number of complementary techniques to establish and identify the dominant electronic states.

II. EXPERIMENTAL DETAILS

Two commercially available natural single crystal Cu_2O wafers from SurfaceNET with a resistivity of 20 kΩ cm were used in the study. The wafers had (111)-orientation and a size of 1×1 cm^2 with a thickness of 500 μm. One of the wafers was measured by x-ray diffraction (XRD) before it was cut into smaller samples for Schottky diode fabrication, Secondary Ion Mass Spectrometry (SIMS), and Cathodoluminescence (CL) measurments. Another wafer was used for the temperature-dependent Hall (TDH).

SIMS measurements of hydrogen and nitrogen concentrations were conducted in a Cameca IMS7f microanalyzer with Cs^+ primary ions at 15 keV. Reference samples were used to quantify the concentrations in the Cu_2O wafers studied. The reference samples used were magnetron sputtered, phase-pure Cu_2O films ion-implanted with known doses of hydrogen and nitrogen. The implantation of hydrogen was performed with an energy of 20 keV and a dose of 1×10^{16} cm^{-2}. These implantation conditions resulted in a hydrogen profile with a peak concentration of 8×10^{20} cm^{-3} at a depth of ~160 nm. The implantation of nitrogen was done with the same dose 1×10^{16} cm^{-2} and an ion energy of 80 keV. This energy was chosen in order to provide a nitrogen depth profile similar to that of hydrogen. The resulting nitrogen profile has a peak concentration of 8×10^{20} cm^{-3} at a depth of ~120 nm. The SIMS measurements were carried out for the reference samples and the studied single crystalline wafers at the same measurement conditions on the same day. The count rates of the secondary ions were then calibrated using the reference samples. This calibration was used to deduce the concentrations from the rate counts for the analyzed single crystal samples. The measurements revealed a high concentration of hydrogen in the Cu_2O wafers: as high as 3×10^{19} cm^{-3}. Nitrogen concentration was established to be $\sim 7 \times 10^{17}$ cm^{-3}.

Structural characterization was performed using X-ray Diffraction (XRD) in a Bragg–Brentano geometry and Cu$K_{\alpha 1}$ radiation selected by a GE(002) asymmetric monochromator on the primary beam side. The scans were performed in a Bruker AXS D8 Discovery XRD system.

CL was studied with a JEOL JSM-IT300 SEM with a Delmic SPARC CL system equipped with an Andor Shamrock SR-193i spectrometer, a 300 l/mm grating, and a charged couple device (CCD) Andor Newton DU940P-BU2, allowing us to achieve 0.97 nm spectral resolution. The CL spectra were recorded at 80 K with acceleration voltages of 3, 5, 10, and 20 keV and a probing current of 100 pA.

Free carrier density has been assessed by TDH measurements conducted with two different Lakeshore 7604 setups, one configured for low-temperature measurements (20–300 K) and one for high temperature (300–700 K). The sample was first measured in the low-temperature setup at 120–300 K, subsequently, it was measured in the high temperature setup at 300–550 K.

Circular Al contacts with a diameter of 0.5 mm were deposited by thermal evaporation through a shadow mask. Subsequently, Au was deposited over the whole backside surface as the back contact. This resulted in Schottky diodes with rectifications of ∼2 orders of magnitude. Thermal admittance spectroscopy (TAS) was performed under 1 V reverse bias with an Agilent 4280A LCR meter with probe frequencies between 10 kHz and 1 MHz and 20 mV amplitude.

III. RESULTS AND DISCUSSION

The XRD pattern of a θ–2θ scan (Fig. 1) reveals two dominant peaks at 36.43° and 77.35°. The peaks correspond to diffraction at (111) and (222) planes of Cu_2O. This confirms phase-pure, single crystalline Cu_2O with the orientation along the [111] direction. The lattice constant $a = 4.269 \pm 0.004$ Å was obtained from the position of the [111] reflection and is in good agreement with the literature value of 4.270 ± 0.001 Å.[3] The two minor peaks marked by asterisks originate from the Al sample holder. One can also observe an indication of a minor peak at ∼33°. At the moment, we cannot make a conclusive claim on the origin of this peak. One can speculate that it can be due to (110) CuO since the presence of CuO inclusions or a thin CuO surface layer cannot be excluded.[23] On the other hand, we do not observe the diffraction on (220) CuO, expected at ∼70° with a similar intensity.

Figure 2 depicts CL spectra measured at 80 K with different electron-beam energies, the spectra are consistent with each other and indicate good crystal quality and uniformity. The spectra reveal strong and sharp near-band emission (NBE) lines in the photon energy range 1.9–2.1 eV. In addition, two broad, strong luminescence bands are observed at around 1.3 and 1.7 eV.

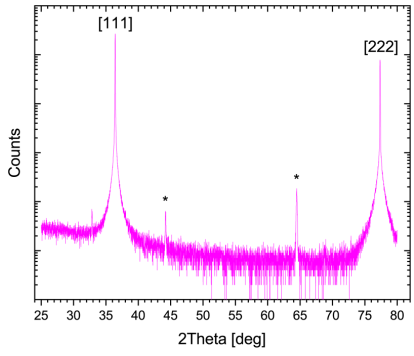

FIG. 1. θ-2θ XRD scan for the Cu_2O sample. Asterisks denote minor peaks that originate from the sample holder.

Similar transitions were routinely observed by photoluminescence (PL) already over half a century ago (see Ref. 24 and references therein). First tentative identification was put forward by Bloem *et al.*,[24] where the luminescence peak at ∼1.2–1.3 eV was attributed to the acceptor state of V_{Cu}, and the peak at ∼1.7 eV was assigned to a donor state of oxygen vacancy (V_O). Later, Gastev *et al.*[25] assigned the emission at ∼1.7 eV to a double donor state of oxygen vacancy (V_O^{2+}), which was based on previous studies by Zouaghi *et al.*[26] using infrared absorption and photoconductivity. Since then, this identification has been routinely repeated in the literature (see Refs. 2 and 3 and references therein). Apparently, these identifications contradict the DFT studies by both Raebring *et al.*[5] and Scalon *et al.*[6,19] First, V_O is predicted to be electrically neutral without electronic levels in the bandgap.[5,6,19] Second, the assignment of the 1.3-eV peak to V_{Cu} would imply that the acceptor level of V_{Cu} is at $E_V + 0.8$ eV, which also contradicts to the DFT predictions.[5,6,19]

Based on the DFT calculations, one can put forward another identification of the deep emission lines. The photon energy 1.3 eV is close to the energy for the acceptor level of H-V_{Cu}, which was put by Scanlon and Watson[19] at $\sim E_V + 1.2$ eV. Since hydrogen is abundant in the studied samples, as shown by SIMS, it is tempting to attribute the 1.3-eV emission line to H-V_{Cu}. The 1.7-eV emission line can be tentatively attributed to the acceptor transition of $V_{Cu,split}$ that is predicted to have the level at $E_V + 0.47$ eV,[6,19] i.e., at $\sim E_C - 1.7$ eV. The latter identification would then imply that either (i) $V_{Cu,split}$ is the preferred and dominant configuration compared to V_{Cu} or (ii) the radiative transition for $V_{Cu,split}$ is significantly more efficient compared to that for V_{Cu}.

Five different NBE peaks can be detected in the CL spectra and labeled as peaks 1–5 (Fig. 2). One can observe that the shape of the NBE in the present experiment is quite similar to that reported previously for high-quality Cu_2O films with photoluminescence (PL).[27] This leads to a peak identification similar to that in Ref. 27. The separation between peaks 4 and 5 is 0.025 eV, which is in good agreement with the PL data.[27] The peaks are, thus, identified as the orthoexcitonic (X_o) emission coupled with absorption or emission of the Γ^-_{12} phonon, where peak 5 at 2.043 eV is attributed to the absorption of the phonon ($X_o + \Gamma^-_{12}$) and peak 4 at 2.018 eV is due to the emission ($X_o - \Gamma^-_{12}$). Since the energy of the Γ^-_{12} phonon is 0.0125 eV, one can deduce the phonon-free X_o emission energy as the center point between peaks 4 and 5, which is 2.030 eV. Taking the exciton binding energy 0.14 eV[28] results in a bandgap of 2.17 eV at 80 K. Peak 3 at 1.974 eV is 0.056 eV below the X_o emission, which is close to the Γ^+_{25} phonon energy reported at 0.064 eV.[29] Hence, we identify peak 3 as X_o coupled with emission of the Γ^+_{25} phonon ($X_o - \Gamma^+_{25}$). Similarly, peak 2 at 1.950 eV is identified as X_o coupled with emission of the Γ^{-2}_{15} phonon ($X_o - \Gamma^{-2}_{15}$) by its relative position of 0.08 eV below the X_o emission energy, which is close to the reported value of 0.082 eV for the Γ^{-2}_{15} phonon by Petroff *et al.*[29] Finally, peak 1 was previously assigned to the emission of the Γ^{-2}_{15} and Γ^+_{25} phonons at 1.875 eV.[27] On the other hand, the peak position at 1.891 eV is in good agreement with the energy 1.89 eV calculated by T-Thienprasert and Limpijumnong[16] for optical transition for $(N_2)_{Cu}$. Within the present experiment, however, we cannot conclusively favor one or another assignment for peak 1. The suggested assignments and energy position of the peaks are summarized in Table I.

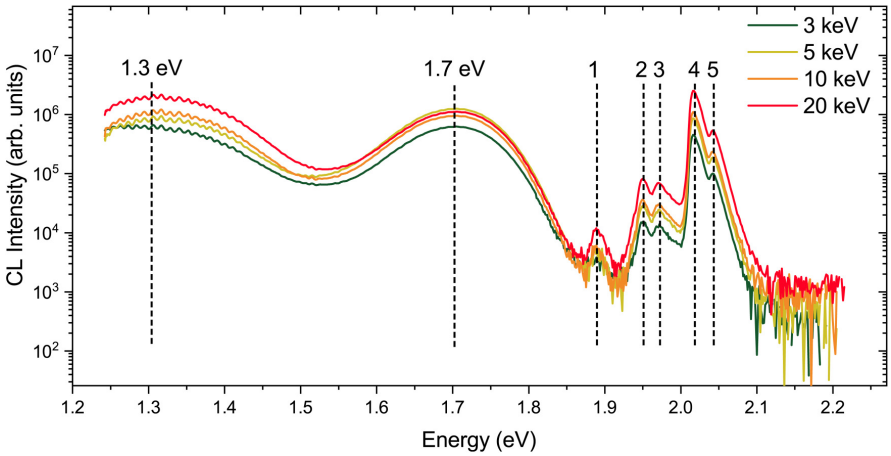

FIG. 2. CL at 80 K in the photon energy range 1.2–2.2 eV recorded for different electron-beam energies: 3, 5, 10, and 20 keV. The assignment of the NBE lines (peaks 1–5) is summarized in Table I.

TDH measurements were conducted to evaluate the electrical transport properties of the Cu_2O crystal (Fig. 3). The measurements reveal p-type conductivity of Cu_2O with a carrier density of $6.7 \times 10^{12}\,cm^{-3}$ and a hole mobility of 48 $cm^2/(Vs)$ at room temperature. One can see that the hole concentration is considerably less compared to nitrogen concentration and the expected concentration of V_{Cu} (around 10^{18}–$10^{20}\,cm^{-3}$).[5] This indicates that the material is highly compensated, presumably with unintentional donor impurities.

As the temperature increases, the hole concentration increases in a closely Arrhenius behavior [Fig. 3(a)]. For a compensated material, the hole concentration can be express by the following relation:[30]

$$p \approx \frac{g_a N_v (N_a - N_d)}{N_d} \exp\left(-\frac{\Delta E_a}{kT}\right), \quad (1)$$

where p is the hole density, N_a is acceptor concentration, N_d is compensating donor concentration, g_a is the degeneracy factor, N_v is the density of states at the valence band, k is Boltzman constant, T is temperature, and E_a is the ionization energy of the acceptor state. One can tentatively identify two slopes of similar magnitudes in Fig. 3(a) that correspond to acceptor activation energies of 0.16 and 0.22 eV. The acceptor concentrations cannot be unambiguously deduced due to incomplete ionization in the investigated temperature range. However, a lower limit estimate can be made for both of the acceptors. This results in the densities $\geq 10^{16}\,cm^{-3}$ for the acceptor at 0.16 eV and $\geq 10^{17}\,cm^{-3}$ for the acceptor at 0.22 eV.

TABLE I. NBE transitions in CL at 80 K and their assignments.

Peak	Energy position (eV)	Assignment
1	1.891	$X_O - \Gamma_{25}^{+} - \Gamma_{15}^{-2} \rightarrow \Gamma_7^{+}$ or $(N_2)_{Cu}$
2	1.950	$X_O + \Gamma_{15}^{-2} \rightarrow \Gamma_7^{+}$
3	1.974	$X_O + \Gamma_{25}^{+} \rightarrow \Gamma_7^{+}$
4	2.018	$X_O - \Gamma_{12}^{-} \rightarrow \Gamma_7^{+}$
5	2.043	$X_O + \Gamma_{12}^{-} \rightarrow \Gamma_7^{+}$

One can speculate that the steepening of the slope in the TDH data from 0.16 to 0.22 eV with increasing temperature may not be a manifestation of two different states, but rather a result of other effects. Fitting of the TDH data with a single level to the whole temperature range gives an activation energy of 0.19 eV. However, we tend to assume two distinct levels. This is based on the previous reports on Cu_2O doping with nitrogen:[12,13,31] (1) TDH measurements on undoped Cu_2O reveals acceptors with an activation energy of ≥0.2 eV. (2) The doping results in a decrease in the activation energy down to 0.12 eV. Such behavior suggests two distinct acceptors. The acceptor in the undoped Cu_2O can be assigned to V_{Cu} with the acceptor level at $\sim E_V + 0.25$ eV.[6,7] The acceptor with the activation energy 0.12 eV was attributed to nitrogen, in accordance with previous reports that put the nitrogen level at 0.12–0.18 eV above E_V.[11–13] In line with the literature, we attribute (i) the level at 0.16 eV [Fig. 3(a)] to a nitrogen-related acceptor and (ii) the acceptor with the activation energy 0.22 eV to V_{Cu}.

A sharp increase in carrier concentration is observed at the higher temperature limit of the measurements. This increase corresponds to an activation energy of ∼0.4 eV. Two possible explanations can be put forward: (1) there is another deeper acceptor with a level at $\sim E_V + 0.4$ eV and (2) there is an increase in the concentration of shallows acceptors, which is governed by the formation

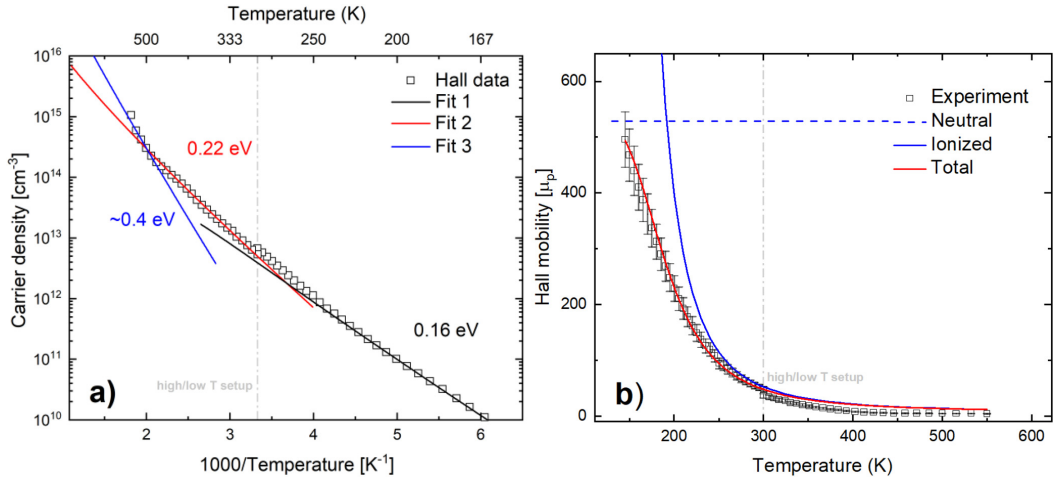

FIG. 3. (a) Hole concentration vs the inverse temperature (squares) as determined by the Hall effect measurement. Exponential fits [Eq. (1)] are indicated with solid lines. (b) Hole mobility as a function of temperature (squares). Curves show the total mobility and contributions from neutral and ionized impurities according to Eq. (3).

energy ~0.4 eV. We favor the former interpretation. First, a similar acceptor has been observed previously by Paul *et al.*[7] and Papadimitriou.[9] Second, the acceptor level at $\sim E_V + 0.4$ eV is consistent with the results of CL measurements, where the 1.7-eV emission can be attributed to a level at $E_C - 1.7$ eV, i.e., at $E_V + 0.47$ eV. We assign this level to $V_{Cu,split}$.

The Hall mobility has a strong dependence on temperature and is shown in Fig. 3(b). Previous studies of hole transport in Cu_2O by Shimada and Masuimo[32] did not result in a consistent picture for hole mobility as a function of temperature: In the low-temperature limit, an acceptable agreement could be made from the combination of phonon LO scattering, acoustical phonon scattering, and neutral impurities. In the higher temperature range, however, another dominating mobility limiting mechanism had to be assumed. To account for the observed rapid decline in mobility, the formation of a metastable self-trapped state has been suggested.[32] A similar rapid decline in mobility is reported by Matsuzaki *et al.*[33] for temperatures above 200 K.

As shown by SIMS, the samples contain a considerable concentration of impurities, with hydrogen concentration (3×10^{19} cm^{-3}) significantly higher than that considered by Shimada and Masuimo.[32] The material is believed to be strongly compensated and contain a significant concentration of both neutral and ionized impurities. It appears to be a reasonable assumption that the main limiting mechanism for hole mobility is scattering at impurities, both neutral and ionized. One can express the total hole mobility, μ, as

$$\mu = \left(\frac{1}{\mu_n} + \frac{1}{\mu_i}\right)^{-1}, \tag{2}$$

where μ_n is the mobility limited by neutral impurities and μ_i is the mobility limited by ionized impurities. Figure 3(a) shows that the hole concentration and, hence, the concentration of ionized impurities, N_i, strongly increases with temperature as an activation-type dependence, $N_i \sim \exp(-E_a/kT)$, where E_a is the activation energy. Both Conwell–Weisskopf and Brooks–Herring approximations (see, for instance, Ref. 34) state that μ_i is inversely proportional to the concentration of ionized impurities and roughly proportional to $T^{3/2}$. One can, thus, express μ_i as $\mu_i = \alpha T^{3/2}/\exp(-E_a/kT)$, where α is the proportionality coefficient. Assuming μ_n is temperature independent, the hole mobility can be expressed as a function of temperature,

$$\mu = \left(\frac{1}{\mu_n} + \frac{\exp(-E_a/kT)}{\alpha T^{3/2}}\right)^{-1}. \tag{3}$$

This expression was fitted to the experimental data in Fig. 3(b). The fitting appears to be satisfactory and yields $\mu_n = 550$ cm^2 V^{-1} s^{-1}, $\alpha = 5.17 \times 10^{-5}$ cm^2 V^{-1} s^{-1} K$^{-3/2}$ and $E_a = 0.14$ eV. Besides, E_a deduced from the mobility data is consistent with the activation energies (0.16–0.22 eV) deduced from the hole concentration data in Fig. 3(a). We conclude that the model can describe the temperature dependence of the mobility.

Figure 4 shows the results of TAS measurements[30] with capacitance [Fig. 4(a)] and conductance [Fig. 4(b)] as functions of temperature for different frequencies and the Arrhenius plot for the emission rates [Fig. 4(c)]. Two dominant electronic levels are evident and manifested as two step-like changes in the capacitance measurements [Fig. 4(a)] and as two peaks in

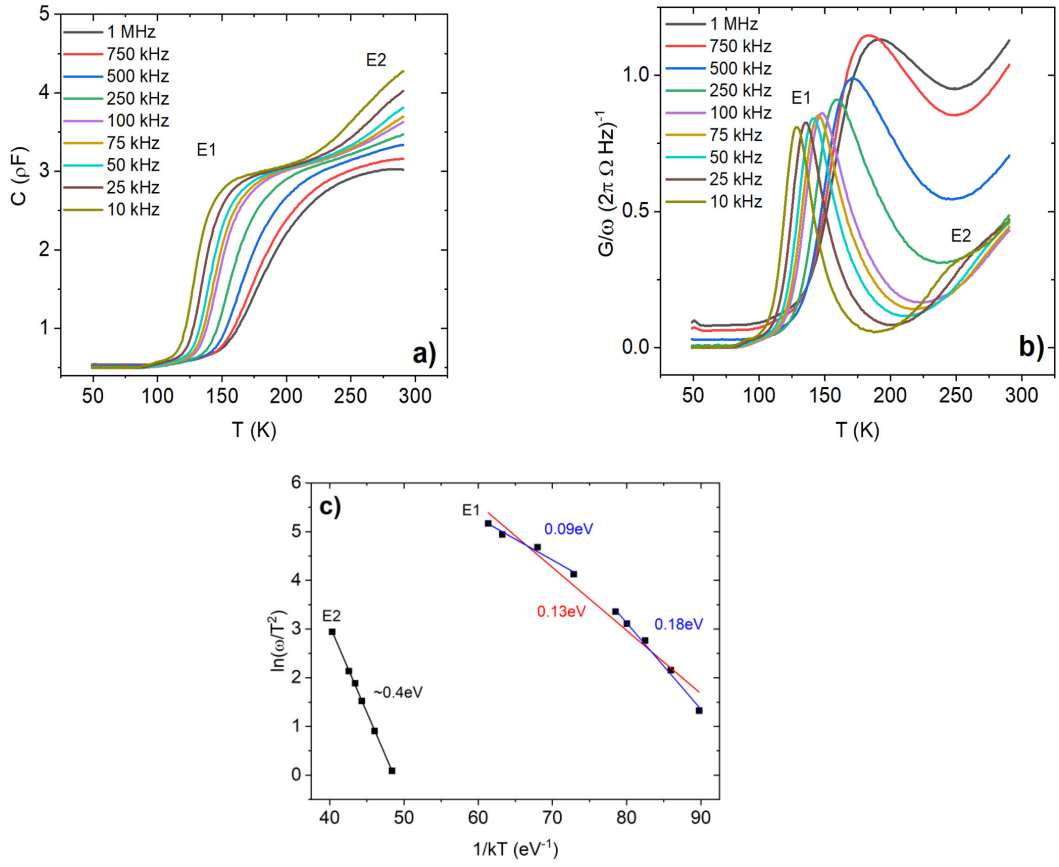

FIG. 4. TAS measurements with capacitance, C (a) and conductance over the angular frequency, G/ω (b) vs temperature for nine different probing frequencies. (c) Arrhenius plot of $\ln(\omega/T^2)$ vs 1/kT for the observed electronic states.

the conductance measurements [Fig. 4(b)]. One level is evident in the 100–200 K range, while another can be observed at >250 K. Arrhenius analysis of the shallower level yield an activation energy of 0.13 eV. One can notice, however, that the emission rate does not demonstrate a clear Arrhenius dependence on the reciprocal temperature. This can be explained by (i) temperature dependence of the capture cross section or (ii) the presence of two overlapping electronic levels. This observation is similar to that for TDH, where two closely positioned acceptor levels are observed [Fig. 3(a)]. Using this interpretation, the two levels are indicated by the additional lines in Fig. 4(c), which results in two levels at 0.09 eV and 0.18 eV above E_V. In line with the interpretation of the TDH data, we assign the level observed with TAS at 0.09 0eV to that observed with TDH at 0.16 eV and attributed to a nitrogen-related acceptor. The level observed with TAS at 0.18 eV is assigned to that observed with TDH at 0.22 eV and identified as the acceptor level of V_{Cu}.

The increasing capacitance and conductance at >250 K indicate the presence of a deeper level [Figs. 4(a) and 4(b)]. This level is particularly visible for lower frequencies. Using the data for these frequencies, the level is estimated to be ~0.4 eV above E_V. This is consistent with the deeper level at 0.4 eV observed by TDH [Fig. 3(a)]. We thus assign this level to $V_{Cu,split}$.

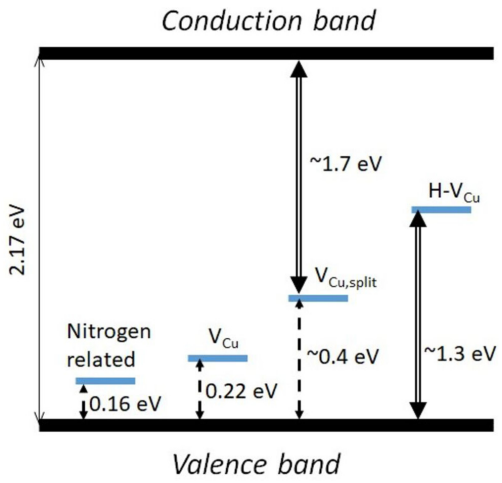

FIG. 5. Schematic illustration of the levels within the bandgap proposed in the present study. Dashed arrows indicate electronic transitions deduced by TDH. The solid double-line arrows denote optical transitions observed by CL.

The proposed assignments of the electronic levels and the corresponding optical transitions are illustrated in Fig. 5. It should be emphasized that the electronic and optical transitions observed in the present study are similar to those observed in other experiments reported in the literature. This suggests that the samples investigated in the present study are representative and comparable to those reported in the literature. Thus, the considerations on the identity of the levels are applicable to identifications reported previously.

IV. CONCLUSION

The dominant electrically active centers and carrier transport in single crystal Cu_2O wafers are studied by several complementary techniques. The measurements reveal electronic levels at around $E_V + 0.16$, $E_V + 0.22$, $E_V + 0.4$, and $E_V + 1.3$ eV. In line with previous identifications, the level at 0.16 eV is assigned to a nitrogen-related acceptor, and the levels at 0.22 and ~0.4 eV are assigned to the acceptor states of V_{Cu} and $V_{Cu,split}$. The level at $E_V + 1.3$ eV is believed to be responsible for the emission line at 1.2–1.3 eV, which is routinely observed in PL and CL measurements. In contrast to the identification as V_{Cu}, normally given in the literature, we tend to attribute this level to the acceptor state of H-V_{Cu}. The origin of another routinely observed emission line at ~1.7 eV is argued to be the acceptor level of $V_{Cu,split}$, as opposed to a widely accepted identification as V_O. In addition, we demonstrate that the mechanism limiting carrier mobility can be described by scattering on neutral and ionized defect centers.

ACKNOWLEDGMENTS

This work was performed within The Norwegian Research Center for Sustainable Solar Cell Technology (FME SUSOLTECH, Project No. 257639/E20). The center is co-sponsored by the Research Council of Norway and its research and industry partners. The Research Council of Norway is acknowledged for the support to the Norwegian Micro- and Nano-Fabrication Facility, NorFab, Project No. 295864, and FUNDAMeNT, Project No. 251131.

AUTHOR DECLARATIONS

Conflict of Interest

The authors have no conflicts to disclose.

DATA AVAILABILITY

The data that support the findings of this study are available from the corresponding authors upon reasonable request.

REFERENCES

[1]C. Malerba, F. Biccari, C. Leonor Azanza Ricardo, M. D'Incau, P. Scardi, and A. Mittiga, Sol. Energy Mater. Sol. Cells **95**, 2848 (2011).
[2]B. K. Meyer, A. Polity, D. Reppin, M. Becker, P. Hering, P. J. Klar, T. Sander, C. Reindl, J. Benz, M. Eickhoff, C. Heiliger, M. Heinemann, J. Blasing, A. Krost, S. Shokovets, C. Muller, and C. Ronning, Phys. Status Solidi B **249**, 1487 (2012).
[3]B. Meyer, A. Polity, D. Reppin, M. Becker, P. Hering, B. Kramm, P. Klar, T. Sander, C. Reindl, C. Heiliger, M. Heinemann, C. Muller, and C. Ronning, *Oxide Semiconductors*, Semiconductors and Semimetals (Elsevier, 2013), p. 201.
[4]T. Minami, Y. Nishi, and T. Miyata, Appl. Phys. Express. **9**, 052301 (2016).
[5]H. Raebiger, S. Lany, and A. Zunger, Phys. Rev. B **76**, 045209 (2007).
[6]D. O. Scanlon, B. J. Morgan, G. W. Watson, and A. Walsh, Phys. Rev. Lett. **103**, 096405 (2009).
[7]G. K. Paul, Y. Nawa, H. Sato, T. Sakurai, and K. Akimoto, Appl. Phys. Lett. **88**, 141901 (2006).
[8]Y. S. Lee, M. T. Winkler, S. C. Siah, R. Brandt, and T. Buonassisi, Appl. Phys. Lett. **98**, 192115 (2011).
[9]L. Papadimitriou, Solid-State Electron. **36**, 431 (1993).
[10]G. P. Pollack and D. Trivich, J. Appl. Phys. **46**, 163 (1975).
[11]S. Ishizuka, S. Kato, T. Maruyama, and K. Akimoto, Jpn. J. Appl. Phys. **40**, 2765 (2001).
[12]J. Li, Z. Mei, L. Liu, H. Liang, A. Azarov, A. Kuznetsov, Y. Liu, A. Ji, Q. Meng, and X. Du, Sci. Rep. **4**, 7240 (2014).
[13]J. Benz, K. P. Hering, B. Kramm, A. Polity, P. J. Klar, S. C. Siah, and T. Buonassisi, Phys. Status Solidi B **254**, 1600421 (2017).
[14]Y. Wang and J. F. Pierson, J. Phys. D: Appl. Phys. **54**, 263002 (2021).
[15]Y. Wang, J. Ghanbaja, D. Horwat, L. Yu, and J. F. Pierson, Appl. Phys. Lett. **110**, 131902 (2017).
[16]J. T-Thienprasert and S. Limpijumnong, Appl. Phys. Lett. **107**, 221905 (2015).
[17]C. Malerba, C. L. Azanza Ricardo, M. D'Incau, F. Biccari, P. Scardi, and A. Mittiga, Sol. Energy Mater. Sol. Cells **105**, 192 (2012).
[18]C. G. Van de Walle and J. Neugebauer, Nature **423**, 626 (2003).
[19]D. O. Scanlon and G. W. Watson, Phys. Rev. Lett. **106**, 186403 (2011).
[20]K. P. Hering, C. Kandzia, J. Benz, B. G. Kramm, M. Eickhoff, and P. J. Klar, J. Appl. Phys. **120**, 185705 (2016).
[21]N. Tabuchi and H. Matsumura, Jpn. J. Appl. Phys. **41**, 5060 (2002).

[22]R. Kumar, K. Bergum, H. N. Riise, E. Monakhov, A. Galeckas, and B. G. Svensson, J. Alloys Compd. **825**, 153982 (2020).
[23]S. Poulston, P. M. Parlett, P. Stone, and M. Bowker, Surf. Interface Anal. **24**, 811 (1996).
[24]J. Bloem, A. J. Van der Houven van Oordt, and F. A. Kröger, Physica **22**, 1254 (1956).
[25]S. V. Gastev, A. A. Kaplyanskii, and N. S. Sokolov, Solid State Commun. **42**, 389 (1982).
[26]M. Zouaghi, B. Prevot, C. Carabatos, and M. Sieskind, Phys. Status Solidi A **11**, 449 (1972).
[27]K. Bergum, H. N. Riise, S. Gorantla, P. F. Lindberg, I. J. T. Jensen, A. E. Gunnæs, A. Galeckas, S. Diplas, B. G. Svensson, and E. Monakhov, J. Phys.: Condens. Matter **30**, 075702 (2018).
[28]K. Shindo, J. Phys. Soc. Jpn. **36**, 1583 (1974).
[29]Y. Petroff, P. Y. Yu, and Y. R. Shen, Phys. Rev. B **12**, 2488 (1975).
[30]P. Blood, *The Electrical Characterization of Semiconductors Majority Carriers and Electron States* (Academic Press Inc., San Diego, CA, 1992).
[31]Y. S. Lee, J. Heo, M. T. Winkler, S. C. Siah, S. B. Kim, R. G. Gordon, and T. Buonassisi, J. Mater. Chem. A. **1**, 15416 (2013).
[32]H. Shimada and T. Masumi, J. Phys. Soc. Jpn. **58**, 1717 (1989).
[33]K. Matsuzaki, K. Nomura, H. Yanagi, T. Kamiya, M. Hirano, and H. Hosono, Appl. Phys. Lett. **93**, 202107 (2008).
[34]D. Chattopadhyay and H. J. Queisser, Rev. Mod. Phys. **53**, 745 (1981).

Paper II

Deposition and Characterization of Lithium Doped Direct Current Magnetron Sputtered Cu_2O Films

Martin Nyborg, Alexander Azarov, Kristin Bergum, Eduard Monakhov

This paper is published in Thin Solid Films **722** (2021)

II

Thin Solid Films 722 (2021) 138573

Contents lists available at ScienceDirect

Thin Solid Films

journal homepage: www.elsevier.com/locate/tsf

Deposition and characterization of lithium doped direct current magnetron sputtered Cu_2O films

M. Nyborg *, A. Azarov, K. Bergum, E. Monakhov

Department of physics, center of Materials Science and Nanotechnology, University of Oslo, PO Box 1048, Blindern, N-0316 Oslo, Norway

ARTICLE INFO

Keywords:
Cuprous oxide
Lithium doping
Reactive sputtering
Optical properties
Electrical properties

ABSTRACT

Lithium doped cuprous oxide ($Cu_2O:Li$) films were deposited on quartz substrates by direct current magnetron reactive co-sputtering of copper and $Cu:Li$ targets. X-ray diffraction (XRD), secondary ion mass spectrometry (SIMS), Rutherford backscattering spectrometry, UV-VIS transmittance, and room temperature Hall measurements have been conducted to characterize the deposited films. SIMS revealed Li concentrations in the range $2\times10^{18}-5\times10^{20}\,cm^{-3}$ in the doped films. XRD confirms phase pure Cu_2O for all doping concentrations. The doping concentration correlates with an increased free carrier density found from Hall effect measurements. The highest Li doping concentration results in low resistivity ($4\,\Omega cm$) p-type Cu_2O with acceptor concentrations up to $2\times10^{17}\,cm^{-3}$.

1. Introduction

Cu_2O is a p-type semiconductor with a direct bandgap of 2.1 eV and a high absorption coefficient. It is stable, abundant, non-toxic and has the potential for low cost production schemes [1]. Cu_2O single junction solar cells have a theoretical efficiency of 19% [2]. Minami et al. has shown steep progress with a record efficiency of 8.1% in a bulk Cu_2O absorber based device [3]. Further, the band gap makes Cu_2O a candidate material for tandem solar cells, with an intriguing possibility as the top cell paired with a silicon bottom cell [4].

Cu_2O can be deposited by most thin-film methods, e.g., electrodeposition [5], molecular beam epitaxy [6], atomic layer deposition [7], radio frequency (RF) [8] and direct current (DC) reactive magnetron sputtering [9]. Magnetron sputtering and electrodeposition are most common in solar cell applications and is scalable for large scale production. Many known metal oxide semiconductors' are prone to low-charge carrier lifetimes and carrier mobilities. This is especially valid in sputtered Cu_2O based devices, which have yet to surpass efficiencies of 2-3% [10]. In Cu_2O, this is likely due to poor defect control and low mobility, which results in the inability to control the p-type nature of Cu_2O. The p-type conductivity is generally accepted to be due to persistent intrinsic acceptor states of copper vacancies (V_{Cu}), and so-called split-vacancies (V_{Cu}^{Split}) [11–18].

Doping of Cu_2O is widely explored, with transition metals, hydrogen, silicon, nitrogen, and more [19]. Most notably are the properties of nitrogen-doped p-type Cu_2O, with low resistivity and the possibility of tuning the electrical properties of Cu_2O [9,20]. There are no reports of viable routes to n-type conductivity in sputtered Cu_2O films, and most dopants lead to an increase in acceptor concentration. Isseroff and Carter [18] presented Lithium (Li) as an isovalent substitutionary cation with similar ionic size of Li^+ as that of Cu^+. Density functional theory calculations suggest that Li doping can form $V_{Cu}-Li$ complex in Cu_2O. The optimal defect complex structure was identified as Li tetrahedrally coordinated to four oxygen atoms, similar to V_{Cu}^{split}, resulting in a large driving force to cluster [18]. Besides, Li at the interstitial site (Li_i) can be expected to act as a donor. Thus, Li could be a route to passivate the high acceptor density in Cu_2O.

There is little literature on the effect of Li doping of Cu_2O, with only a few studies reporting increased carrier concentrations and increased conductivity in doped films [5,21,22]. In this work we investigate the effect of Li doping with varied concentrations in Cu_2O. Cu_2O films were deposited on quartz substrates by reactive co-sputtering of pure copper, 1% and 0.01% Li doped copper targets. Characterization of the films was carried out by X-ray diffraction (XRD), secondary ion mass spectrometry (SIMS), Rutherford backscattering spectrometry (RBS), UV-VIS transmittance, and room temperature Hall measurements (RTH).

2. Experimental details

Cu_2O films were deposited on 1×1 cm^2 fused silica substrates (t =

* Corresponding author.

https://doi.org/10.1016/j.tsf.2021.138573
Received 7 May 2020; Received in revised form 11 January 2021; Accepted 4 February 2021
Available online 9 February 2021

500 μm) by reactive DC and RF magnetron co-sputtering in a Semicore Triaxis system. The fused silica substrates were cleaned for 1 min in Pirhana solution, rinsed in DI water, and subsequently ultrasonically washed in isopropanol for 5 min. The base pressure in the deposition chamber was below 2.7 $\times 10^{-4}$ Pa (2 $\times 10^{-6}$ Torr). Before deposition, the targets were pre-sputtered for 20 min, and then films were deposited for $\simeq$ 15 min at 400 °C. The samples were made with Cu (4N, AEM inc), CuLi (99:1 wt% AEM inc), and Cu:Li (99.99:0.01 wt% AEM inc) targets with varying powers on DC and RF to achieve different lithium content. A series of samples were deposited with varying oxygen flow for each batch to achieve optimal growth conditions and phase pure Cu_2O. The sum of oxygen and argon mass flow rate was fixed at 50 sccm. Table 1 contains detailed deposition parameters of the five phase-pure Cu_2O samples with varying Li content selected for further characterization.

Structural and compositional analysis was performed by a combination of XRD, SIMS, and RBS. XRD was performed on a Bruker AXS D8 Discover system, Cu Kα_1 radiation ($\lambda = 1.54$ Å) scanned over the angles 20° to 80° 2θ. SIMS measurements were done in a Cameca IMS7f microanalyzer with O_2^+ primary ions at 10 keV. RBS analysis was performed with 1.62 MeV $4He^+$ ions backscattered into a detector placed at 165° relative to the incident beam direction. Analysis of the RBS spectra was performed using simulation with the SIMNRA code [23]. Optical data were obtained from transmission measurements employed in the spectral range of 290-2500 nm with an integrating sphere on a Shimadzu SolidSpe-3700 DUV spectrophotometer. RTH was performed in a Lake-Shore 7604 setup in the Van-der Pauw configuration. Contacts were prepared by soldering Ag wires onto the samples' corners with indium (contact size, $d \simeq 1\,mm$).

3. Results and discussion

XRD patterns in Fig. 1 indicate that all films are crystalline and single-phase Cu_2O with no detectable peaks from CuO or Cu. All samples except #4 are dominated by the Cu_2O 111 reflection at 36.5°. In sample #4, both the 111 reflection and 200 reflection at 42.3° are similarly visible, indicating a less directional growth along the [111] direction. Cu_2O preferred growth orientation is sensitive to O_2 partial pressure and total pressure during deposition [24,25]. O_2 flow was adjusted for each sample to suit the target configuration and power applied for the different Li concentrations. The difference in the preferred orientation of sample #4 is likely due to the lower oxygen partial pressure during deposition. Measurement of clean fused silica substrate was performed to rule out background peaks, and these are marked by asterisk in Fig. 1. The crystallite size is estimated by the Scherrer's formula given by Dastan et al. [26], Dastan [27], Dastan et al. [28], Jafari et al. [29], Zhou et al. [30]:

Table 1
Deposition parameters during the growth of the Cu_2O films.

Sample	#1	#2	#3	#4	#5
Cu target	DC 100 W	-	DC 100W	DC 100W	-
Cu : Li target [99.99/0.01 wt%]	-	DC 100 W	-	-	-
Cu : Li target [99/1 wt %]	-	-	RF 10W	RF 50W	DC 100W
Argon flow [sccm]	40.5	41	44.7	45.5	44.5
Oxygen flow [sccm]	9.5	9.0	5.3	4.5	5.5
Temperature [°C]	400	400	400	400	400
Rotation [RPM]	12	12	12	12	12
Base pressure [1 × 10^{-4}Pa]	2.7	2.7	2.7	2.7	2.7
Deposition time [min]	15	15	15	15	15
Thickness [nm]	290	380	390	470	430

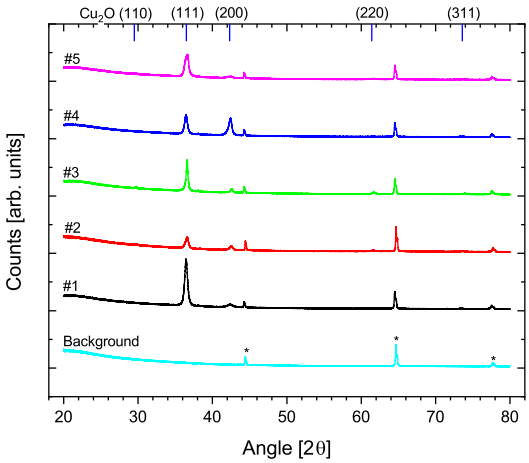

Fig. 1. $\theta - 2\theta$ XRD pattern of Cu_2O (#1) and $Cu_2O : Li$ films with increasing Li content (#2-5). Asterisk mark peaks stemming from the background scan.

$$D = \frac{K\lambda}{\beta Cos\theta} \tag{1}$$

where D is the crystallite size, K the Scherrer constant (0.94), $\lambda = 0.1543\,nm$ the X-ray wavelength, and θ the FWHM from a gaussian fit on the 111 peak in radians. D_p deduced from the 111 peak gives crystallite sizes of 30-50 nanometer for the different films without any apparent doping concentration trend. Slightly larger than the report of 14–20 nm crystallites in RF sputtered Cu_2O films by Gan et al. [8]. The crystallite size deduced from the Scherrer equation should be used cautiously with sputtered films. The equation is designed for spherical powder samples. Non-spherical shape of the crystallites, stress/strain, non-uniform crystallite sizes, and other peak broadening effects will impact the analysis.

Fig. 2 shows the measured optical transmission spectra for wavelengths from 290 to 2500 nm for the Cu_2O and $Cu_2O : Li$ films. The spectra show no apparent features emerging from Li doping, and high optical transmittance of 85-90 % is observed in all samples. High absorption is indicated by the clear decline towards zero transmittance for energies above the lowest allowed optical transitions at $\simeq$ 470 nm ($\Gamma_7^+ \rightarrow \Gamma_8^-$) [1,31]. The interference fringes indicate that sample #1 has a lower thickness than samples #2-5. SIMS measurements (Cu65 signal) confirms this, where sample #1 has a thickness of 290 nm compared to about 400-500 nm for sample #2-5. The study of Malerba et al. found that the absorption coefficient in Cu_2O includes various contributions from direct, forbidden, and indirect transitions, and therefore Tauc analysis is not a reliable way to determine the gap of Cu_2O samples [32]. However, Tauc analysis has been employed to investigate the effects of Li doping in Cu_2O (Fig. 3).The optical band gap was deduced through the relation [33–35]:

$$(h\nu\alpha)^{1/n} = A\left(h\nu - E_g\right) \tag{2}$$

where h is Planck's constant, f is the photon frequency, α the absorption coefficient, T the transmittance in %, and A a proportionality constant. In this work, we have used the exponent n equals 1/2 for direct allowed transitions. The deduced optical gaps are listed in Fig. 3, giving a mean optical gap of 2.55 ± 0.1 eV, and there is no significant change in the optical gap with Li doping.

Lithium concentration vs. depth profiles as measured by SIMS are shown in Fig. 4. Significant Li concentrations are detected in all the doped films (#2-5), while the undoped sample, #1, has Li concentration

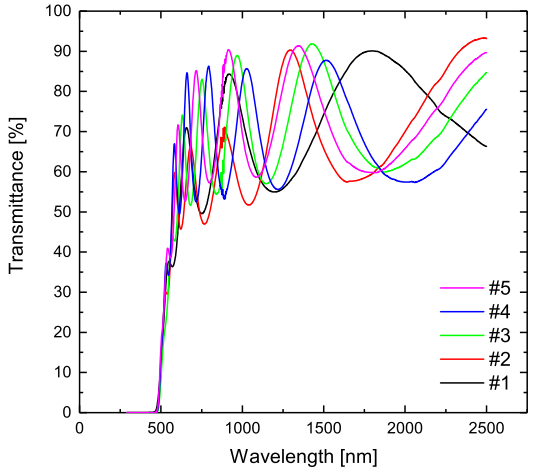

Fig. 2. Transmittance of Cu_2O (#1) and $Cu_2O:Li$ films with increasing Li content (#2-5).

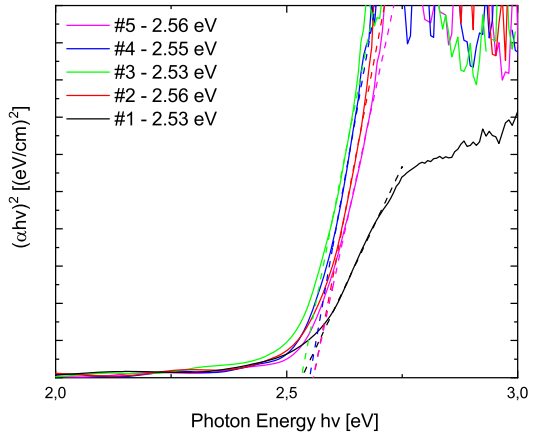

Fig. 3. Tauc plot of the Cu_2O (#1) and $Cu_2O:Li$ films (#2-5) deduced from the transmittance spectra in Fig. 2. The optical bandgap is extracted by extrapolation to the abscissa (dashed lines).

below the detection limit ($< 1 \times 10^{15}\,cm^{-3}$). Samples #2, 3 and 4 have uniform Li distribution throughout the film depth, with average concentrations of $1.9 \times 10^{18}\,cm^{-3}$, $7.0 \times 10^{18} cm^{-3}$, and $2.0 \times 10^{20}\,cm^{-3}$, respectively. It is important to note that in sample #5, there is a Li gradient towards the surface before averaging out at a mean concentration of $5 \times 10^{20}\,cm^{-3}$ after about 80 nm. Also, there is a drop in the copper signal (not shown) towards the surface, corresponding well to the Li-enriched region's depth.

It is believed that Li concentration in the near-surface region may be so high that stoichiometry of this layer is altered, and determination of the exact Li content in this layer may be challenging due to matrix effects. Supporting the SIMS results, the thin O-rich and Cu deficient surface layer formation is also confirmed by RBS results as illustrated by Fig. 5 showing RBS spectra of the undoped (#1) and Li-doped (#5) samples. It might be seen that for sample #5, the Cu edge is shifted towards the lower channels compared to the Cu surface position indicated by the arrow, and there is a small bump in O content (the channels

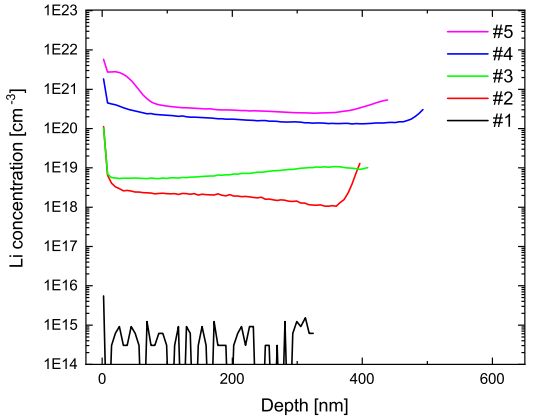

Fig. 4. SIMS depth profiles of the Cu_2O (#1) and $Cu_2O:Li$ films with increasing Li content (#2-5)., with Lithium concentration vs. depth.

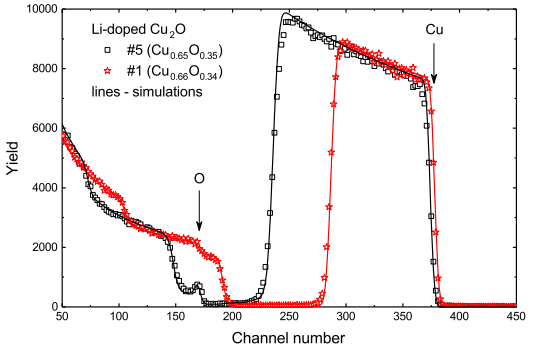

Fig. 5. RBS spectra of the undoped (#1) and Li-doped (#5) Cu_2O films. The surface positions of Cu and O atoms are shown by the arrows. The results of the simulations performed with the SIMNRA code are shown by the solid lines, while the films' obtained composition is plotted in the legend.

165-175). These observations may indicate a formation of a thin oxide layer at the film surface. According to simulations (see the solid line in the figure), the thickness of this layer is estimated to be $\simeq 25\,nm$. It should be noted that although the Li signal is not seen on the RBS spectra due to its low atomic mass, the involvement of Li atoms in this surface layer can not be excluded. According to simulations, the films have a near stoichiometric composition of $Cu_{0.66}O_{0.34}$ and $Cu_{0.65}O_{0.35}$ for samples #1 and #5, respectively. An electrical characterization by RTH measurements was conducted to determine carrier type, density, mobility, and sample resistivity (Fig. 6). The resistivity decreases by 3 orders of magnitude for the samples with high Li content. The decrease in resistivity can be attributed to an increase in acceptor concentration in the highly doped samples. A drop in carrier mobility accompanies this, however mobility above $10\,cm^2/Vs$ is retained in all samples.

The increase in carrier concentration correlates with a high Li concentration in the samples. The origin of the acceptor increase is not clear. Li is an isovalent dopant and not expected to increase the acceptor concentration directly but to passivate acceptor states originating from copper vacancies, i.e. $Li_i^+ + V_{cu}^- \rightarrow Li_{Cu}$, which would lead to a decrease in p-type doping. The high acceptor concentration and previous studies contradict the model where V_{Cu} is the primary defect responsible for the persistent p-type of Cu_2O [5,21,21,22]. One can speculate that

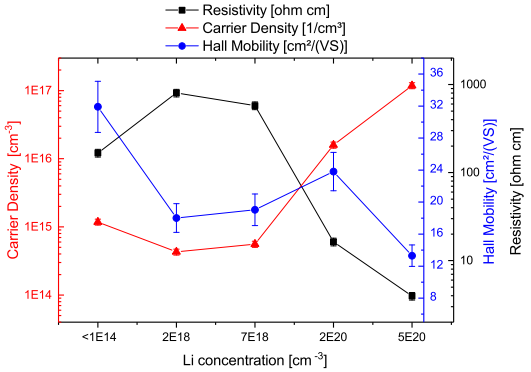

Fig. 6. Resistivity, majority carrier mobility, and carrier concentration as a function of measured lithium concentrations in the films.

hydrogen's role should be considered, similar to the explanations of persistent n-type in ZnO [36,37]. A possible explanation for the increase could be that Li passivates a compensating donor in Cu_2O. This would explain the increase in apparent carrier concentration at room temperature. Finally, one cannot rule out the formation of other unknown defects due to Li doping in Cu_2O.

4. Conclusion

Phase pure Li doped Cu_2O films have been deposited by reactive magnetron co-sputtering of Cu and Cu:Li doped targets. $Cu_2O:Li$ films with Li concentrations of $10^{18} - 10^{21}\ cm^{-3}$ retain their phase, relatively high mobility, and transparency in all investigated samples. However, a thin Cu lean and Li-rich surface layer is observed in the highest doped sample ($\simeq 1wt\%$ Li). The isovalent Li dopant was proposed to reduce acceptor concentration by passivating V_{Cu}. However, increased carrier density with increased Li doping concentrations is observed. The highest doped sample exhibits a high carrier concentration ($1.2 \times 10^{17}\ cm^{-3}$), low resistivity ($4\,\Omega cm$), and mobility of $13\ cm^2/Vs$.

Declaration of Competing Interest

The authors declare that they have no known competing financial interests or personal relationships that could have appeared to influence the work reported in this paper.

Acknowledgments

This work was performed within The Norwegian Research Center for Sustainable Solar Cell Technology (FME SUSOLTECH, project number 257639/E20). The center is co-sponsored by the Research Council of Norway and its research and industry partners. The Research Council of Norway is acknowledged for the support to the Norwegian Micro- and Nano-Fabrication Facility, NorFab, project number 295864.

References

[1] B.K. Meyer, A. Polity, D. Reppin, M. Becker, P. Hering, B. Kramm, P.J. Klar, T. Sander, C. Reindl, C. Heiliger, M. Heinemann, C. Müller, C. Ronning, The physics of copper oxide Cu_2O, in: B.G. Svensson, S.J. Pearton, C. Jagadish (Eds.), Semiconductors and Semimetals vol. 88, Academic Press, 2013, pp. 201–226, https://doi.org/10.1016/B978-0-12-396489-2.00006-0.

[2] W. Shockley, H.J. Queisser, Detailed Balance Limit of Efficiency of p-n Junction Solar Cells, J. Appl. Phys. 32 (3) (1961) 510–519, https://doi.org/10.1063/1.1736034.

[3] T. Minami, Y. Nishi, T. Miyata, Efficiency enhancement using a Zn_{1-x} Ge_x-O thin film as an n-type window layer in Cu_2O-based heterojunction solar cells, Appl. Phys. Express 9 (5) (2016) 052301, https://doi.org/10.7567/APEX.9.052301.

[4] A.D. Vos, Detailed balance limit of the efficiency of tandem solar cells, J. Phys. D. 13 (5) (1980) 839–846, https://doi.org/10.1088/0022-3727/13/5/018.

[5] T.G. Kim, H. Ryu, W.-J. Lee, Effects of lithium (Li) on lithium-cuprous-oxide (Li-Cu_2O) composite films grown by using electrochemical deposition for a PEC photoelectrode, J. Korean Phys. Soc. 68 (2) (2016) 268–273, https://doi.org/10.3938/jkps.68.268.

[6] D.S. Darvish, H.A. Atwater, Epitaxial growth of Cu_2O and ZnO/Cu_2O thin films on MgO by plasma-assisted molecular beam epitaxy, J. Cryst. Growth 319 (1) (2011) 39–43, https://doi.org/10.1016/j.jcrysgro.2011.01.071.

[7] J.R. Avila, A.W. Peters, Z. Li, M.A. Ortuño, A.B.F. Martinson, C.J. Cramer, J. T. Hupp, O.K. Farha, Atomic layer deposition of Cu(i) oxide films using Cu(ii) bis (dimethylamino-2-propoxide) and water, Dalton Trans. 46 (2017) 5790–5795, https://doi.org/10.1039/C6DT02572B.

[8] J. Gan, V. Venkatachalapathy, B. Svensson, E. Monakhov, Influence of target power on properties of Cu_xO thin films prepared by reactive radio frequency magnetron sputtering, Thin Solid Films 594 (2015) 250–255, https://doi.org/10.1016/j.tsf.2015.05.029.

[9] A. Jafari, K. Tahani, S. Asgary, Z. Shi, X.-T. Yin, W.-D. Zhou, H. Garmestani, Ş Ţălu, Ion implantation of copper oxide thin films; statistical and experimental results, Surf. Interfaces 18 (2020) 100463, https://doi.org/10.1016/j.surfin.2020.100463.

[10] T.K.S. Wong, S. Zhuk, S. Masudy-Panah, G.K. Dalapati, Current status and future prospects of copper oxide heterojunction solar cells, Materials 9 (4) (2016) 271, https://doi.org/10.3390/ma9040271.

[11] W.H. Brattain, The copper oxide rectifier, Rev. Mod. Phys. 23 (3) (1951) 203–212, https://doi.org/10.1103/RevModPhys.23.203.

[12] J. Xue, R. Dieckmann, The non-stoichiometry and the point defect structure of cuprous oxide ($Cu_{2-\delta}O$), J. Phys. Chem. Solids 51 (11) (1990) 1263–1275, https://doi.org/10.1016/0022-3697(90)90003-X.

[13] O. Porat, I. Riess, Defect chemistry of $Cu_{2-y}O$ at elevated temperatures. Part II: electrical conductivity, thermoelectric power and charged point defects, Solid State Ionics 81 (1) (1995) 29–41, https://doi.org/10.1016/0167-2738(95)00169-7.

[14] A.F. Wright, J.S. Nelson, Theory of the copper vacancy in cuprous oxide, J. Appl. Phys. 92 (10) (2002) 5849–5851, https://doi.org/10.1063/1.1516620.

[15] G.K. Paul, Y. Nawa, H. Sato, T. Sakurai, K. Akimoto, Defects in Cu_2O studied by deep level transient spectroscopy, Appl. Phys. Lett. 88 (14) (2006) 141901, https://doi.org/10.1063/1.2175492.

[16] M. Nolan, S.D. Elliott, The p-type conduction mechanism in Cu_2O: a first principles study, Phys. Chem. Chem. Phys. 8 (45) (2006) 5350–5358, https://doi.org/10.1039/B611969G.

[17] D.O. Scanlon, B.J. Morgan, G.W. Watson, A. Walsh, Acceptor levels in p-type Cu_2O: rationalizing theory and experiment, Phys. Rev. Lett. 103 (9) (2009) 1–4, https://doi.org/10.1103/PhysRevLett.103.096405.

[18] L.Y. Isseroff, E.A. Carter, Electronic structure of pure and doped cuprous oxide with copper vacancies: suppression of trap states, Chem. Mater. 25 (3) (2013) 253–265, https://doi.org/10.1021/cm3040278.

[19] F. Biccari. Defects and doping in Cu_2O, University of Rome, 2009. Doctoral dissertation.

[20] Y.S. Lee, J. Heo, M.T. Winkler, S.C. Siah, S.B. Kim, R.G. Gordon, T. Buonassisi, Nitrogen-doped cuprous oxide as a p-type hole-transporting layer in thin-film solar cells, J. Mater. Chem. A 1 (2013) 15416–15422, https://doi.org/10.1039/C3TA13208K.

[21] K.-S. Cho, D.-H. Kim, Y.-H. Kim, J. Nah, H.-K. Kim, Li-doped Cu_2O/ZnO heterojunction for flexible and semi-transparent piezoelectric nanogenerators, Ceram. Int. 43 (2) (2017) 2279–2287, https://doi.org/10.1016/j.ceramint.2016.10.208.

[22] K. Karlsen. Characterization of Li doped, magnetron sputtered Cu_2O thin films, University of Oslo, 2019. Masters thesis.

[23] M. Mayer, Improved physics in SIMNRA 7, Nucl. Instrum. Methods Phys. Res. Section B 332 (2014) 176–180, https://doi.org/10.1016/j.nimb.2014.02.056.

[24] K. Bergum, H.N. Riise, S.M. Gorantla, E. Monakhov, B.G. Svensson, Thin film Cu_2O for solar cell applications. 2016 IEEE 43rd Photovoltaic Specialists Conference (PVSC), 2016, pp. 2770–2773, https://doi.org/10.1109/PVSC.2016.7750156.

[25] Y. Wang, J. Ghanbaja, F. Soldera, P. Boulet, D. Horwat, F. Mücklich, J. Pierson, Controlling the preferred orientation in sputter-deposited Cu_2O thin films: influence of the initial growth stage and homoepitaxial growth mechanism, Acta Mater. 76 (2014) 207–212, https://doi.org/10.1016/j.actamat.2014.05.008.

[26] D. Dastan, P. Londhe, N. Chaure, Characterization of TiO_2 nanoparticles prepared using different surfactants by solgel method, Journal of Materials Science: Materials in Electronics 25 (2014) 3473–3479, https://doi.org/10.1007/s10854-014-2041-9.

[27] D. Dastan, Effect of preparation methods on the properties of titania nanoparticles solvothermal versus sol-gel, Appl. Phys. A 123 (2017) 699, https://doi.org/10.1007/s00339-017-1309-3.

[28] D. Dastan, N. Chaure, M. Kartha, Surfactants assisted solvothermal derived titania nanoparticles: synthesis and simulation, J Mater Sci 28 (2017) 7784–7796, https://doi.org/10.1007/s10854-017-6474-9.

[29] A. Jafari, M. Alam, S. Ziakhodadadian, Z. Shi, H. Garmestani, A. Weidenbach, Ş Ţălu, Statistical, morphological, and corrosion behavior of PECVD derived cobalt oxide thin films, J. Mater. Sci. 30 (2019) 21185–21198, https://doi.org/10.1007/s10854-019-02492-6.

[30] W.-D. Zhou, D. Dastan, J. Li, X.-T. Yin, Q. Wang, Discriminable sensing response behavior to homogeneous gases based on n-ZnO/p-NiO composites, Nanomaterials 10 (4) (2020) 785, https://doi.org/10.3390/nano10040785.

[31] K. Bergum, H.N. Riise, S. Gorantla, P.F. Lindberg, I.J.T. Jensen, A.E. Gunnæs, A. Galeckas, S. Diplas, B.G. Svensson, E. Monakhov, Improving carrier transport in

Cu_2O thin films by rapid thermal annealing, J. Phys 30 (7) (2018) 075702, https://doi.org/10.1088/1361-648x/aaa5f4.
[32] C. Malerba, F. Biccari, C. Leonor Azanza Ricardo, M. D'Incau, P. Scardi, A. Mittiga, Absorption coefficient of bulk and thin film Cu_2O, Solar Energy Mater. Solar Cells 95 (10) (2011) 2848–2854, https://doi.org/10.1016/j.solmat.2011.05.047.
[33] D. Dastan, Nanostructured anatase titania thin films prepared by sol-gel dip coating technique, J. At. Mol. Condens. MatterNano Phys. 2 (2) (2015) 109–114.
[34] D. Dastan, S. Panahi, N. Chaure, Characterization of titania thin films grown by dip-coating technique, J. Mater. Sci. 27 (2016) 12291–12296, https://doi.org/10.1007/s10854-016-4985-4.
[35] R. Shakoury, A. Arman, Ş Ţălu, D. Dastan, C. Luna, S. Rezaee, Stereometric analysis of TiO_2 thin films deposited by electron beam ion assisted, Opt. Quantum Electron. 52 (5) (2020) 270, https://doi.org/10.1007/s11082-020-02388-4.
[36] C. Van de Walle, Hydrogen as a cause of doping in zinc oxide, Phys. Rev. Lett. 85 (5) (2000) 1012–1015, https://doi.org/10.1103/PhysRevLett.85.1012.
[37] U. Ozgur, Y. Alivov, C. Liu, A. Teke, M. Reshchikov, S. Dogan, V. Avrutin, S. x, H. Morkoc, A comprehensive review of ZnO materials and devices, J. Appl. Phys. 98 (4) (2005), https://doi.org/10.1063/1.1992666.

Paper III

Dominant Acceptors in Li Doped, Magnetron Deposited Cu_2O Films

Martin Nyborg, Kjetil Karlsen, Kristin Bergum, Eduard Monakhov

This paper is published in Material Research Express **8** (2021)

III

PAPER • **OPEN ACCESS**

Dominant acceptors in Li doped, magnetron deposited Cu_2O films

To cite this article: M Nyborg *et al* 2021 *Mater. Res. Express* **8** 125903

Materials Research Express

PAPER

Dominant acceptors in Li doped, magnetron deposited Cu_2O films

M Nyborg* , K Karlsen , K Bergum and E Monakhov*

Physics Department/Centre for Materials Science and Nanotechnology, University of Oslo, PO Box 1048 Blindern, Oslo N-0316, Norway

* Authors to whom any correspondence should be addressed.

E-mail: martin.nyborg@fys.uio.no **and** eduard.monakhov@fys.uio.no

Keywords: cuprous oxide, doping, lithium, carrier transport, magnetron sputtering

OPEN ACCESS

RECEIVED
14 October 2021

REVISED
18 November 2021

ACCEPTED FOR PUBLICATION
29 November 2021

PUBLISHED
17 December 2021

Abstract

Cu_2O films deposited by reactive magnetron sputtering with varying Li concentrations have been investigated by a combination of temperature-dependent Hall effect measurement and thermal admittance spectroscopy. As measured by secondary ion mass spectrometry, Li concentrations up to 5×10^{20} Li/cm^3 have been achieved. Li doping significantly alters the electrical properties of Cu_2O and increases hole concentration at room temperature for higher Li concentrations. Moreover, the apparent activation energy for the dominant acceptors decreases from around 0.2 eV for undoped or lightly doped Cu_2O down to as low as 0.05 eV for higher Li concentrations.

1. Introduction

Cuprous oxide (Cu_2O) is an attractive p-type semiconductor widely investigated for its possible application in photovoltaics. It has intriguing properties suitable for both single- and tandem-junction solar cells. Cu_2O has a direct bandgap of 2.17 eV, is non-toxic, has high natural abundance, and has the potential for low-cost production schemes. The Shockley–Queisser limit is about 20% for a single junction and could reach over 30% in a tandem junction configuration [1–3]. Thick oxidized copper sheets have had steep progress in the past years, achieving efficiencies as high as 8% [4]. However, thin-film devices have demonstrated considerably lower performance [5, 6]. Among the possible reasons for the low efficiencies of the solar cells based on Cu_2O, one can point to a lack of control over the carrier concentration and the inability to synthesize n-type Cu_2O that would enable a p-n homojunction [7–9].

Thin-film Cu_2O cells suffers from poor carrier collection, especially at higher wavelengths, which could be attributed to the relative low mobility and recombination at the interface and within the Cu_2O layer [9, 10] Brandt *et al* [11] suggests that thermal and chemical treatments will be needed to reduce or passivate defects in order to improve cell performance of Cu_2O devices. The persistent p-type nature of Cu_2O is believed to be due to the acceptor states of copper vacancies (V_{Cu}), which is substantiated by the studies of their configurations and electronic properties by density functional theory (DFT) [12]. Thus, the control over carrier concentration should involve the ability to control the V_{Cu} concentration or to passivate V_{Cu}.

Perhaps, the most prominent candidates for passivating V_{Cu} and potential n-type doping are Group-I elements. For example, hydrogen atoms are predicted to form stable complexes with V_{Cu} (H–V_{Cu}) [13]. Although H–V_{Cu} is still an acceptor, the acceptor level has an activation energy of around 1.2 eV, which effectively reduces the acceptor activity of V_{Cu}. Isolated hydrogen atoms are predicted to occupy an interstitial position (H_i). The donor level of H_i is expected to lie deep in the bandgap, at around $E_V + 1$ eV, where E_V is the valence band edge. Introducing atomic hydrogen can, thus, moderate the hole concentration in Cu_2O.

Similar to hydrogen, alkali metals, such as Li and Na, can also be considered for carrier concentration control. Theoretical predictions on the electronic activity of these metals are, however, scarce. *Isseroff and Carter* [14] have performed DFT calculations on the interaction of several metals, such as Li, Mg, Mn, and Za, with V_{Cu} and electronic properties of their complexes. It is established that the complex of Li and V_{Cu} (Li–V_{Cu}) has no electronic levels in the bandgap. Moreover, Li–V_{Cu} has the lowest formation energy among the complexes considered in the study. It has been concluded that Li has the greatest potential to passivate V_{Cu} and to improve the electronic properties of Cu_2O.

Table 1. Li concentration and film thickness in the prepared samples deduced from SIMS measurements.

Sample #	Li concentration (cm^{-3})	Film thickness (nm)
1 (undoped)	$<10^{15}$	470
2	2×10^{18}	485
3	7×10^{18}	550
4	2×10^{20}	560
5	5×10^{20}	530

Perhaps, the first systematic study of the effect of alkali metal on conductivity and carrier concentration in Cu_2O has been performed by Minami *et al* [15] for Na. In that study, Cu_2O was prepared by oxidizing metallic Cu sheets, and Na was introduced by in-diffusion from the surface. It has been observed that conductivity and carrier concentration increases with the duration and the temperature of the Na in-diffusion. For instance, the carrier concentration at room temperature has increased from 10^{13} cm^{-3} (for undoped Cu_2O) to 10^{19} cm^{-3} (after the longest Na in-diffusion). Moreover, Temperature-dependent Hall effect (TDH) measurements have revealed a decrease in the activation energy of the acceptors: from 0.15 eV (for undoped Cu_2O) down to 0.02 eV (for Cu_2O with hole concentration of 4×10^{17} cm^{-3} at room temperature). The samples with the longest Na in-diffusion exhibited degenerated p-type conduction. This is a surprising result since Na, similar to Li, is expected to passivate V_{Cu} and reduce hole concentration. The observed increase in hole concentration was attributed to an excess formation of V_{Cu} compensating for Na atoms incorporated at the interstitial site as donors [15]. Such an interpretation, however, cannot explain the decrease in the acceptor activation energy, since the acceptor activation energy of V_{Cu} is believed to be ~0.2 eV [12].

Recently, it has been reported on the effect of Li on resistivity and carrier concentration in magnetron sputter deposited Cu_2O films [16]. It is observed a trend similar to that reported by Minami *et al* [15] for Na: the hole concentration increases for higher Li content. The undoped Cu_2O films exhibit a hole concentration of 10^{15} cm^{-3}, while those doped with Li demonstrate a hole concentration of up to 10^{17} cm^{-3} at room temperature.

In this study, we report on the electronic properties of the dominant acceptors in Li doped, magnetron sputter deposited Cu_2O films. For the first time temperature dependence of hole concentration and the activation energy of the dominant acceptors are deduced using TDH measurements and thermal admittance spectroscopy (TAS) on Li doped Cu_2O.

2. Experimental

500 nm thick Cu_2O films with various Li content were deposited by reactive DC and RF magnetron co-sputtering from Cu (4N, AEM Inc.) and Cu:Li targets (4N 99:1 wt% AEM Inc. and 4N 99.99:0.01 wt% AEM Inc.) in a Semicore Triaxis system. Two 1×1 cm^2 substrates were used in each deposition run: (i) an UV-grade fused silica substrate with a resistivity of >1 GOhm-cm for TDH measurements and (ii) a n-type Si substrate for TAS. The Si substrates were cut from an n-type (100) Si wafer with a resistivity of 5 Ohm-cm. The n-type Si was chosen in order to form a p-n heterojunction between Cu_2O and Si. The fused silica substrates were cleaned for 1 min in Pirhana solution, rinsed in DI water, then subsequently ultrasonically washed for 5 min in isopropanol before deposition. The Si substrates was prepared following the RCA procedure. Chamber base pressure was lowered to below 2.7×10^{-4} PA, subsequently the targets were pre sputtered for 20 min before initiating deposition for 15 min at 400 °C. A total of 10 samples were prepared after 5 depositions for different Li content. Additional details on deposition and characterization of Li doped Cu_2O is reported elsewhere [16].

Secondary ion mass spectrometry (SIMS) was used to measure Li concentration in the films. Table 1 shows the Li concentration and film thickness in the samples studied.

Charge carrier density has been assessed by TDH measurements with a Lakeshore 7604 setup in the temperature range 95–550 K, employing a field strength of ±1 T. Two separate cryostats were used for the TDH measurements: (1) a low-temperature one in the rage 95–300 K and (2) a high-temperature one in the range 300–550 K. The measurements were performed in the Van der Pauw geometry.

Diodes for TAS measurements were defined on the samples with the Si substrates by a lift-off lithography process, which involved (i) deposition of 400 nm thick Au front contacts with a diameter of 1.5 mm on the Cu_2O film and (ii) subsequent etching of Cu_2O around the Au contacts. Al was deposited as a back contact, resulting in Au/Li:Cu_2O/n-Si/Al structures. Current-voltage measurements confirmed a diode behavior of the structures with a rectification of 2–6 orders of magnitude. TAS was performed with an Agilent 4280A LCR meter under a reverse bias of −1 V, using a probing ac signal with frequencies between 1 kHz to 1 MHz and an amplitude of 20 mV.

101

Table 2. Some of the main parameters for the Cu_2O film used in the simulation.

Parameter	Value	References
Band gap [eV]	2.17	[12]
Relative permittivity [eV]	7.11	[12]
Electron affinity [eV]	3.1	[12]
Film thickness [nm]	550	table 1, sample #3
Acceptor concentration [cm^{-3}]	1×10^{18}	figure 1(a), sample #3
Acceptor activation energy [eV]	0.14	figure 3, sample #3

Device simulation of the pn-junction was performed using Silvaco TCAD device simulator. The device structure and parameters were chosen to corroborate with the experimental data, the Si substrate was defined with a n-type doping concentration of 10^{15} cm^{-3}. See table 2 for the main material parameters used in the simulation.

3. Results and discussion

3.1. Temperature-dependent hall effect

Hall effect measurements, performed for the Cu_2O films deposited on the quartz substrates, from the polarity of the Hall voltage it is revealed p-type conductivity in all the samples [17]. At room temperature, the hole concentration in the films is in the range 10^{15}–10^{17} cm^{-3}. The results of the TDH measurements for samples #1-#5 are presented in figure 1. As mentioned above, two separate cryostats were used for temperature ranges 95–300 K and 300–550 K. This can be seen in figure 1(b) as a discontinuity in the temperature dependence for hole mobility at 300 K. Almost no discontinuity between the two cryostats is observed for the hole concentration in figure 1(a).

The hole concentrations (figure 1(a)) show a strong dependence on temperature. For instance, in the undoped film (sample #1) the hole concentration changes from 10^{13} cm^{-3} at around 200 K up to 10^{18} cm^{-3} at 550 K. The temperature-dependent hole concentration for a p-type semiconductor can be described by the following relation [17]:

$$p(\mathrm{T}) \gg \frac{g_a N_v (N_a - N_d)}{N_d} \exp\left(-\frac{\Delta E_a}{kT}\right) \quad (1)$$

where $p(T)$ is the hole concentration, N_a is the acceptor concentration, N_d is the net concentration of the compensating donors, E_a is the activation energy of the acceptor, N_v is the valence band effective density of states, g_a is the degeneracy factor, k is Boltzmann constant, and T is temperature. One can observe that $p(T)$ for sample #1 in figure 1(a) deviates from the simple exponential dependence in equation (1). In the experimental results, the slope of $p(T)$ increases with increasing T. We interpret this as an indication of several acceptor levels in the film, where deeper acceptors become activated at higher T. Nevertheless, we have estimated the activation energy of the most shallow acceptor by fitting equation (1) in the temperature range 200–300 K. The estimated activation energy is ~0.16 eV, as indicated in parentheses in figure 1(a).

Doping with Li results in a noticeable effect on the electronic properties of Cu_2O (figure 1(a)). Samples #2 (2×10^{18} Li/cm^3) and #3 (7×10^{18} Li/cm^3) exhibit somewhat lower hole concentrations as compared to sample #1 (undoped). Moreover, the acceptor activation energies appear to increase with Li doping to values of ~0.25 eV and ~0.22 eV for samples #2 and #3, respectively. This observation is consistent with theoretical results by *Isseroff and Carter* [14], where Li is predicted to passivate V_{Cu}. Similar to the undoped sample #1, an indication of deeper acceptors can be seen in $p(T)$, which is manifested by steeper slopes of p(T) at higher T. At 550 K, $p(T)$ appears to stabilize at around 10^{18} cm^{-3}.

For higher Li concentrations, however, the effect of Li doping is different. Firstly, the hole concentration at room temperature increases significantly: to around 10^{16} cm^{-3} for sample #4 and to around 10^{17} cm^{-3} for sample #5. At 550 K, the hole concentration appears to saturate at around 10^{18}–10^{19} cm^{-3}. Secondly, the activation energy for the dominating shallow acceptors decreases to 0.12 eV and 0.05 eV for samples #4 and #5, respectively. This observation contradicts the predictions by *Isseroff and Carter* [14] and the trend observed for the lower Li concentration (samples #2 and #3). However, this is in line with the finding by Minami *et al* [15], who observed an increase in the hole concentration and a decrease in the activation energy after Na doping. Since the Li concentration in samples #4 and #5 is relatively high (2×10^{20} Li/cm^3 and 5×10^{20} Li/cm^3), one can speculate that Li with such a high concentration can change the material properties of Cu_2O and thus affect

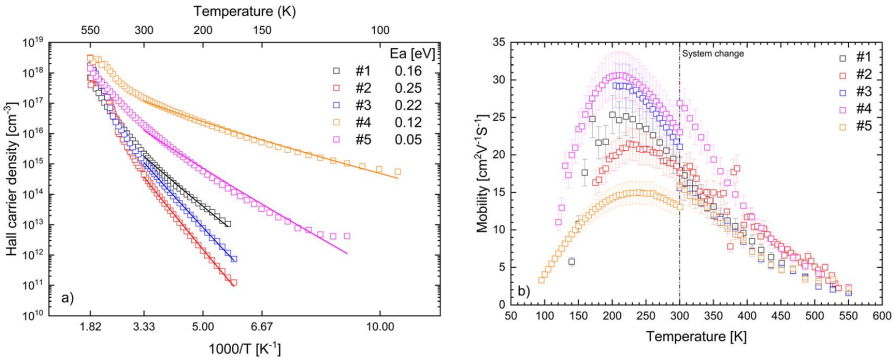

Figure 1. (a) Hole concentration versus inverse temperature in different samples. The solid lines indicate approximate fittings of the activation energies. The estimates of the activation energies are given in the parentheses. (b) Carrier mobility versus temperature in different samples.

the formation energy of defects, including that of V_{Cu}. According to the widely accepted formalism, the equilibrium concentration of a defect in a crystal is defined by the formation energy of the defect [18]. A decrease in the formation energy would lead to an increase in the concentration of V_{Cu} and would affect the acceptor level position in the band gap. In the study by Minami *et al* [15], the concentration of Na in Cu_2O has not been reported. One can speculate, however, that Na concentration could be high, and similar consideration can be applied to the effect of Na.

The temperature dependent mobility data in figure 1(b) show a typical bell-shape temperature dependency. This is generally attributed to the contribution of ionized impurity scattering at low temperatures and intrinsic scattering at elevated temperatures (i.e. phonon scattering) [12]. The mobility is relatively low compared to that reported for single crystal samples (80–100 $cm^2V^{-1}s^{-1}$) [19], this could be attributed to an increase of neutral impurity scattering and grain boundary scattering in polycrystalline thin films.

It has not been observed any dependence in the band gap on the film thickness in Li doped Cu_2O [16]. Similarly, no such dependence is observed for the doping concentration. We can conclude that the observed changes in the electronic properties are due to Li doping and are not caused by different film thickness.

3.2. Thermal admittance spectroscopy

TAS measurements have been employed to substantiate the characterization of electrically active defects in the deposited films. As mentioned above, for TAS measurements the Cu_2O films are deposited on n-type Si substrates with a doping concentration of 1×10^{15} cm^{-3}. The structure forms a p-n heterojunction that shows a diode behavior and the corresponding capacitance of the diode. Figure 2 shows the results of TAS for samples #1–#5, where the capacitance (C) and the conductance over the angular frequency (G/ω) are measured at a reverse bias of −1 V and plotted versus temperature for 6 probing frequencies. As established from TDH measurements (figure 1), the acceptors in the Cu_2O films are partially activated at room temperature, which results in a carrier concentration in the range 10^{14}–10^{17} cm^{-3} (depending on the sample). The total capacitance of the sample is then determined by depletion regions in the film and in the substrate. The value of the total capacitance at room temperature is around 120–150 pF (figure 2, left). As the temperature decreases, the acceptors freeze out and the hole concentration in the Cu_2O film decreases rapidly, as seen in TDH measurements in figure 1(a). In TAS, the freeze-out of the acceptors in the film is manifested as a step-like drop of the capacitance (figure 2, left). In the conductance measurements (figure 2, right), the acceptors freeze-out corresponds to a maximum.

The activation energy of the acceptors can be deduced by performing capacitance and conductance measurements at different probing frequencies. The temperature of the step-like capacitance drop or the conductance maximum depends on the frequency [17]. From the TAS plots (figure 2), a single dominating acceptor freeze-out is observed in samples #1 - #4. By performing a standard Arrhenius analysis (figure 3), the deduced acceptor energies are 0.11 eV, 0.11 eV, 0.14 eV and 0.08 eV for sample #1, #2, #3 and #4, respectively. In sample #5, no clear acceptor freeze-out is visible within the investigated temperature range, which indicates very low activation energy for the acceptors. This is, in fact, consistent with the observation by TDH, where the activation energy for sample #5 (figure 1) is deduced to be as low as 0.05 eV.

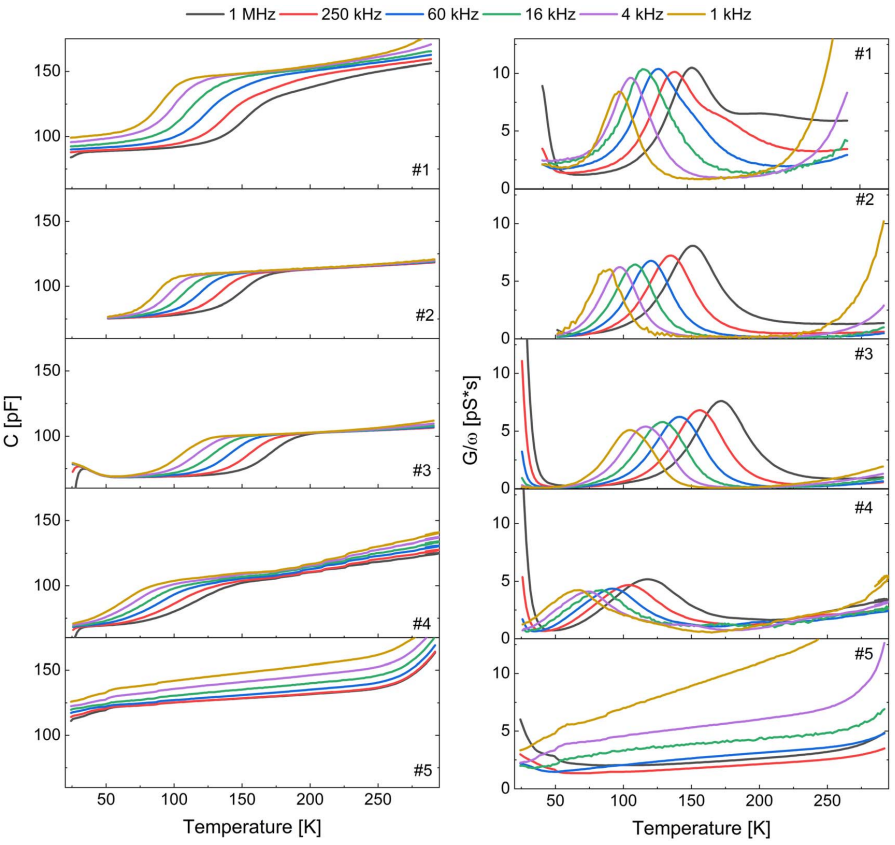

Figure 2. Capacitance (C, left) and conductance over angular frequency (G/ω, right) versus temperature for different probing frequencies for samples #1 – #5.

One can see that the activation energies deduced by TAS are systematically lower compared to those deduced by TDH. The reason can be twofold: (1) One can observe that p(T) deviates from perfect exponential dependence in figure 1(a), which introduces uncertainty in the activation energy deduced from the TDH measurements. (2) The Poole-Frenkel effect [20], which lowers the activation energy in external electric fields, can play an important role in the TAS measurements. Indeed, in the TDH measurements, the voltage spans over about 1 cm, resulting in a weak electric field. In the TAS measurements, most of the voltage drop occurs at the p-n heterojunction, which results in a higher electric field in the probing region. In any case, it is clear, however, that the trend for the decreasing activation energy at high Li concentration is similar: the activation energies in samples #4 and #5 are consistently lower compared to other samples.

3.3. TAS simulations

In order to corroborate and substantiate the interpretation of the TAS measurements, we have performed simulations using Silvaco TCAD [21]. Figure 4 shows the simulated capacitance (C) and conductance over the angular frequency (G/ω) as functions of temperature for different frequencies that were used in the experiment (figure 2). The parameters were chosen to illustrate the simulations correspond to those for sample #3, since it represents an intermediate case. Simulations with different parameters, such as film thickness, acceptor activation energy, and acceptor concentration, have been carried out and demonstrated the same trends as in the experiment.

At 270 K, the simulation shows the presence of a depletion region associated with the p-n heterojunction between p-type Cu_2O and n-type Si. Moreover, since the concentration of acceptors in Cu_2O (10^{18} cm^{-3}) is much higher compared to donor concentration in Si (10^{15} cm^{-3}), the depletion region is extended predominantly into Si. This is in full agreement with the theory on the depletion region in p-n junctions [17].

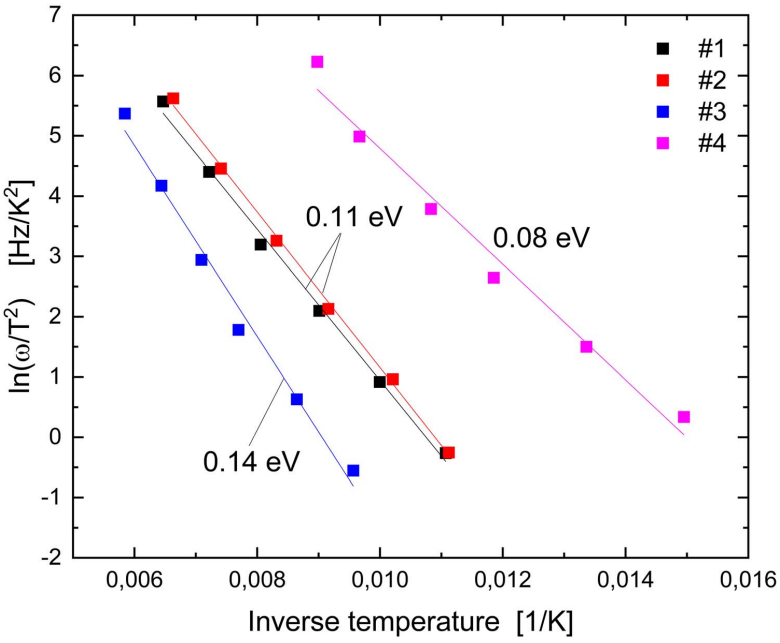

Figure 3. Arrhenius plot for TAS measurements of samples #1 - #4. The solid lines represent the linear fits. The deduced activation energies are indicated.

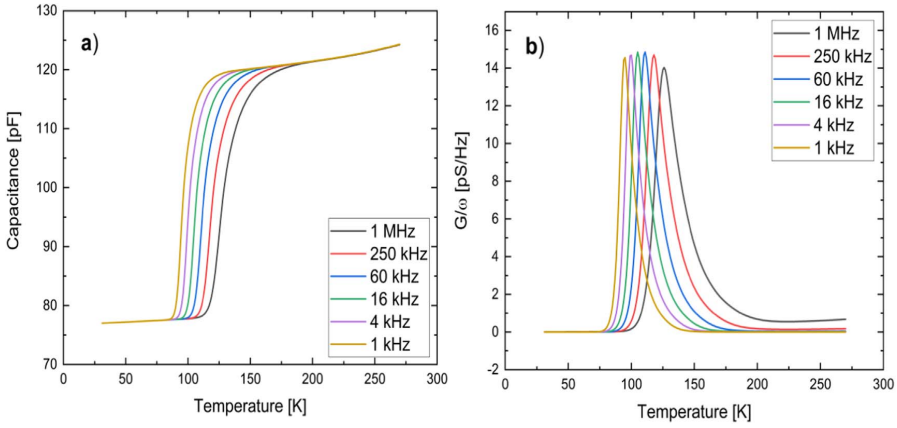

Figure 4. Capacitance (a) and conductance over angular frequency (b) simulated as functions of temperature for the 6 probing frequencies used in the experiment (1 kHz–1 MHz). The simulations are performed using the parameters in table 2.

Thus, at around room temperature, the capacitance of the structure is determined mainly by the depletion region in Si, which corresponds to around ~120 pF for the given diode size.

As temperature decreases, the acceptors in the Cu_2O films start to freeze out, which is manifested in the capacitance drop in the TAS measurements. At low temperatures, when the acceptors are completely frozen out, the Cu_2O film becomes a fully depleted dielectric. The total capacitance of the structure is then determined mainly by the capacitance of the depleted film, which corresponds to around ~80 pF for the given film thickness (table 2) and the diode size. The simulation supports, hence, the interpretation that the capacitance drop and the conductance peak in the TAS measurements correspond to the freeze-out of the dominant acceptors in the Cu_2O film.

105

4. Conclusion

We have performed Hall effect and TAS investigations of the effect of Li doping on the dominant acceptors in Cu_2O films deposited by reactive DC and RF magnetron sputtering from a metallic Cu target. During the growth, the films were doped with Li by co-sputtering of Cu:Li targets. Li concentrations up to 5×10^{20} Li/cm^3 have been achieved. We observe an increase in hole concentration at room temperature for higher Li concentrations. This can be considered as a counter-intuitive finding since Li is expected to passivate V_{Cu} that is commonly believed to be the main acceptor in Cu_2O. Moreover, the apparent activation energy for the dominant acceptors decreases from around 0.2 eV down to 0.05 eV for higher Li concentrations, as determined by TDH. Our results are, however, in line with literature reports on the effect of other group-I doping: Na.

Acknowledgments

This work was performed within The Norwegian Research Center for Sustainable Solar Cell Technology (FME SUSOLTECH, project number 257639/E20). The center is co-sponsored by the Research Council of Norway and its research and industry partners. The Research Council of Norway is acknowledged for the support to the Norwegian Micro- and Nano-Fabrication Facility, NorFab, project number 295864.

Data availability statement

The data that support the findings of this study are available upon reasonable request from the authors.

ORCID iDs

M Nyborg https://orcid.org/0000-0002-2787-9073
K Karlsen https://orcid.org/0000-0002-0904-2480
K Bergum https://orcid.org/0000-0002-4093-521X
E Monakhov https://orcid.org/0000-0002-7015-3358

References

[1] de Vos A 1980 *J. Phys. D: Appl. Phys.* **13** 839
[2] White T P, Lal N N and Catchpole K R 2014 *IEEE J. Photovolt.* **4** 208
[3] Mitroi M R, Ninulescu V and Fara L 2017 *Int. J. Photoenergy* **2017** 7284367
[4] Minami T, Nishi Y and Miyata T 2016 *Applied Physics Express* **9** 052301
[5] Wong T K S, Zhuk S, Masudy-Panah S and Dalapati G K 2016 *Materials* **9** 271
[6] Wang Y and Pierson J F 2021 *J. Phys. D: Appl. Phys.* **54** 263002
[7] Gan J, Hoye R L Z, Ievskaya Y, Vines L, Marin A T, MacManus-Driscoll J L and Monakhov E V 2020 *Sol. Energy Mater. Sol. Cells* **209** 110418
[8] Brandt R E, Young M, Park H H, Dameron A, Chua D, Lee Y S, Teeter G, Gordon R G and Buonassisi T 2014 *Appl. Phys. Lett.* **105** 263901
[9] Rizi M T, Abadi M H S and Ghaneii M 2018 *Optik* **155** 121
[10] Lee Y S, Chua D, Brandt R E, Siah S C, Li J V, Mailoa J P, Lee S W, Gordon R G and Buonassisi T 2014 *Adv. Mater.* **26** 4704–10
[11] Brandt R E, Lloyd M, Lee Y S, Siah S C and Buonassisi T 2013 *IEEE 39th Photovoltaic Specialists Conference (PVSC)* 846–8
[12] Meyer B *et al* 2013 The Physics of Copper Oxide (Cu2O) *Oxide Semiconductors* ed B G Svensson, S J Pearton and C Jagadish 88 (Amsterdam: Elsevier) 6 201 Semiconductors and Semimetals
[13] Scanlon D O and Watson G W 2011 *Phys. Rev. Lett.* **106** 186403
[14] Isseroff L Y and Carter E A 2013 *Chemistry of Materials* **25** 253
[15] Minami T, Nishi Y and Miyata T 2014 *Appl. Phys. Lett.* **105** 212104
[16] Nyborg M, Azarov A, Bergum K and Monakhov E 2021 *Thin Solid Films* **722** 138573
[17] Blood P and Orton J W 1992 *The Electrical Characterization of Semiconductors: Majority Carriers and Electron States* (London: Academic)
[18] Kittel C 2005 Point Defects *Introduction to Solid State Physics* 8th edn (New York: Wiley) 20
[19] Lee Y S, Winkler M T, Siah S C, Brandt R and Buonassisi T 2011 *Appl. Phys. Lett.* **98** 192115
[20] Frenkel J 1938 *Physical Review* **54** 647
[21] SILVACO® ATLAS™ User's Manual 2016

Appendices

Appendix A

APPENDIX A

Simulation models and inputs

The activated models in the simulations where:

```
models Temp Fermi
```

Temp

Specifies the temperature in Kelvin.

Fermi

Specifies that Fermi-Dirac carrier statistics are used

ATLAS SOURCE CODE

```
set Tstart=270
set LoopsN=240
set Tstep=-1

loop steps=$LoopsN

stmt T=$Tstart:$Tstep

go atlas simflags="-160"

mesh  space.mult=1

set temp=$T

### STRUCTURE
set FilmThickness=0.5
set TotalThickness=100


### Acceptors & Donors
set Accept1=0.22
set AcceptConc1=1e18
set FilmDopConc=1e10
set SubstrDopConc=1e15


### MESH
```

```
x.mesh loc=0.00 spac=1
x.mesh loc=1 spac=1
y.mesh loc=0.00 spac=0.001
y.mesh loc=$FilmThickness/2 spac=$FilmThickness/20
y.mesh loc=$FilmThickness spac=0.001
y.mesh loc=$FilmThickness+1 spac=0.01
y.mesh loc=$FilmThickness+10 spac=0.5
y.mesh loc=$FilmThickness+20 spac=1
y.mesh loc=$TotalThickness-10 spac=1
y.mesh loc=$TotalThickness-5 spac=0.1
y.mesh loc=$TotalThickness spac=0.01


### REGIONS
region number=1 x.min=0 x.max=1 y.min=0.0 y.max=$FilmThickness USER.MATERIAL
     =CuprousOxide
region number=2 x.min=0 x.max=1 y.min=$FilmThickness y.max=$TotalThickness \
material=silicon


### ELECTRODES
electrode name=anode top
electrode name=cathode bottom


### DOPING & MATERIAL
doping region=1 p.type conc=$FilmDopConc uniform
doping region=2 n.type conc=$SubstrDopConc uniform
material material=CuprousOxide user.group=semiconductor user.default=silicon
      \
permittivity=7.1 affinity=3.1 EG300=2.17 EGALPHA=1e-30


### TRAPS
TRAP region=1 E.LEVEL=2.17-$Accept1 ACCEPTOR DENSITY=$AcceptConc1 DEGEN=1
     SIGN=1E-16 SIGP=1e-14
#

output L.TEMPER=false E.TEMP=false H.TEMP=false RECOMB=false TRAPS.FT \
con.band val.band band.param

models temperature=$temp fermi

contact name=cathode workfunction=4.1

method itlimit=10000 trap MIN.TEMP=2 MAX.TEMP=1000 maxtraps=4

if cond=($temp = $Tstart)
solve init
save outf="Init.str"
log outfile="IV.log"
solve Vanode=0.01 name=anode
solve Vanode=0.05 name=anode
solve Vanode=0.1 name=anode
solve Vanode=0.2 name=anode
```

```
solve Vanode=0.5 name=anode
solve Vanode=0.2 name=anode
solve Vanode=0.1 name=anode
solve Vanode=0.05 name=anode
solve Vanode=0.01 name=anode
solve Vanode=0 name=anode
solve Vanode=-0.01 name=anode
solve Vanode=-0.05 name=anode
solve Vanode=-0.1 name=anode
solve Vanode=-0.2 name=anode
solve Vanode=-0.3 name=anode
solve Vanode=-0.5 name=anode
solve Vanode=-0.75 name=anode
solve Vanode=-1 name=anode
save outf="Prev.str"
else
load infile="Prev.str" master
solve prev Vanode=-1 name=anode
save outf="Prev.str"
if.end

probe lat.temp  x=0.5 y=$FilmThickness/2
probe p.conc    x=0.5 y=$FilmThickness/2
probe band.gap  x=0.5 y=$FilmThickness/2
probe n.conc    x=0.5 y=$TotalThickness/2

if cond=($temp = $Tstart)
log outfile="CF.log"
else
log outfile="CF.log" append
if.end

solve name=anode Vanode=-1 ac freq=1e3 vss=0.03
solve name=anode Vanode=-1 ac freq=4e3 vss=0.03
solve name=anode Vanode=-1 ac freq=1.6e4 vss=0.03
solve name=anode Vanode=-1 ac freq=6e4 vss=0.03
solve name=anode Vanode=-1 ac freq=2.5e5 vss=0.03
solve name=anode Vanode=-1 ac freq=1e6 vss=0.03


l.end

quit
```

Appendix B

APPENDIX B

Simulation models and inputs

The activated models in the simulations where:

```
models srh auger optr
```

SRH

Enables Shockley-Read-Hall recombination - Trap assisted recombination, where the electron recombines trhough a localized state within the bandgap. SRH is modelled as:

$$R_{SRH} = \frac{pn - n_{ie}^2}{TAUP0[n + n_{ie}exp(\frac{ETRAP}{kT_L})] + TAUN0[p + n_{ie}exp(\frac{-ETRAP}{kT_L})]} \tag{B.1}$$

where ETRAP is the trap level with reference to the intrinsic Fermi level, T_L the lattice temperatrure in kelvin and TAUN0 and TAUP0 the electron and hole lifetimes.

Auger

Enables Auger recombination, is moddeled through the expression:

$$R_{Auger} = AUGN(pn^2 - nn_{ie}^2) + AUGP(np^2 - pn_{ie}^2) \tag{B.2}$$

Where AUGN nad AUGP is the auger coefficients. Default values has been used.

OPTR

Enables radiative recombination, which is given by:

$$R_{SP_m}](x,y) = ESEP \cdot EMISSION_FACTOR_{\frac{c}{NEFF}} \cdot D(E) \cdot GAIN0 \cdot \sqrt{\frac{\hbar\omega - E_g}{jq}} \cdot f(\frac{E_c - E_{fn} + GAMMA(\hbar\omega - E_g)}{kT}) \cdot [1 - f(\frac{E_v - E_{fp} - (1-GAMMA)(\hbar\omega - E_g)}{kT})] \tag{B.3}$$

where: c is the speed of light, $\hbar$ Planck's constant, k Boltzman constant, E_G the energy bandgap, E_c and E_v the conduction and valence band energies, T the lattice temperature, E_{fn} and E_{fp} the electron and hole quasi Fermi energies, ω the emission frequency that corresponds to the transition energy E, D(E) is the optical mode density, EMISSION.FACTOR, GAIN0 and GAMMA are user defined parameters from the material statement (default values were employed) [**atlas**].

ATLAS SOURCE CODE

```
go atlas
# Definition of constants
# Mesh
# X-Mesh
# Y-Mesh
# Regions
# Electrodes
# Doping
# Material properties
# Models
# Light beams
# Solving

set defects=0
set depth=0.1
#Cu2O material parameters
set Cu2O_bandgap = 2.17
set Cu2O_epsilon = 7.6
set Cu2O_affinity = 3.2
set Cu2O_elec_mobility = 200
set Cu2O_hole_mobility = 100
set Cu2O_Nc = 2.43e19
set Cu2O_Nv = 1.34e19
set Cu2O_tau=1e-4

#CuO material parameters
set CuO_bandgap = 1.35
set CuO_epsilon =18.1
set CuO_affinity = 4.07
set CuO_elec_mobility = 10
set CuO_hole_mobility = 5
set CuO_Nc = 2.43e19
set CuO_Nv = 1.34e19
set CuO_tau=1e-9


#AZO material paremeters
set AZO_bandgap = 3.35
set AZO_epsilon = 9
set AZO_affinity =4.4
set AZO_elec_mobility =10
set AZO_hole_mobility = 5
set AZO_Nc = 2.2e18
set AZO_Nv =1.8e19

set ZnO_thickness = 0.01
set AZO_thickness = 0.085
set CuO_thickness = $depth
set Cu2O_thickness =2.5

mesh
x.mesh loc=0.0  spacing=0.1
```

```
x.mesh loc=1.0  spacing=0.1


y.mesh loc=0.0 spacing=0.001
y.mesh loc=0.1 spacing=0.01
y.mesh loc=1 spacing=0.1
y.mesh loc=2 spacing=0.1
y.mesh loc=2.4 spacing=0.01
y.mesh loc=$AZO_thickness+$ZnO_thickness+$Cu2O_thickness + $CuO_thickness
     spacing=0.001


region num=1 user.material=AZO y.min=0.0 y.max=$AZO_thickness x.min=0 x.max
     =1

region num=2 user.material=Ga2O3 y.min=$AZO_thickness y.max=$AZO_thickness+
     $ZnO_thickness x.min=0 x.max=1

region num=3 user.material=Cu2O y.min=$AZO_thickness+$ZnO_thickness y.max=
     $AZO_thickness+$ZnO_thickness+$Cu2O_thickness x.min=0 x.max=1

region num=4 user.material=Cu2O y.min=$AZO_thickness+$ZnO_thickness+
     $Cu2O_thickness y.max= $AZO_thickness+$ZnO_thickness+$CuO_thickness+
     $Cu2O_thickness x.min=0 x.max=1

electr num=1 name=cathode top length=1

electr num=2 name=anode substrate material=Au

material material=Ga2O3 user.default=GaN user.group=semiconductor \
affinity=4.0 eg300=4.8 nc300=3.72e18 nv300=3.72e18 permittivity=10.0 \
mun=118 mup=50

material mat=AZO user.group=semiconductor user.default=ZnO EG300=
     $AZO_bandgap PERMITTIVITY=$AZO_epsilon AFFINITY=$AZO_affinity MUN=
     $AZO_elec_mobility MUP=$AZO_hole_mobility NC300=$AZO_Nc NV300=$AZO_Nv
     index.file=AZO.nk

material mat=Cu2O user.group=semiconductor user.default=GaAs EG300=
     $Cu2O_bandgap PERMITTIVITY=$Cu2O_epsilon AFFINITY=$Cu2O_affinity MUN=
     $Cu2O_elec_mobility MUP=$Cu2O_hole_mobility NC300=$Cu2O_Nc NV300=
     $Cu2O_Nv index.file=Cu2O_h.nk TAUN=10E-6

doping uniform   y.min=0.0   y.max=$AZO_thickness   x.min=0 x.max=1.0  n.
     type concentration=1e20

doping uniform   y.min=$AZO_thickness   y.max=$AZO_thickness +
     $ZnO_thickness   x.min=0 x.max=1.0  n.type concentration=1e18
doping uniform   y.min=$AZO_thickness+$ZnO_thickness y.max=$AZO_thickness+
     $ZnO_thickness+$Cu2O_thickness  x.min=0 x.max=1.0 p.type concentration
     =1e16
doping uniform trap region=3 acceptor e.level=1.77 conc=$defects sigp=1E-15
     sign=1E-15
doping uniform   y.min=$AZO_thickness+$ZnO_thickness + $Cu2O_thickness y.max
     =$AZO_thickness+$ZnO_thickness+$Cu2O_thickness+ $CuO_thickness x.min=0
```

```
    x.max=1.0 p.type concentration=1e19

output con.band val.band



models srh auger optr
method trap atrap=0.5 maxtrap=10

solve init
save outf="Cu2O_init_ $defects .str"

beam num=1 x.o=0.5 y.o=-2.0 AM1.5 verbose tr.matrix
solve b1=1e-16
solve b1=1e-12
solve b1=1e-8
solve b1=1e-4
solve b1=1e-1
solve b1=1

log outf="Cu2O_IV_IL_ $defects .log"
solve vanode=0.00 name =anode vstep=0.02 vfinal =2
structure outf="Cu2O_IL_ $defects .str"

set xtot=1
extract init infile="Cu2O_IV_IL_ $defects .log"
extract name="IVdata" curve(v."anode",i."anode"/$xtot*1e8*1e3*(-1)) outfile
    ="ivcurve_ $defects .txt"

extract name="Defects = $defects" outfile="Param_ $defects .txt"

extract name="Jsc" y.val from curve(v."anode", i."anode") where x.val=0.0
    outfile="Param_ $defects .txt"

extract name="JscmAcm2" $Jsc*1e08*1e03/$xtot outfile="Param_ $defects .txt"

extract name="Voc" x.val from curve(v."anode", i."anode") where y.val=0.0
    outfile="Param_ $defects .txt"

extract name="Pm" min(curve(v."anode", (v."anode" * i."anode")))  outfile="
    PM_ $defects .txt"

extract name="Vm" x.val from curve(v."anode", (v."anode"*i."anode") ) \
where y.val=$"Pm" outfile="Param_ $defects .txt"

extract name="Im" $"Pm"/$"Vm" outfile="Param_ $defects .txt"

extract name="FF" ($"Pm"/($"Jsc"*$"Voc"))*100 outfile="Param_ $defects .txt"

extract name="Opt_intens" max(beam."1") outfile="Param_ $defects .txt"

extract name="Eff" (-1e8*$Pm/($Opt_intens))*100 outfile="Param_ $defects .
    txt"

# SECOND ATLAS RUN FOR SPECTRAL RESPONSE
```

```
# set monochromatic light beam for spectral analysis
beam num=2 x.origin=0.5 y.origin=-2.0 angle=90.0

# saves optical intensity to solution files
output opt.int

# spectral response
solve init
solve previous
solve previous b1=0
log outf="spectral_ $defects .log"
solve b2=1 beam=2 lambda=0.3 wstep=0.01 wfinal=0.7

extract init inf="spectral_ $defects .log"
extract name="IQE" curve(elect."optical wavelength", \
-(i."anode")/elect."available photo current") outf="spectral_IQE_ $defects .
    dat"
extract name="EQE" curve(elect."optical wavelength", \
-(i."anode")/elect."source photo current") outf="spctral_EQE_ $defects .dat"

quit
```